

UNIVERSITY OF ZAGREB
FACULTY OF MECHANICAL ENGINEERING AND NAVAL ARCHITECTURE

**3D CFD CALCULATION OF INJECTOR
NOZZLE FLOW FOR STANDARD AND
ALTERNATIVE FUELS**

DIPLOMA WORK

Mentors:

Prof. dr. sc. Neven Duić

Doc. dr. sc. Zoran Lulić

Student:

Luka Perković

Zagreb, 2007

Diploma Work - Assignment

3D CFD Calculation of Injector Nozzle Flow for standard and alternative Fuels

Introduction

The CFD code AVL FIRE offers the possibility to simulate multi phase flow situations like they are appearing in all kind of fuel injection nozzles. The calculation of this kind of flows provides valuable information for the development of nozzles and injection strategies. E.g. the shape of the nozzle hole, the number of nozzle holes, injection timing and several other parameters can be a subject of optimization.

In this project it is planned to assess the resulting Diesel spray for different kind of model nozzles especially focusing on the type of fuel which is used. Standard Diesel fuel will be under investigation as well as different alternative fuels.

The topic of alternative fuels is one which is becoming more and more interesting for engine manufacturers. The reason is that using fuels from sustainable sources has been recognized as one remedy to solve the greenhouse gas problematic. The European Community e.g. has already defined certain amounts of bio-fuels which have to be added to fossil fuels in the near future.

Since the properties of these bio-fuels sometimes differ significantly from the fuels used nowadays, it is necessary to see if the current injection and combustion systems can handle the new type of fuels with maintaining or even improving their performance regarding fuel consumption and pollutant emission.

Within this Diploma work it is planned to perform the following calculations on the basis of model nozzles:

Outline

Channel cases:

- From calculations that have been done up to now, 5 well working cases should be selected.
 - I and Y type channels to be included for each presented pressure difference
-

- Perform restarts with activated erosion model
- Recalculation with 2 additional fuel types (DME, FAME) and activated erosion model

Target cases:

- One target case should be selected
- Two selected pressure drops (I and Y channel types)
- Apply diesel fuel as well as the 2 additional fuels from the above case.

Output:

The following quantities should be post-processed

- 3D: phase distribution – assessment of the cavitation zones – comparison with experiments
- 3D: velocity profiles
- 3D: for cases with erosion, plausibility check of eroded zones
- 2D: discharge

General Comments:

The geometry and fuel data are available at AVL. Some data has already been transferred some will be transferred as soon as possible to FSB.

SUMMARY

In this diploma thesis multiphase flow analysis was done via simulations in CFDWM/FIRE application for standard diesel and two alternative biofuels, FAME and DME, inside different nozzle models and under various boundary conditions. Analysis criteria regarding fuel type are: phase volume fraction distribution due to cavitation, mass flow rate and velocity profile in nozzle model.

Nozzle model consists of narrow channel with sharp (type I) or rounded (type Y) inlet section, with or without downstream placed target.

Simulation results show clearly difference between three observed fuels, which was expected considering their different physical properties. Mass flow in channel type I is lower than one in Y channel type. Also, mass flow rate of DME was lowest, despite biggest flow velocity. FAME fuels achieved largest mass flow rate in all cases. Cavitation is present in all cases, but in Y channel type without target it is negligible small.

STATEMENT

*I would like to state that this Diploma work was done on my own, based on a knowledge that I gained on **Faculty of Mechanical Engineering and Naval Architecture at University of Zagreb**, using specified literature and materials provided by **AVL**.*

MENTION

*I would like to thank to **prof. dr. sc. Neven Duić** for given opportunity for this diploma work, and also for suggestions and help provided. I would also like to thank to co-mentor **doc. dr. sc. Zoran Lulić**, research assistants **Marko Ban, dipl. ing.** and **Milan Vujanović, dipl. ing.** for really great and unselfish help.*

*Also many thanks to **dr. Reinhard Tatschl, dr. Peter Priesching** and **dr. David Greif** from **AVL**, for data provided, as well as essential suggestions regarding this work.*

*And at the end, I would like to thank my girlfriend **Matea Nikolac** on grammar and style corrections, as well as support given during the whole undergraduate study.*

CONTENTS

LIST OF FIGURES.....	3
LIST OF TABLES.....	6
1. INTRODUCTION	7
2. CAVITATION INSIDE FUEL NOZZLES.....	9
2.1. Generally about cavitation phenomena	9
2.2. Cavitation erosion.....	10
2.3. Cavitation inside real nozzles	12
3. CFD MATHEMATICAL MODEL	14
3.1. General assumptions about flow type.....	14
3.2. General information about AVL Multiphase module.....	14
3.3. Conservation equations in <i>Multifluid</i> model	14
3.3.1. Multifluid model equations in discretized form	16
3.3.2. k- ϵ turbulence model	16
3.4. Interfacial models	17
3.4.1. Linear Cavitation Model.....	18
3.4.2. Cavitation Drag Model	18
3.4.3. Bubble number density and interfacial area equations.....	19
3.5. Closure coefficients and empirical factors of mathematical model	21
3.6. Erosion modeling.....	21
3.7. User functions.....	22
3.8. Parameters of mathematical model.....	23
4. COMPUTATIONAL DOMAIN WITH SELECTIONS AND BOUNDARY	
CONDITIONS	24
4.1. Geometry and mesh	24
4.2. Selections and boundary conditions	26
4.3. Initial conditions and time parameters.....	28
5. PHYSICAL PROPERTIES OF OBSERVED FUELS	29
6. RESULTS	30
6.1. Comparison of simulation results with experimental data	30
6.1.1. Comparison criteria	30
6.1.2. Nozzle models without downstream placed target.....	30

6.1.2.1	Results analysis	32
6.1.3.	Nozzle models with downstream placed target	32
6.1.3.1	Results analysis	34
6.2.	Comparison of fuels: nozzle models without downstream placed target	35
6.2.1.	Comparison criteria	35
6.2.2.	Volume fraction, pressure, velocity and TKE distribution.....	35
6.2.3.	Mass flow rate	56
6.2.4.	Erosion incubation time and MDPR.....	57
6.2.5.	Velocity profiles vs. narrow channel height.....	61
6.2.6.	Channel I results analysis	64
6.2.7.	Channel Y result analysis	64
6.3.	Comparison of fuels: nozzle models with downstream placed target	66
6.3.1.	Comparison criteria	66
6.3.2.	Volume fraction, pressure, velocity and TKE distribution.....	66
6.3.3.	Mass flow rate	75
6.3.4.	Erosion incubation time and MDPR.....	75
6.3.5.	Velocity profiles vs. narrow channel height.....	77
6.3.6.	Results analysis	Error! Bookmark not defined.
7.	CONCLUSION	80
8.	REFERENCES	81
	APPENDIX: FORTRAN CODE OF USER FUNCTIONS	83

LIST OF FIGURES

Figure 2.1 Experiment: relation between mass flow rate and pressure drop [5]	10
Figure 2.2 Bubble implosion near surface [6].	10
Figure 2.3 Cavitation erosion curve, according to [11].	11
Figure 2.4 MDPR vs. time, presented in [6].	11
Figure 2.5 Experiment: Cavitation erosion in nozzle model [14].	12
Figure 2.6 Visualisation of cavitation inside metallic nozzle [21].	13
Figure 2.7 Macrofracture due to cavitation erosion in real nozzle [9]	13
Figure 2.8 Cavitation damage zone with magnified micro-crater (right) [9]	13
Figure 3.1 General Polyhedral Control Volume around point P_0	16
Figure 4.1 Nozzle model geometry: narrow channel	24
Figure 4.2 Nozzle model geometry: downstream placed target	24
Figure 4.3 Narrow channel mesh with coordinate system	25
Figure 4.4 Channel flow: boundary conditions/selections	27
Figure 4.5 Target flow: Boundary conditions/selections	28
Figure 6.1 Channel I vs. experiment: volume fraction distribution	31
Figure 6.2 Channel I vs. experiment: mass flow rate	32
Figure 6.3 Target I&Y vs. experiment: volume fraction distribution	33
Figure 6.4 Target I&Y vs. experiment: mass flow rate	34
Figure 6.5 Channel flow: area where distribution results are presented	35
Figure 6.6 Channel I, 100-040bar comparison: volume fraction and absolute pressure distribution	36
Figure 6.7 : Channel I, 100-040bar comparison: velocity and TKE distribution	37
Figure 6.8 Channel I, 200-080bar comparison: volume fraction and absolute pressure distribution	38
Figure 6.9 Channel I, 200-080bar comparison: velocity and TKE distribution	39
Figure 6.10 Channel I, 300-080bar comparison: volume fraction and absolute pressure distribution	40
Figure 6.11 Channel I, 300-080bar comparison: velocity and TKE distribution	41
Figure 6.12 Channel I, 300-120bar comparison: volume fraction and absolute pressure distribution	42

Figure 6.13 Channel I, 300-120bar comparison: velocity and TKE distribution	43
Figure 6.14 Channel I, 400-160bar comparison: volume fraction and absolute pressure distribution.....	44
Figure 6.15 Channel I, 400-160bar comparison: velocity and TKE distribution	45
Figure 6.16 Channel Y, 100-040bar comparison: volume fraction and absolute pressure distribution.....	46
Figure 6.17 Channel Y, 100-040bar comparison: velocity and TKE distribution.....	47
Figure 6.18 Channel Y, 200-080bar comparison: volume fraction and absolute pressure distribution.....	48
Figure 6.19 Channel Y, 200-080bar comparison: velocity and TKE distribution.....	49
Figure 6.20 Channel Y, 300-080bar comparison: volume fraction and absolute pressure distribution.....	50
Figure 6.21 Channel Y, 300-080bar comparison: velocity and TKE distribution.....	51
Figure 6.22 Channel Y, 300-120bar comparison: volume fraction and absolute pressure distribution.....	52
Figure 6.23 Channel Y, 300-120bar comparison: velocity and TKE distribution.....	53
Figure 6.24 Channel Y, 400-160bar comparison: volume fraction and absolute pressure distribution.....	54
Figure 6.25 Channel Y, 400-160bar comparison: velocity and TKE distribution.....	55
Figure 6.26 Channel I: mass flow rate.....	56
Figure 6.27 Channel Y: mass flow rate	56
Figure 6.28 Channel I: erosion incubation time	57
Figure 6.29 Channel Y: erosion incubation time.....	58
Figure 6.30 Channel I: MDPR.....	59
Figure 6.31 Channel Y: MDPR	60
Figure 6.32 Channel flow: location of polyline on which velocity profiles were taken	61
Figure 6.33 Channel I comparison: velocity profiles vs. narrow channel height.....	62
Figure 6.34 Channel I comparison: velocity profiles vs. narrow channel height.....	63
Figure 6.35 Target flow: area where distribution results are presented	66
Figure 6.36 Target I, 100-001bar comparison: volume fraction and absolute pressure distribution.....	67
Figure 6.37 Target I, 100-001bar comparison: absolute velocity and TKE distribution	68

Figure 6.38 Target I, 400-020bar comparison: volume fraction and absolute pressure distribution.....	69
Figure 6.39 Target I, 400-020bar comparison: absolute velocity and TKE distribution.....	70
Figure 6.40 Target Y, 100-001bar comparison: volume fraction and absolute pressure distribution.....	71
Figure 6.41 Target Y, 100-001bar comparison: absolute velocity and TKE distribution	72
Figure 6.42 Target Y, 400-020bar comparison: volume fraction and absolute pressure distribution.....	73
Figure 6.43 Target Y, 100-001bar comparison: absolute velocity and TKE distribution	74
Figure 6.44 Target I&Y comparison: mass flow rate	75
Figure 6.45 Target I comparison: erosion incubation time on target	75
Figure 6.46 Target I comparison: MDPR on target.....	76
Figure 6.47 Target Y comparison: erosion incubation time on target.....	76
Figure 6.48 Target Y comparison: MDPR on target	76
Figure 6.49 Target flow: location of polyline on which velocity profiles were taken ..	77
Figure 6.50 Target I comparison: velocity profiles vs. narrow channel height.....	77
Figure 6.51 Target Y comparison: velocity profiles vs. narrow channel height	78

LIST OF TABLES

Table 3.1 Variables in the Generic Conservation Equation.....	15
Table 3.2 Closure coefficients for k- ϵ turbulence model.....	17
Table 3.3 Closure coefficients and empirical factors of mathematical model.....	21
Table 3.4 List of User functions	22
Table 3.5 Parameters of mathematical model.....	23
Table 4.1 Nozzle model meshes dimensions	25
Table 4.2 Domain selections with corresponding boundary conditions.....	27
Table 4.3 Simulation parameters: Time step and calculation length.....	28
Table 5.1 Physical properties of observed fuels	29

1. INTRODUCTION

Alternative fuels are lately becoming more and more interesting due to a fact that they don't contribute increasing of carbon in atmosphere in Earth's atmosphere carbon-cycle [1]. In Europe and U.S. fuels gained from rapeseed (RME) and soybean (SOME), together called FAME fuels or biodiesel, are used as an alternative fuel or as a compound in standard diesel/biodiesel mixture. Another biofuel is very interesting, DME, which can be gained from all sorts of different sources. In Europe there are currently several active norms that are regulating amount of biodiesel in mineral diesel (EN 590 allow up to 5%), as well as properties of FAME fuels (EN 14241) [2]. Diesel fuel injection equipment manufacturers brought common statement in which they support the development of compression ignition alternative fuels [3].

Diversity of physical properties between mentioned fuels causes their different flow characteristics inside fuel nozzles. In this work flow simulations with analyses were performed in different nozzle models, for every inlet/outlet pressure drop and three different fuels. Calculations were done via CFD. Analysis is performed by following criteria: volume fraction distribution due to cavitation, achieved mass flow rate and velocity profile in narrow channel section. Additional figures are presented: pressure, absolute velocity and turbulence kinetic energy distribution. Also, erosion modelling was done.

For simulations is used one of the commercially available CFD application, AVL's CFD Workflow Manager with FIRE solver (hereafter CFDWM/FIRE). In CFDWM/FIRE one can perform simulations of multiphase flows via *Multiphase* module with Erosion modelling included.

At the beginning, a brief introduction to cavitation phenomena and cavitation erosion is given. This is followed by brief overview of mathematical model, based upon [4], [5] and [6]. Next, the simulation parameters, nozzle model geometry and calculation domain with boundary conditions is presented. Fuel properties table for standard Diesel,

DME and FAME is provided by AVL. Finally, results are presented in form of figures with corresponding analysis and conclusion.

First part of the simulations is used to present a validity of the mathematical model, as well as its closure coefficients value selection (*Chapter 6.1*). Since experimental results on nozzle models for mineral diesel were available, direct comparison with corresponding simulation results was performed. Experimental results were also provided by AVL.

After conclusion that mathematical model and its closure coefficients satisfy, comparison of simulation results between previously mentioned fuels was done for different boundary conditions and nozzle models.

2. CAVITATION INSIDE FUEL NOZZLES

2.1. Generally about cavitation phenomena

Cavitation is a phenomena of evaporation of condensed gases inside fluid when its static pressure drops below saturation (evaporation) value. Since evaporation is usually happening without heat gaining, phenomena is often called cold boiling. Real fluids, such as fuels, hold some liquefied gases when fluid static pressure is above their saturation point. If pressure drops below saturation level (for, example, because of high flow velocity), liquefied gases change phase into vapour/gas and two-phase flow occurs. In two-phase flow liquid continuous phase and gaseous dispersed phase are present. Saturation pressure depends on physical properties of fluid and temperature. Generally, with greater temperature saturation pressure raises and cavitation becomes bigger.

Based on continuity equation it is known that usually when velocity increases, pressure drops. For example, this happens in diesel engine injector nozzles. Evaporated phase reduces the cross-section of fuel flow, additionally increasing flow velocity inside nozzle. As a consequence, flow is choked earlier than if cavitation never occurred. Theoretic maximum of velocity is determined by acoustic velocity [7]. Experimental data regarding to mass flow rate are available in [5], and upon them we can see that mass flow rate becomes stationary after certain amount of pressure drop is applied, which can be seen in *Figure 2.1*. This can be explained with the fact that no flow information data transfer could be done upstream, once the acoustic velocity is reached.

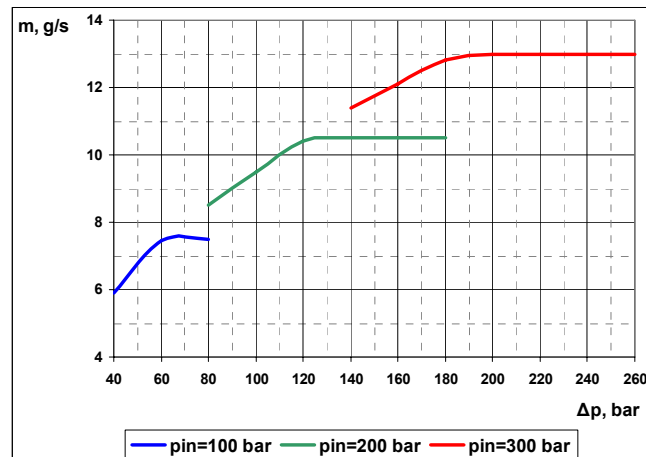


Figure 2.1 Experiment: relation between mass flow rate and pressure drop [5]

Cavitation can be observed anywhere, where high local velocities occur. For example, in central axis of free vortex or on turbine blades [8].

2.2. Cavitation erosion

According to [9] cavitation is often considered to be the main reason for primary break up of injector nozzle. When cavitated bubbles encounter a high-pressure zone, they collapse and cause explosive shocks to the surface, if they collapse close enough to the surface [6] (*Figure 2.1*). These surface shocks cause localized deformation and pitting. Cavitation pits eventually link up and cause a general roughening of the surface and material removal. The process by which material is removed from a surface is called cavitation erosion, and the resulting damage is termed cavitation damage [10, 11, 12]. Cavitation damage is caused by the microjet impingement of the fluid induced by the fluid pressure change. This microjet can reach high local velocities (several 100 m/s) that cause a shock (the order of magnitude is bigger than 1 GPa, the duration is approximately 1 ns and the affected area is in order of a few m^2) with high local tension of the material [13].

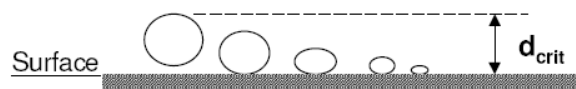


Figure 2.2 Bubble implosion near surface [6].

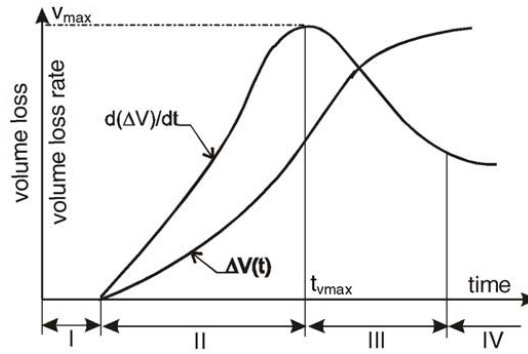


Figure 2.3 Cavitation erosion curve, according to [14].

According to [14] cavitation erosion curve can be divided into four main periods (Figure 2.3). The first, incubation period, is an initial period of damage in which the volume loss of material is unmeasurable. During this initial stage of erosion material accumulates energy, plastic deformation starts. Fatigue processes and strain hardening can occur during this time. The intensification of damage is observed in the second period of cavitation erosion. This period is distinguished by a fast increase of the volume loss rate of erosion. In this time the volume loss rate reaches its maximum value. In the third period a weakening of damage is observed, and the volume loss rate decreases. This course of material failure is explained by a decrease of the cavitation intensity caused by filling pits with water. Finally, the fourth period, is characterized by an almost constant volume loss rate of erosion.

Stationary value of erosion can be presented with MDPR (Mean Depth of Penetration Rate) value. Mathematical description of MDPR and erosion incubation time (erosion modelling) are based on [15] and [16].

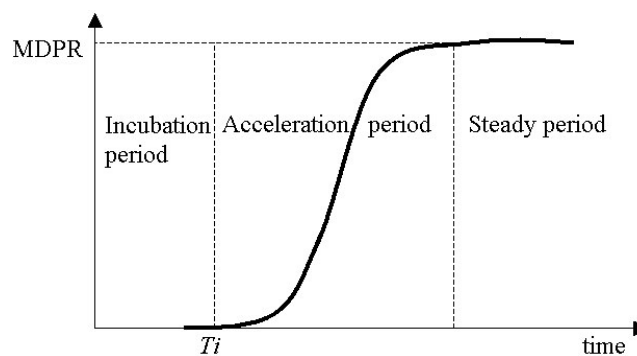


Figure 2.4 MDPR vs. time, presented in [6]

Figure 2.4 presents cavitation erosion on target in nozzle model, [17]. Red color presents 100% liquid, and blue 100% gaseous phase.

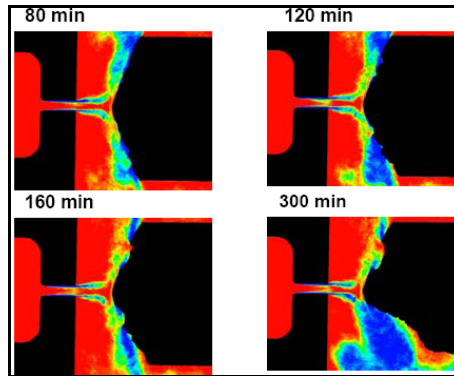


Figure 2.5 Experiment: Cavitation erosion in nozzle model [17].

2.3. Cavitation inside real nozzles

An injector nozzle is one of the most important parts of a diesel engine. Injectors deliver fuel to cylinders of internal combustion engines. The fuel is sprayed through an injector nozzle, typically at high pressure, to improve the mixing of fuel with air and therefore the combustion efficiency. Modern passenger cars and trucks use high injection pressures. Diesel engine injectors often operate at injection pressures of 25 MPa or higher. Unfortunately, high operating pressures in diesel injectors can cause cavitation in the liquid fuel, leading to degradation in the performance and structural damage to the injector [9]. Cavitation is influencing on spray by an increasing the spray cone angle with the start of cavitation [19]. Also cavitation erosion can occur leading to nozzle failure, as mentioned before.

This leads us to conclusion that besides construction difficulties regarding to continuous increasing of working parameters, physical restrictions regarding to fuel also have to be taken into account.

Although a number of studies have provided evidence on the existence of cavitation inside the nozzle depending on injection pressure, the detailed nature of nozzle flow has remained unknown until recently. There is experimental evidence to show that cavitation within the nozzle modifies the characteristics of the nozzle exit spray and

probably favours atomisation of the spray. It may, however, also affect the internal flow in other ways that are not yet clear. Real size production nozzles have very small dimensions and operate at very high injection pressure over very short time periods. It is therefore very difficult to visualize the internal flow. Hence, most of these studies were performed on real scale transparent models with the aim of visualizing the cavitation structure within the nozzles [18]. Neutron radiography is suitable for visualizing the fuel behaviors inside the metallic nozzle [24], *Figure 2.6*.

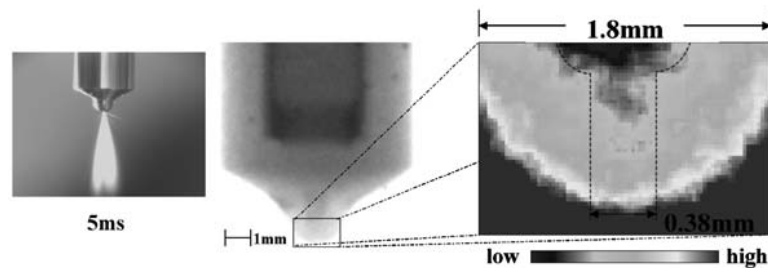


Figure 2.6 Visualization of cavitation inside metallic nozzle [21].

According to [23], for nearly all the duration of the injection process the spray hole is surrounded by cavitation films (Eifler, 1990). As mentioned before, cavitation erosion can lead to failure of nozzle. *Figure 2.7* and *Figure 2.8* presents nozzle that has been found cracked after about 400 h in service.

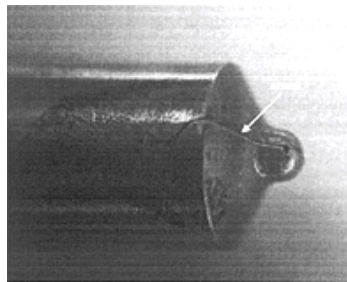


Figure 2.7 Macrofracture due to cavitation erosion in real nozzle [9]

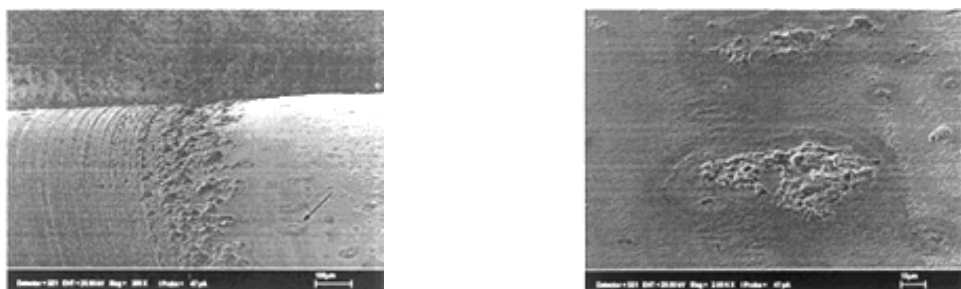


Figure 2.8 Cavitation damage zone with magnified micro-crater (right) [9]

3. CFD MATHEMATICAL MODEL

3.1. General assumptions about flow type

In this work quasi-stationary, inner, non-compressible, viscous, turbulent and two-phase (generally multiphase) type of flow is assumed, so simulation is set-up considering these assumptions. $K-\varepsilon$ turbulence model is used in all calculations due to its successful usage in inner flows for all sorts of different geometries and it is particularly recommended for a quick preliminary estimation of the flow field [25]. Two-phase flow implies bubble number density and interfacial area between liquid and gas phase, so additional transport equations for modeling cavitation should be active in order to describe phase change. From now on liquid phase will be labeled as continuous phase or phase no.1 and gas phase will be labeled as dispersed phase or phase no.2. Flow is not stationary despite stationary boundary conditions, which are static pressure on inlet and outlet. Pressure difference between inlet and outlet is a driving force for flow.

3.2. General information about AVL Multiphase module

Simulation of multiphase flows with CFDWM/FIRE application is done using *Multiphase* module. In *Multiphase* module *Multifluid* model is used, which means that equations for all phases are calculated separately, and pressure is coupled variable. Volume fraction of total must be equal to one.

3.3. Conservation equations in *Multifluid* model

Following description of conservation equation is based on [4].

All conservation equations can be written in generic form:

$$\begin{aligned} \frac{\partial(\alpha\rho\phi)_k}{\partial t} + \nabla \cdot (\alpha\rho v_i \phi)_k = \\ = \nabla \cdot (\alpha \Gamma_\phi \nabla \phi)_k + \nabla \cdot (\alpha q_{\phi S,i})_k + (\alpha q_{\phi V})_k + \sum_{l=1, l \neq k}^N S_{\phi,kl} + \phi_k \sum_{l=1, l \neq k}^N \Gamma_{kl}, \quad k=1, \dots, N \end{aligned} \quad (1)$$

All conservation equations can be reconstructed in differential or integral form by using the values from the following table in equation (1):

Table 3.1 Variables in the Generic Conservation Equation

VARIABLE	ϕ	$\Gamma_{\phi,k}$	$q_{\phi S,i}$	$q_{\phi V}$
Mass	1	0	0	0
Momentum	v_i	$\mu_k + \mu'_k$	$(\mu + \mu')_k \left[\nabla v_i^T - \frac{2}{3} \nabla \cdot v_i \delta_{ij} \right]_k - \frac{2}{3} (\rho k)_k \delta_{ij}$	$-\nabla p + \rho_k f_i$
Turbulence kinetic energy	k	$\mu_k + \frac{\mu'_k}{\sigma_k}$	0	$P_k + P_{B,k} - (\rho \varepsilon)_k$
Turbulence dissipation	ε	$\mu_k + \frac{\mu'_k}{\sigma_\varepsilon}$	0	$C_1 \left(\rho \frac{\varepsilon}{k} \right)_k - C_2 \left(\rho \frac{\varepsilon^2}{k} \right)_k - C_4 [\rho \varepsilon \nabla \cdot v_i]_k$

The compatibility condition must be observed for every phase k :

$$\sum_{k=1}^N \alpha_k = 1 \quad (2)$$

Pressure is assumed identical for all phases:

$$p = p_k, \quad k=1, \dots, N \quad (3)$$

Turbulent viscosity is modeled as:

$$\mu'_k = \left(\rho C_\mu \frac{k^2}{\varepsilon} \right)_k, \quad k=1, \dots, N \quad (4)$$

Turbulent viscosity is flow property, not physical property. If $\mu' \gg \mu$ we have flows with high Re number and vice versa. Molecular viscosity is more significant near wall, where turbulence is damped. So in this region turbulence is modeled via Wall functions.

3.3.1. Multifluid model equations in discretized form

Equation (1) can be integrated over the cell volume to provide the generic conservation equation in integral form:

$$\begin{aligned} \frac{\partial}{\partial t} \int_{KV} (\alpha \rho \phi)_k dV + \int_{KV} [\nabla \cdot (\alpha \rho \mathbf{v}_i \phi)]_k dV = \int_{KV} \nabla \cdot (\alpha \Gamma_\phi \nabla \phi)_k dV + \\ + \int_{KV} \nabla \cdot (\alpha q_{\phi S, i})_k dV + \int_{KV} \left[(\alpha q_{\phi V})_k + \sum_{l=1, l \neq k}^N S_{\phi, kl} + \phi_k \sum_{l=1, l \neq k}^N \Gamma_{kl} \right] dV \end{aligned} \quad (5)$$

$k=1, \dots, N$

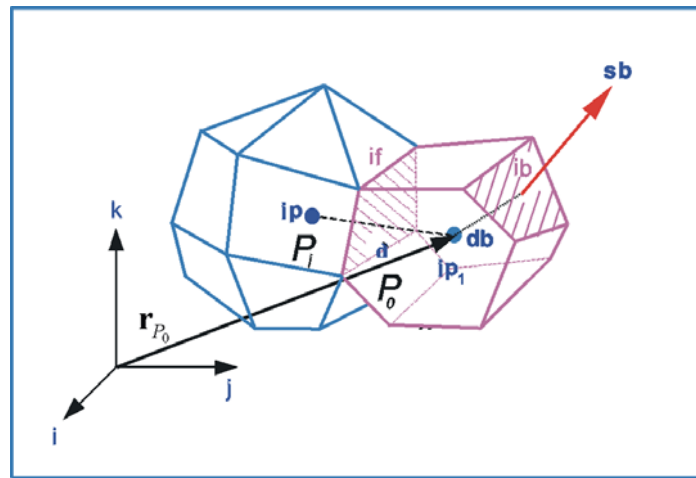


Figure 3.1 General Polyhedral Control Volume around point P_0 .

The integration over the cell volume shown in *Figure 3.1* around the point P_0 yields:

$$\begin{aligned} \frac{\partial}{\partial t} \int_{KV} (\alpha \rho \phi)_k dV + \sum_{j=1}^{n_f} \int_{S_j} (\alpha \rho \mathbf{v}_i \phi)_k \cdot d\mathbf{s}_i = \sum_{j=1}^{n_f} \int_{S_j} (\alpha \Gamma_\phi \nabla \phi)_k \cdot d\mathbf{s}_i + \\ + \sum_{j=1}^{n_f} \int_{S_j} (\alpha q_{\phi S, i})_k \cdot d\mathbf{s}_i + \int_{KV} \left[(\alpha q_{\phi V})_k + \sum_{l=1, l \neq k}^N S_{\phi, kl} + \phi_k \sum_{l=1, l \neq k}^N \Gamma_{kl} \right] dV \end{aligned} \quad (6)$$

$k=1, \dots, N$

3.3.2. k - ϵ turbulence model

This turbulence model is a part of a Eddy Viscosity Models (EVM) with two equations. EVM assumes direct analogy between molecular and turbulent momentum. based on Boussinesq assumption. As a result, two new differential transport equations are derived, for k and ϵ .

When combining equation (1) with *Table 3.1*, it can be seen that closure coefficients for k-ε turbulence model appear. Usually their values are as follows:

Table 3.2 Closure coefficients for k-ε turbulence model

σ	σ_ε	C_1	C_2	C_4	C_μ	C_{Sato}
1.0	1.3	1.44	1.92	-0.33	0.09	0.6

These values are used in our calculations.

It should be noticed that turbulent kinematic viscosity of continuous phase is calculated by equation :

$$\nu_c^t = \nu_c^{t,SI} + \nu_c^{t,BI} \quad (7)$$

First term in equation represents turbulent viscosity caused by shear, and second term represents bubble induced turbulent viscosity. Terms are modeled as follows :

$$\nu_c^{t,SI} = C_\mu \frac{k_c^2}{\varepsilon_c} \quad (8)$$

$$\nu_c^{t,BI} = C_{Sato} D_b \left| \overline{v_r} \right| \alpha_d \quad (9)$$

3.4. Interfacial models

Considering variety cases for *Multifluid* model application, we have variety of interfacial models. In this work following interfacial models were used

- for interfacial mass exchange: Linear Cavitation Model
- for interfacial momentum exchange: Cavitation Drag model

Both interfacial exchange models imply two additional transport equations: Bubble Number Density Equation and Interfacial Area Equation. These equations allows us to close mathematical model via additional closure coefficients.

3.4.1. Linear Cavitation Model

Mass exchange is based on following equation:

$$\Gamma_c = \rho_d N''' 4R^2 \frac{\partial R}{\partial t} = -\Gamma_d \quad (9)$$

The time derivative of the bubble radius is estimated from the Rayleigh equation:

$$R \frac{\partial^2 R}{(\partial t)^2} + \frac{3}{2} \left(\frac{\partial R}{\partial t} \right)^2 = \frac{\Delta p}{\rho_c} \quad (10)$$

The mass exchange can be derived to be equal to:

$$\Gamma_c = \frac{1}{C_{CR}} \text{sign}(\Delta p) 3.85 \frac{\rho_d}{\sqrt{\rho_c}} (N''')^{\frac{1}{3}} (\alpha_d)^{\frac{2}{3}} |\Delta p|^{\frac{1}{2}} = -\Gamma_d \quad (11)$$

where the effective pressure difference equals:

$$\Delta p = p_{isp} - \left(p - C_E \frac{2}{3} \rho_c k_c \right) \quad (12)$$

The closure coefficient C_E , Egler coefficient, depends on local turbulence level. C_{CR} is condensation reduction factor and it is an empirical coefficient used to decrease the condensation rate with respect to the evaporation rate during cavitation.

Bubble number density N''' is calculated as is explained in *Chapter 3.4.3*.

3.4.2. Cavitation Drag Model

Interfacial momentum source includes drag and turbulent dispersion forces:

$$\overline{M}_c = \underbrace{C_D \frac{1}{8} \rho_c A_i'' \overline{v}_r}_{\text{drag}} \left| \overline{v}_r \right| + \underbrace{C_{TD} \rho_c k_c \nabla \alpha_d}_{\text{turbulent dispersion}} = -\overline{M}_d \quad (13)$$

The relative velocity is defined as:

$$\overline{v}_r = \overline{v}_d - \overline{v}_c \quad (14)$$

Now bubble Reynolds number is defined:

$$\text{Re}_d = \frac{v_r D_b}{\nu_c} \quad (15)$$

Drag coefficient C_D is a function of bubble Reynolds number:

$$C_D = \begin{cases} \frac{192}{\text{Re}_b} (1 + 0.1 \text{Re}_b^{0.75}) & \text{Re}_b < 1000 \\ 0.438 & \text{Re}_b \geq 1000 \end{cases} \quad (16)$$

Turbulent dispersion force C_{TD} accounts for the vapor diffusion due to turbulent mixing processes.

3.4.3. Bubble number density and interfacial area equations

Let n''' denote the bubble distribution function in the phase space. Now the total number N''' is defined as:

$$N''' = \int n'''(x_i, M_i, t, r) dx_i dM_i dt dr \quad (17)$$

Through Liouville theorem we can derive transport equation for n''' :

$$\frac{\partial n'''}{\partial t} + \nabla \cdot (n''' M_i) + \frac{\partial}{\partial r} \left(n''' \frac{dr}{dt} \right) = \underbrace{\sum S_j}_{\text{source/drain due to bubble interactions}} + \underbrace{S_{ph}}_{\text{phase change related sources}} \quad (18)$$

Now we can write transport equations for N''' and A''' :

$$\frac{\partial N'''}{\partial t} + \nabla \cdot (N''' M_{0,i}) = \sum R_j + R_{ph} \quad (19)$$

$$\frac{\partial A'''}{\partial t} + \nabla \cdot (A''' M_{2,i}) = \sum \phi_{j2} + \phi_{ph2} \quad (20)$$

Source terms on right side of the equations include various mechanisms and can be modeled as follows (C_{rc} , C_{T1} , C_{ph} and d_{nuc} represents closure coefficients):

Coalescence due to random collision

$$R_{rc} = 4.4 \cdot 10^{-3} C_{rc} \frac{\varepsilon^{\frac{1}{3}} A^{\frac{11}{3}}}{\alpha \alpha_{\max}^{\frac{2}{3}}} \left[1 - \exp \left(-C_{rc} \frac{\alpha^{\frac{1}{3}} \alpha_{\max}^{\frac{1}{3}}}{\alpha_{\max}^{\frac{1}{3}} - \alpha^{\frac{1}{3}}} \right) \right] \quad (21)$$

$$\phi_{rc} = -0.17 C_{rc} \frac{\varepsilon^{\frac{1}{3}} \alpha^{\frac{1}{3}} A^{\frac{5}{3}}}{\alpha_{\max}^{\frac{1}{3}} \left(\alpha_{\max}^{\frac{1}{3}} - \alpha^{\frac{1}{3}} \right)} \left[1 - \exp \left(-C_{rc} \frac{\alpha^{\frac{1}{3}} \alpha_{\max}^{\frac{1}{3}}}{\alpha_{\max}^{\frac{1}{3}} - \alpha^{\frac{1}{3}}} \right) \right] \quad (22)$$

where α_{\max} is the maximum volume fraction related to the packing limit. α_{\max} is taken to be 0.62 here.

Breakup due to turbulent impact

$$R_{T1} = 5.2 \cdot 10^{-3} C_{T1} (1 - \alpha) \frac{\varepsilon^{\frac{1}{3}} A^{\frac{11}{3}}}{\alpha^{\frac{8}{3}}} \exp \left(-\frac{We_{c,T1}}{We} \right) \sqrt{1 - \frac{We_{c,T1}}{We}} \quad (23)$$

$$\phi_{T1} = 0.12 C_{T1} \varepsilon^{\frac{1}{3}} (1 - \alpha) \frac{\varepsilon^{\frac{1}{3}} A^{\frac{5}{3}}}{\alpha^{\frac{2}{3}}} \exp \left(-\frac{We_{c,T1}}{We} \right) \sqrt{1 - \frac{We_{c,T1}}{We}} \quad (24)$$

where We_c is critical Weber number taken to be 2.3 here.

Bubble generation due to phase change

$$R_{ph} = C_{ph} \frac{6Ph}{\rho \pi d_{nuc}^3} \quad (25)$$

$$\phi_{ph} = C_{ph} \frac{6Ph}{\rho d_{nuc}} \quad (26)$$

The interfacial mass and momentum transfer may be closed through the number density and interfacial area information:

$$Ph = \text{sign}(\Delta p) \frac{\rho_d}{\sqrt{\rho_c}} \left(N^m \right)^{\frac{1}{3}} \left(\alpha_d \right)^{\frac{2}{3}} |\Delta p|^{\frac{1}{2}} \quad (27)$$

3.5. Closure coefficients and empirical factors of mathematical model

Table 3.3 Closure coefficients and empirical factors of mathematical model

Label in model equations	Label in SSF	Suggested range
C_E	<i>Egler factor</i>	1÷1.4
C_{CR}	<i>Condensation reduction factor</i>	1÷10
C_{rc}	CC1	0.0001÷1
C_{TI}	CB1	0.01÷10
C_{ph}	CB4	0.1÷1
d_{nuc}	CB5	1e-008÷1e-006
C_{Sato}	<i>Sato's coefficient</i>	0.6
C_{TD}	<i>Dispersion coefficient</i>	0.1÷10

3.6. Erosion modeling

Erosion modeling combines fluid dynamics with material-related quantities. Erosion is in *Multiphase* module modeled within two model quantities:

- Erosion Incubation Time
- Mean Depth Penetration Rate (MDPR)

Physical explanation of both quantities is given in *Chapter 2.2*.

Erosion model is based on [15] and [16]. Equations are valid for ductile materials only. It should be mentioned that material-related variables used in equations (28) and (29) were predefined in AVL and are not changed.

Model implies Ludwig equation for material stress-deformation relation.

Erosion incubation time equation:

$$T_i = \frac{1}{NS} \left[\frac{\sigma_U - \sigma_Y}{\sigma_p - \sigma_Y} \right]^{1+\Theta} \frac{(1+n)(1+\Theta+n\Theta)\sigma_Y + (1+\Theta)(\sigma_U - \sigma_Y)}{(1+n)(1+\Theta+n\Theta)\sigma_Y + (1+\Theta)(\sigma - \sigma_Y)} \quad (28)$$

MDPR equation:

$$MDPR = NS\Delta L = NSL \left[\left(\frac{\varepsilon'}{\varepsilon_U} \right)^{\frac{1}{\Theta}} - 1 \right] \quad (29)$$

3.7. User functions

As mentioned in introduction of this work, before calculations for different fuels could be performed, validity of mathematical model is done. Since experimental data was available, mathematical model was setup upon them. Mathematical model parameters are founded on previous set of calculations (results are given in *Chapter 6.1*). Model was “calibrated” by means of comparison with experimental data, and final values are used for calculation setup for all following cases presented in *Chapter 6.2* and *Chapter 6.3*.

In order to simulate the way that data was taken in experiment, user functions were used. Exact code is given in *Appendix* at the end of this work. Qualitative pictures in experiment were taken with special camera trough whole depth of a nozzle model and various exposition times [15].

Brief description of algorithm: first, cells adjacent to symmetry plane are determined, as well as corresponding upright cells (same x and y, different z, *Figure 4.3*). During simulation, comparison is made after each time step to determine which in-depth cell has biggest volume fraction value (regarding to x and y coordinate). After first time step these values are stored in cells adjacent to symmetry plane. After second time step same operations are performed, but values will be stored only if their value is greater than the ones from previous step. And so on. At the end, results are stored in *.fla file. With this algorithm simulation of in-depth thru-time screening is performed.

Table 3.4 List of User functions

allocating module	defining variables that need to be allocated, first to execute
useini subroutine	initialization of cell addressing matrix and VF_max variable
useout subroutine	performes given operations of volume fraction comparison

useplo subroutine	writing results to *.fla file
--------------------------	-------------------------------

3.8. Parameters of mathematical model

.Following values for closure coefficients were used in all cases.

Table 3.5 Parameters of mathematical model

SSF label	Value
<i>Egler factor</i>	1.2
<i>Condensation reduction factor</i>	10
CC1	1
CB1	0.1
CB4	1
CB5	1e-006
<i>Sato's coefficient</i>	0.6
<i>Dispersion coefficient</i>	0.5

4. COMPUTATIONAL DOMAIN WITH SELECTIONS AND BOUNDARY CONDITIONS

4.1. Geometry and mesh

Nozzle model geometry consists of narrow channel with sharp (type I) or rounded (type Y) inlet, *Figure 4.1*. We will also observe models that have , regarding to a narrow channel, downstream placed target, *Figure 4.2*.

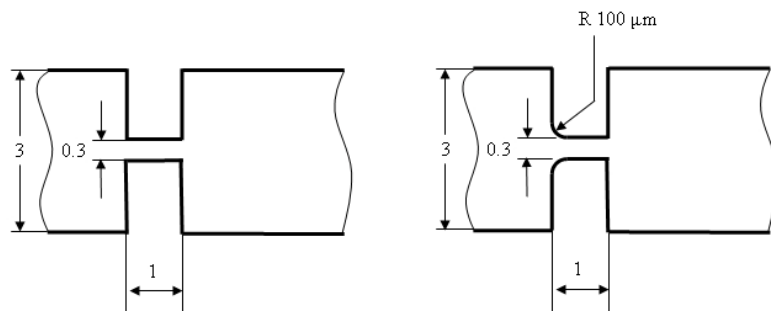


Figure 4.1 Nozzle model geometry: narrow channel

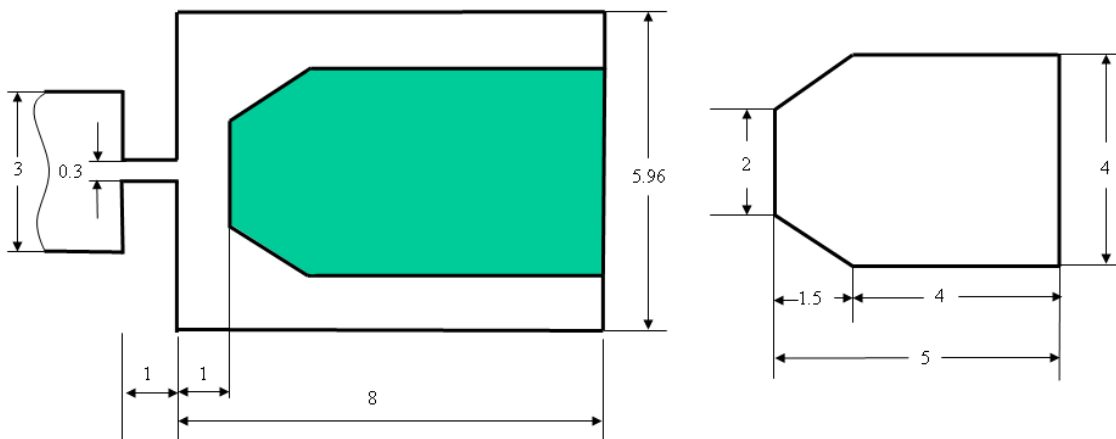


Figure 4.2 Nozzle model geometry: downstream placed target

Geometry of nozzle model is symmetrical regarding to x-y plane so computational domain consists from half of nozzle model geometry also regarding to X-Y plane. Thickness of model is determined with z coordinate. Narrow channel type I mesh can be seen in *Figure 4.3*.

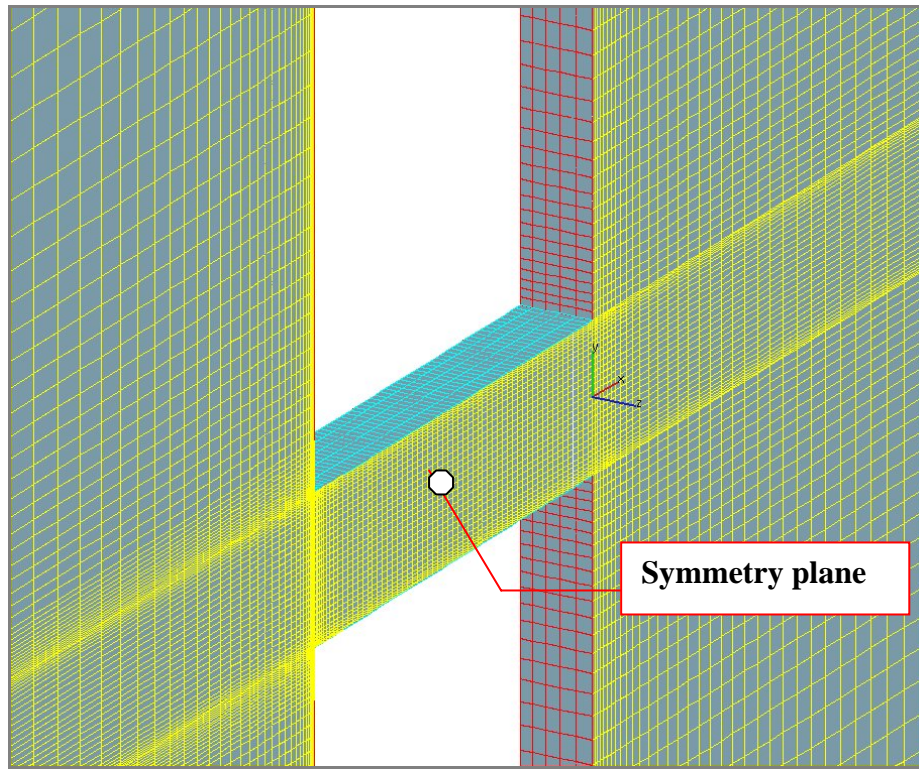


Figure 4.3 Narrow channel mesh with coordinate system

When observing whole geometry (*Figure 4.4* and *Figure 4.5*) it can be noticed that we can roughly divide it on four zones: inlet zone, narrow channel zone and outlet zone. Dimensions of all nozzle model meshes by zones is given in following table.

Table 4.1 Nozzle model meshes dimensions

<i>Zone</i>	<i>Nozzle model</i>	<i>Length, x (mm)</i>	<i>Height, y (mm)</i>	<i>Width, z (mm)</i>
inlet	without target	10	3	0.15
	with target	10	3	0.15
narrow channel	without target	1	0.3	0.15
	with target	1	0.3	0.15
outlet	without target	12	3	0.15

	with target	21	5.96	0.15
--	-------------	----	------	------

Dimensions that are strictly defined: nozzle model thickness, narrow channel, target and height (y coordinate). Length (x coordinate) of inlet and outlet zone is not strictly defined and should be selected to give developed flow on inlet and outlet zone. Calculation stability is also affected with these parameter.

Because of overall of four different nozzle model types, and computational domains respectively, hereafter computational domains will be referred as:

- Channel I → channel type I without target
- Channel Y → channel type Y without target
- Target I → channel type I with downstream placed target
- Target Y → channel type Y with downstream placed target

4.2. Selections and boundary conditions

All domain meshes have same number and type of selections. Boundary conditions must be defined for every phase separately, except pressure which is coupled variable and is defined only for continuous phase. Also, total of phase volume fractions must be equal to one. If there is no specific selection on domain boundary it is assumed that this boundary is wall.

Boundary conditions of turbulence and volume phase fraction, as well as static pressure and flow direction must be determined at inlet and outlet selections. Since driving force for flow quantities is pressure difference between inlet and outlet selection, in order to avoid too long mesh on inlet zone, flow direction on inlet selection is determined. Boundary turbulence parameters were pre-defined by AVL. List of all selections and corresponding boundary conditions are given in following table.

Table 4.2 Domain selections with corresponding boundary conditions

<i>Name of selection</i>	<i>Variables</i>	<i>Continuous phase (phase 1)</i>	<i>Dispersed phase (phase 2)</i>
inlet	static pressure	depends on case	-
	flow direction	x=1, y=0, z=0	-
	turbulent kinetic energy	0.1	0.3
	turbulent length scale	2e-04	2e-04
	turbulent dissipation rate	25	125
	volume fraction	0.99999	1e-06
outlet	static pressure	depends on case	-
	turbulent parameters are not fixed	-	-
	volume fraction	0.99999	1e-06
symmetry	-	-	-
erosion	-	-	-

Following figure shows nozzle model without (Figure 4.6) and with (Figure 4.7) downstream placed target with its boundary conditions and erosion modeling selection .

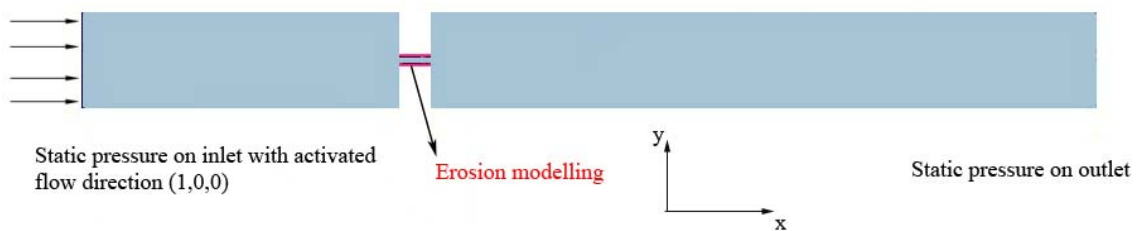


Figure 4.4 Channel flow: boundary conditions/selections

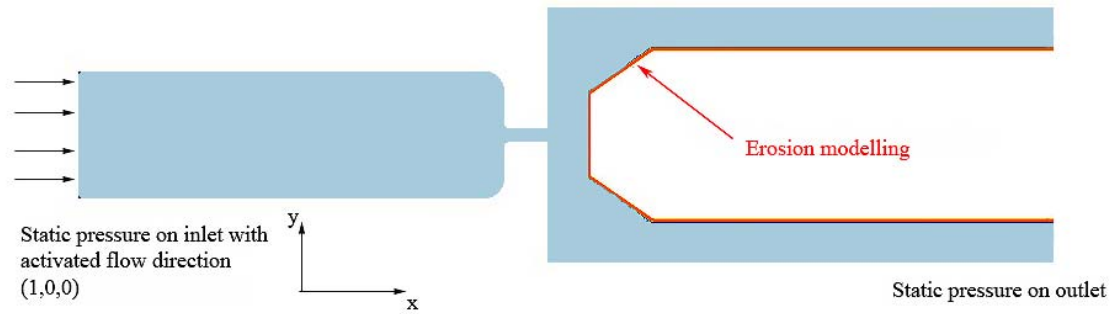


Figure 4.5 Target flow: Boundary conditions/selections

4.3. Initial conditions and time parameters

Considering the fact that simulation is not stationary it is necessary to determine initial conditions, as well as time step and calculation length.

Initial conditions are: in every cell velocity is equal to zero and static pressure is equal to pressure at inlet selection. Since flow type is expected to be quasi-stationary, small variations of mass flow rate is expected.

Table 4.3 Simulation parameters: Time step and calculation length

<i>Parameter</i>	<i>Value</i>	<i>Unit</i>	<i>Description</i>
time step	1e-08	s	should be choosed to give stable calculation and reasonable computation time
simulation end time	4e-07	s	equal to camera exposition time in experiment [12].

5. PHYSICAL PROPERTIES OF OBSERVED FUELS

Physical properties of observed fuels, which must be determined, are written in following table.

Table 5.1 Physical properties of observed fuels (Properties for Diesel and DME are taken from calculations for SCANIA, done by D. Greif and properties for FAME are from the book ‘biodiesel’ by M. Mittelbach)

				Min. diesel	DME	FAME
phase 1	density	ρ	kg/m ³	828	661	880
	dynamic viscosity	μ	Pas	2.14E-03	1.558E-04	3.52E-03
	saturation pressure	p_{isp}	Pa	892	892 (assumption)	892 (assumption)
phase 2	density	ρ	kg/m ³	7	11.23	11.5
	dynamic viscosity	μ	Pas	1E-05	1.028E-05	1E-05 (assumption)

Properties of FAME fuel are similar to mineral diesel, while properties of DME are similar to liquified natural gas [23].

6. RESULTS

6.1. Comparison of simulation results with experimental data

6.1.1. Comparison criteria

Experimental data which was provided by AVL were used to “calibrate” Multiphase mathematical model via closure coefficients. Experimental data refers to mineral diesel, so only mineral diesel cases were performed.

Two comparison criteria could be taken into account:

- volume fraction distribution (qualitative)
- mass flow rate (quantitative)

Under phrase volume fraction, for all cases, it will be assumed volume fraction of dispersed in continuous phase.

When representing volume fraction distribution, it should be mentioned that user functions were included in simulation model (as explained in *Chapter 3.6*). Results were presented on symmetry plane (*Figure 4.3*). Also, m Mass flow rate was taken on inlet selection and was multiplied by two, since only half of nozzle model geometries were included in computational domains.

6.1.2. Nozzle models without downstream placed target

Numerical simulations were performed for five different pressure drops on Channel I domain.

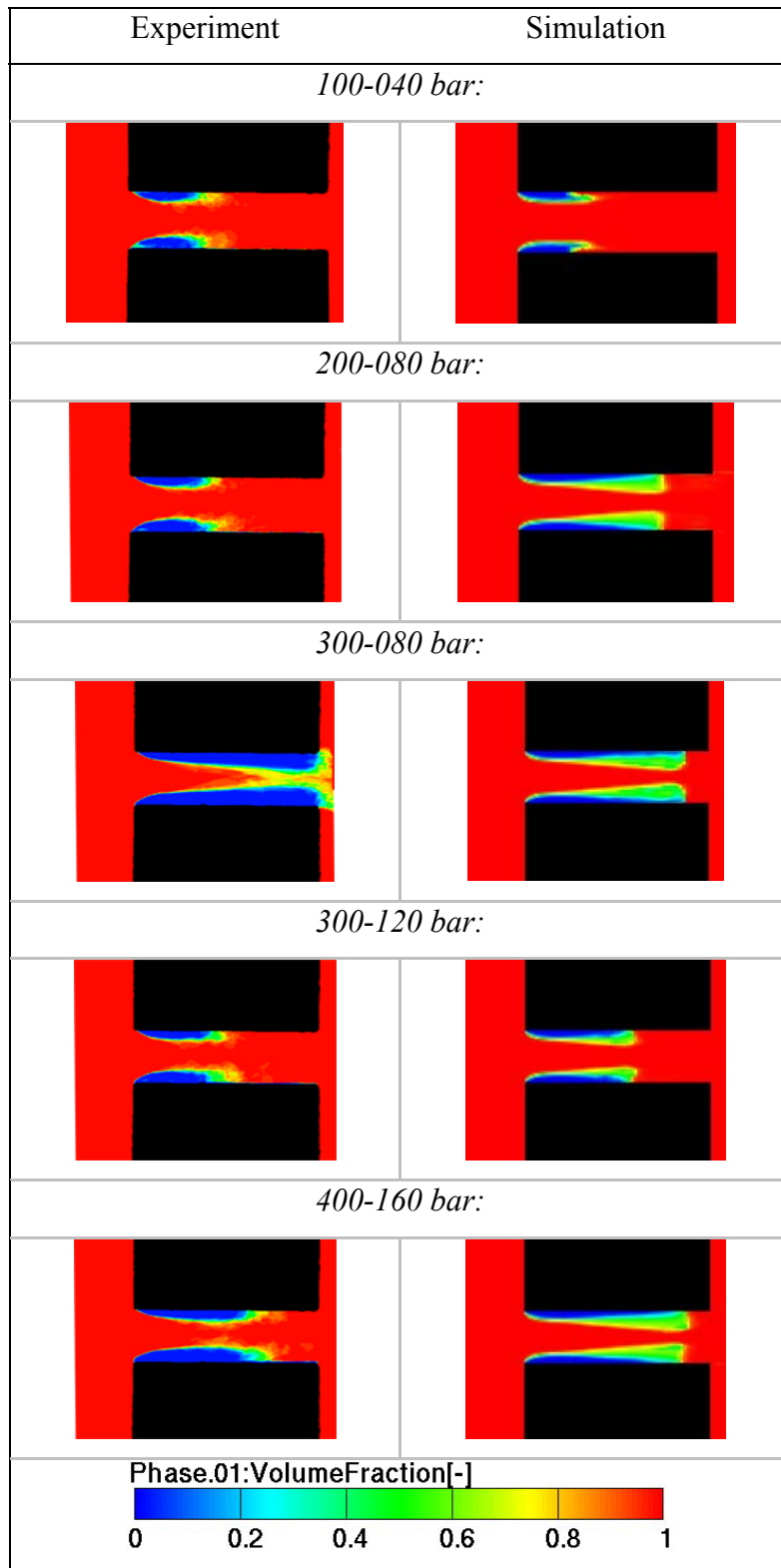


Figure 6.1 Channel I vs. experiment: volume fraction distribution

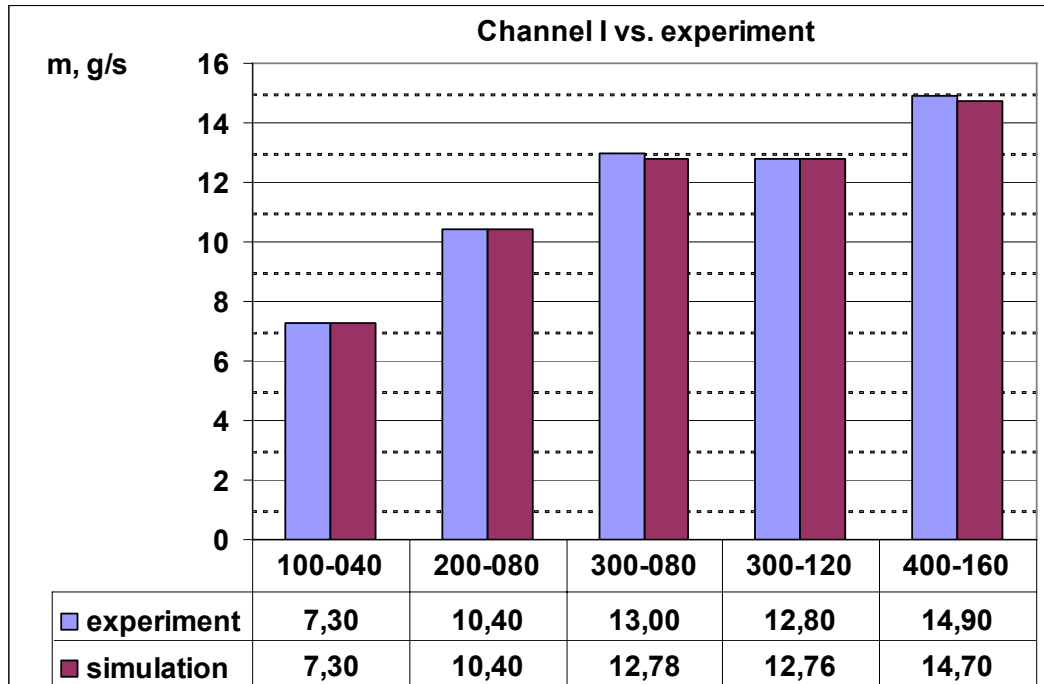


Figure 6.2 Channel I vs. experiment: mass flow rate

6.1.2.1 Results analysis

From *Figure 6.1* we can see that cavitation occurs in all cases. Cavitation will be described with cavitation length and thickness. Cavitation length given by simulation represents experimental data very well, except in 200-080bar and 300-080bar case in which cavitation is longer than in experiment. Cavitation thickness matches experimental data better than cavitation length.

Mass flow rate, *Figure 6.2*, shows almost excellent match of simulation results and experimental values in all cases.

6.1.3. Nozzle models with downstream placed target

Numerical simulations were performed for two different pressure drops on both, Target I and Target Y domain. It should be mentioned that experimental data for mass flow rate on Target Y was not available.

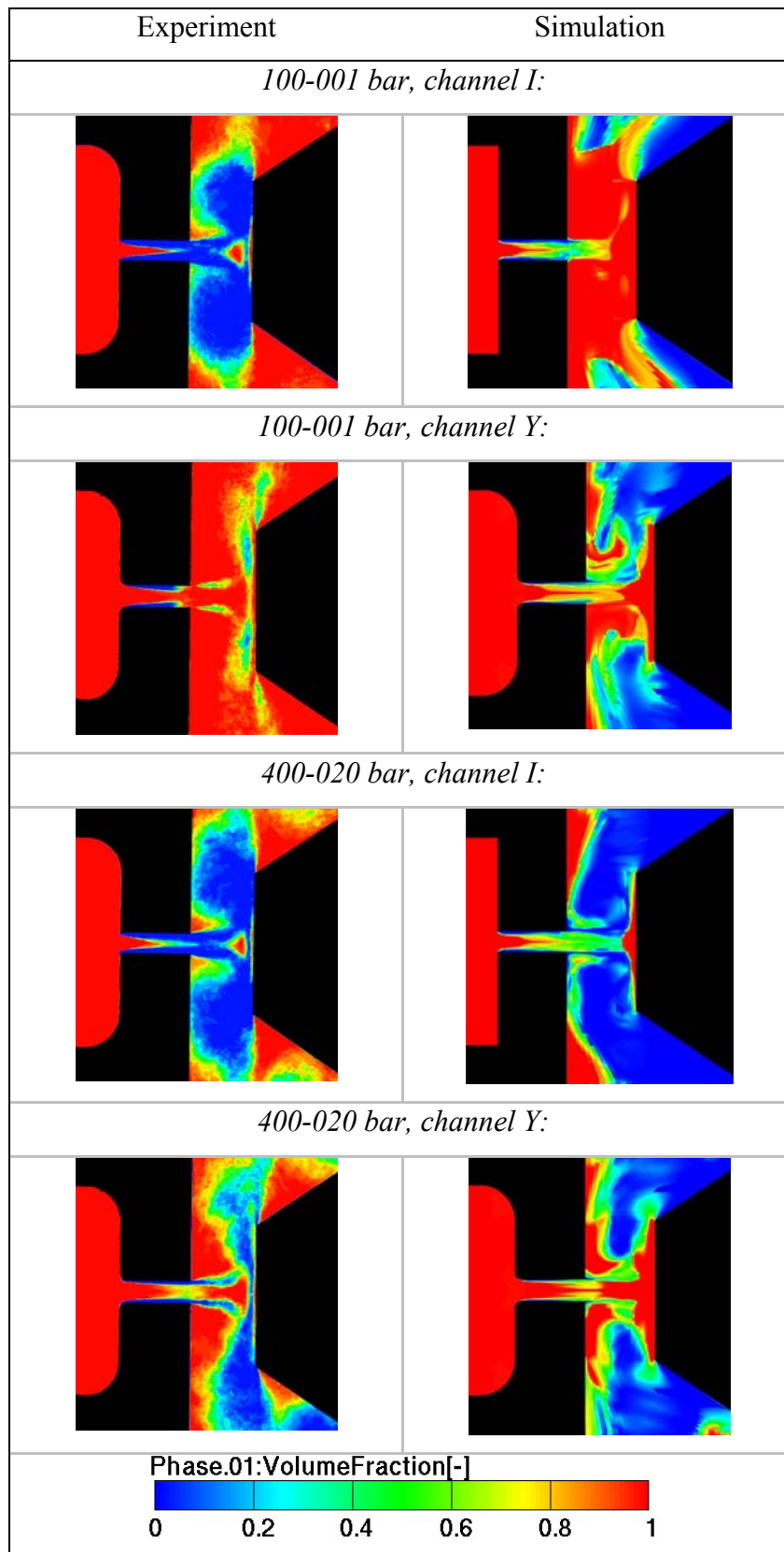


Figure 6.3 Target I&Y vs. experiment: volume fraction distribution

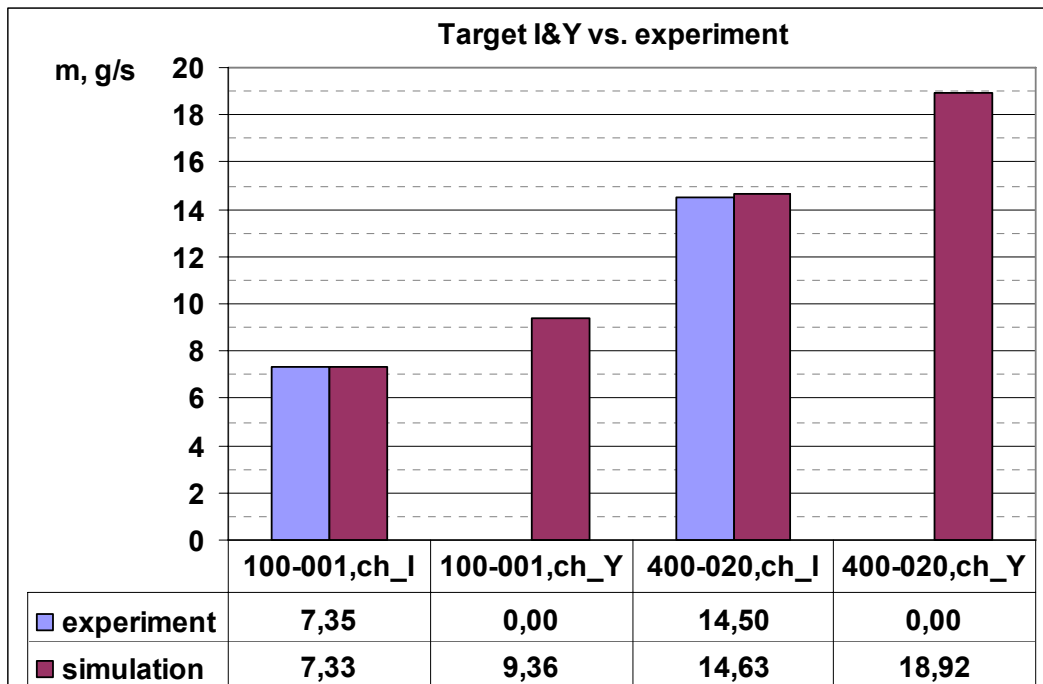


Figure 6.4 Target I&Y vs. experiment: mass flow rate

6.1.3.1 Results analysis

When observing Volume fraction distribution, *Figure 6.3*, it can be seen that cavitation length and thickness given by simulation matches experimental picture only in narrow channel zone. In outlet zone cavitation distribution does not match experiment, cavitation is too excessive.

Mass flow rate again matches experimental value very well, *Figure 6.4*.

6.2. Comparison of fuels: nozzle models without downstream placed target

6.2.1. Comparison criteria

All mentioned above, in Chapter 6.1.1, is also valid here, with some additional comparison criteria. Comparison criteria are as follows:

- volume fraction distribution on symmetry plane
- absolute pressure distribution on symmetry plane
- absolute velocity distribution on symmetry plane
- turbulent kinetic energy (TKE) distribution on symmetry plane
- mass flow rate on Inlet selection
- erosion incubation time & MDPR distribution on Erosion selection
- velocity profiles vs. narrow channel height

6.2.2. Volume fraction, pressure, velocity and TKE distribution

Since we are only interested in narrow channel zone, results are presented as following figure shows:



Figure 6.5 Channel flow: area where distribution results are presented

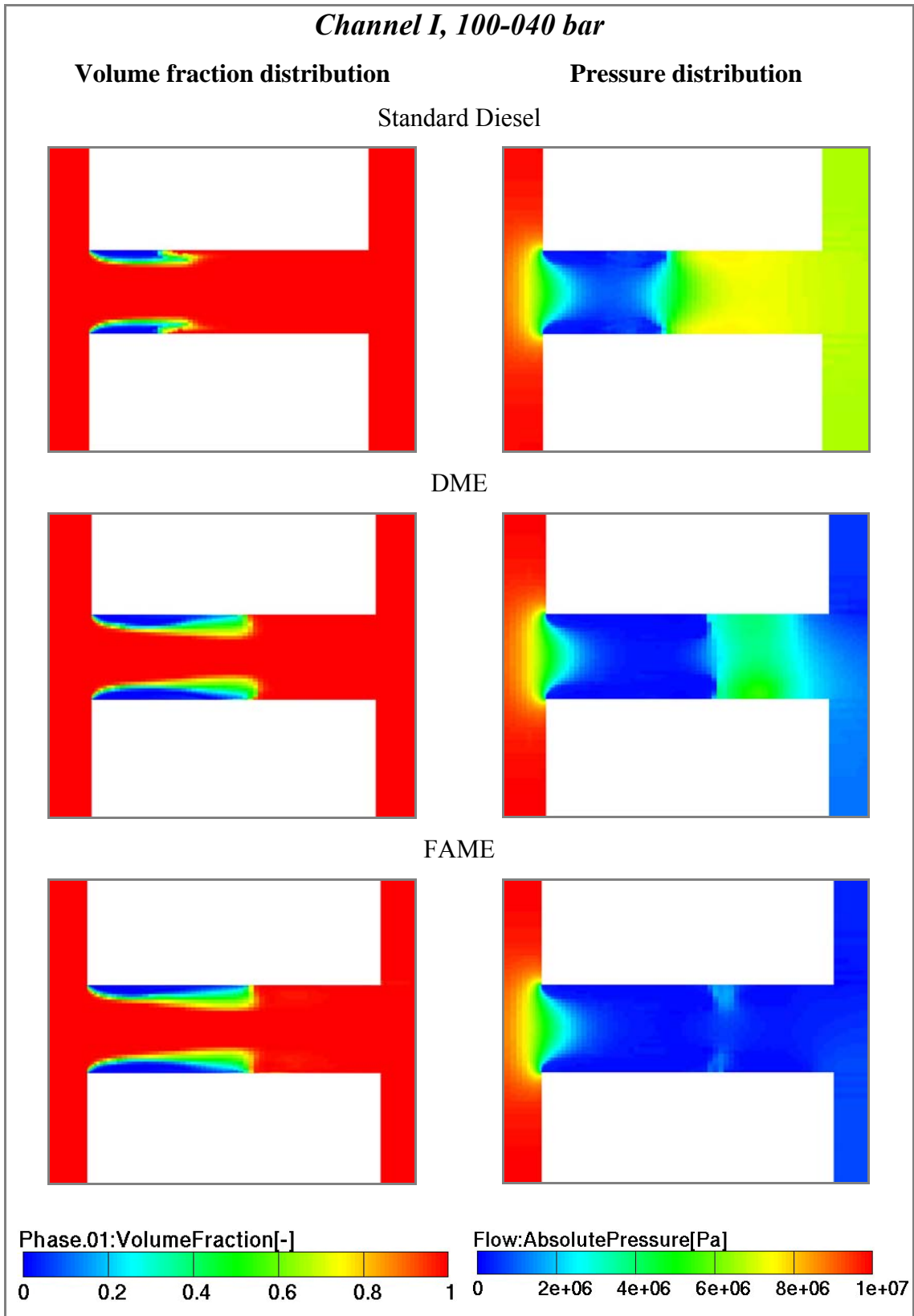


Figure 6.6 Channel I, 100-040bar comparison: volume fraction and absolute pressure distribution

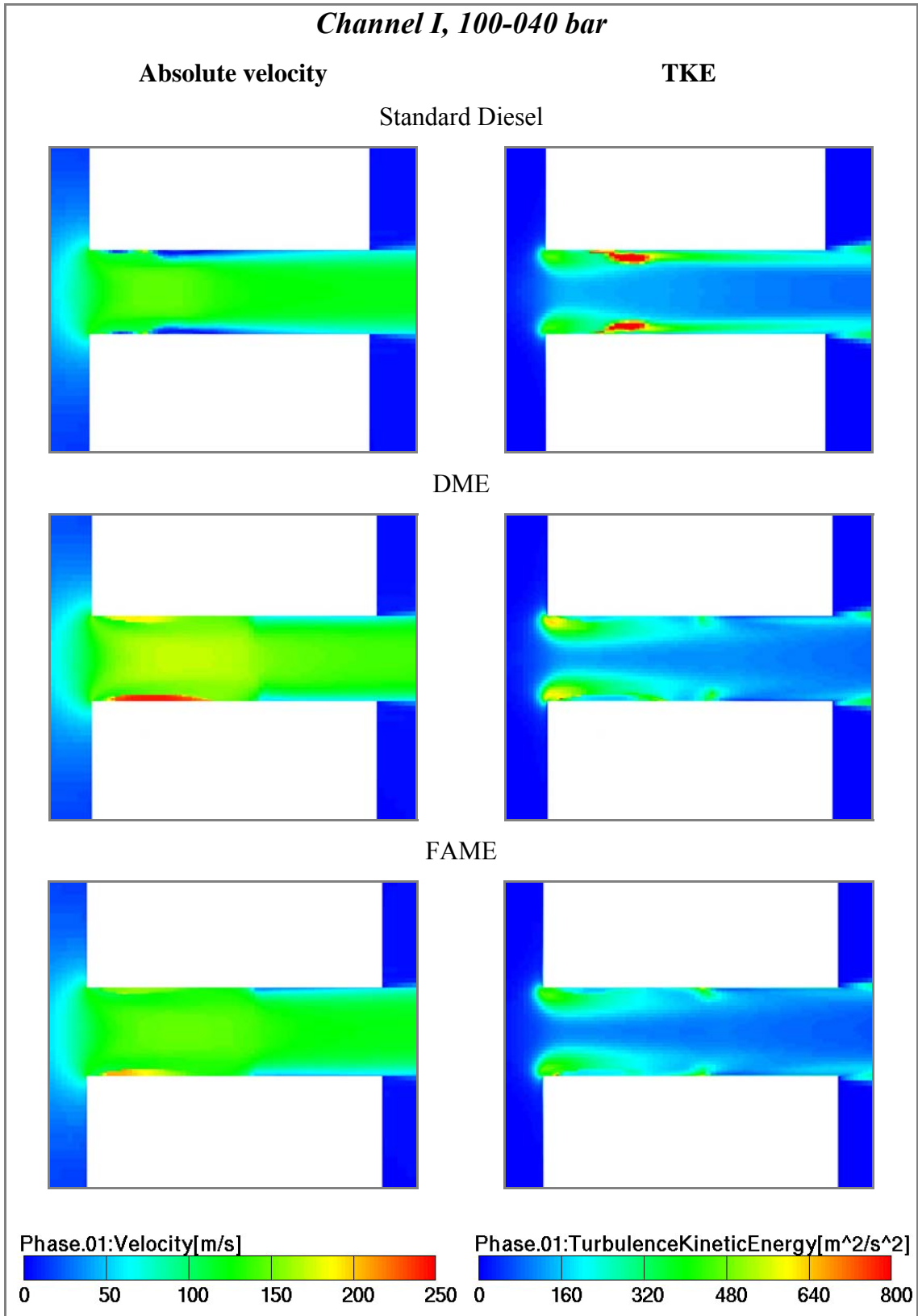


Figure 6.7 : Channel I, 100-040bar comparison: velocity and TKE distribution

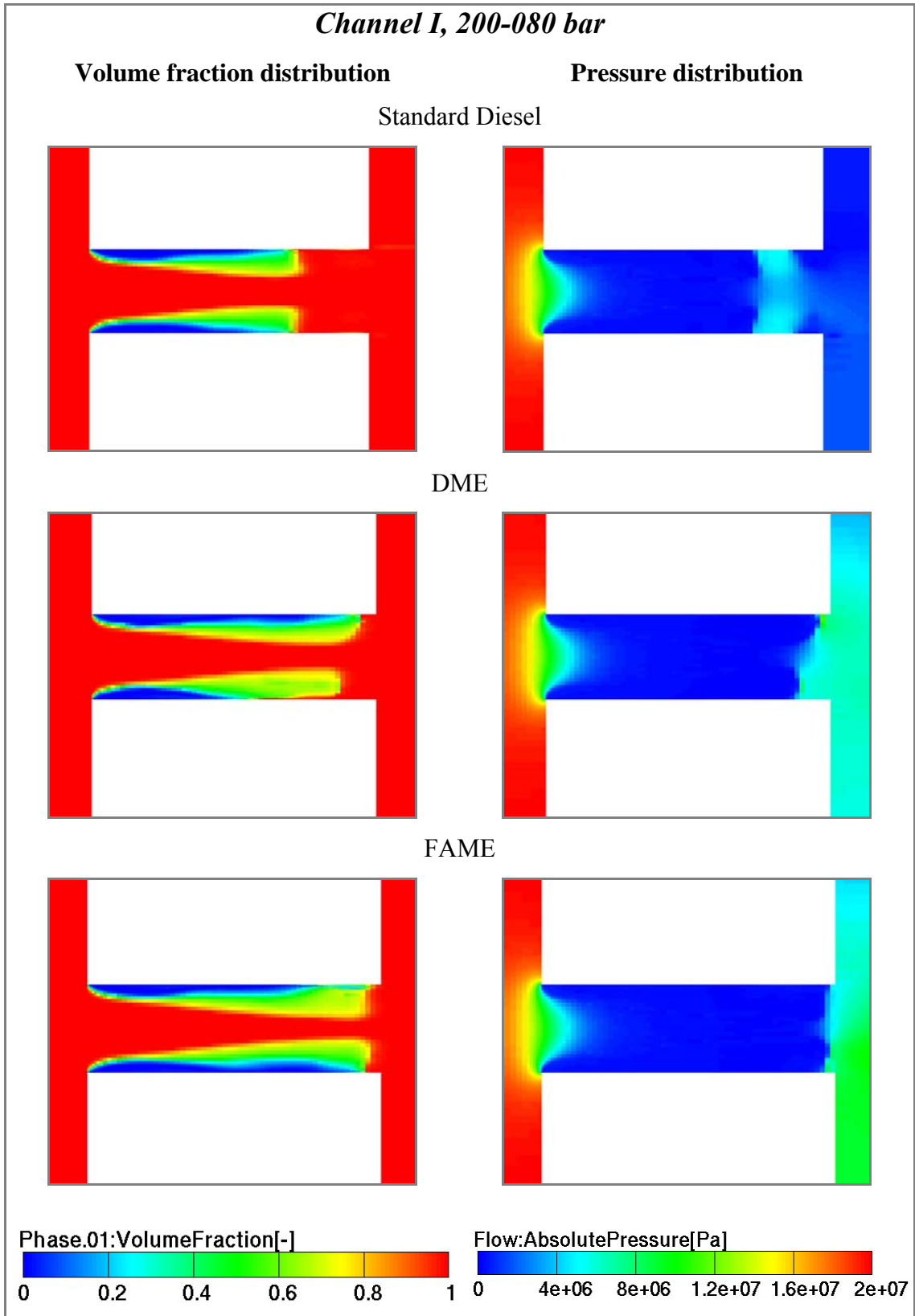


Figure 6.8 Channel I, 200-080bar comparison: volume fraction and absolute pressure distribution

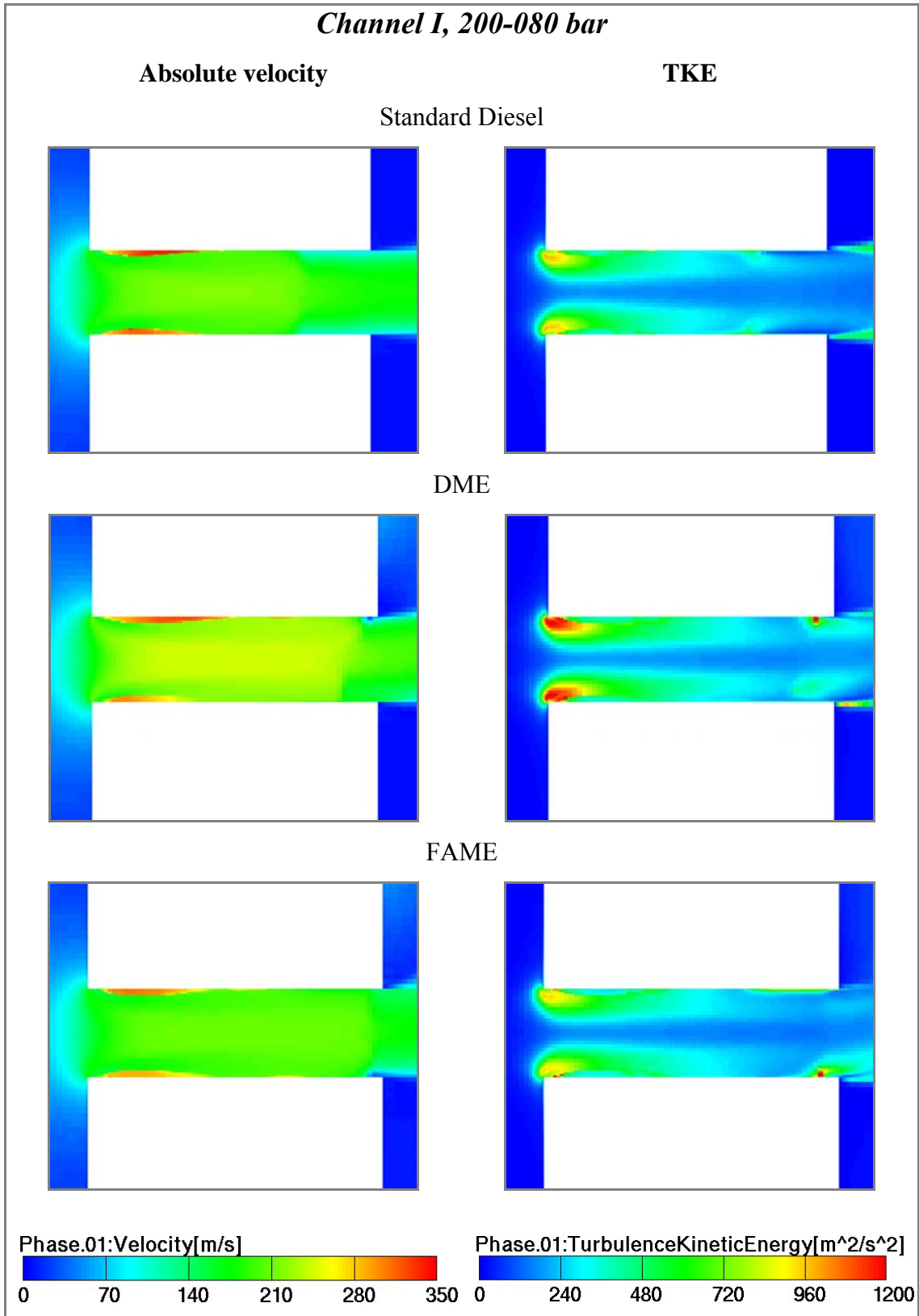


Figure 6.9 Channel I, 200-080bar comparison: velocity and TKE distribution

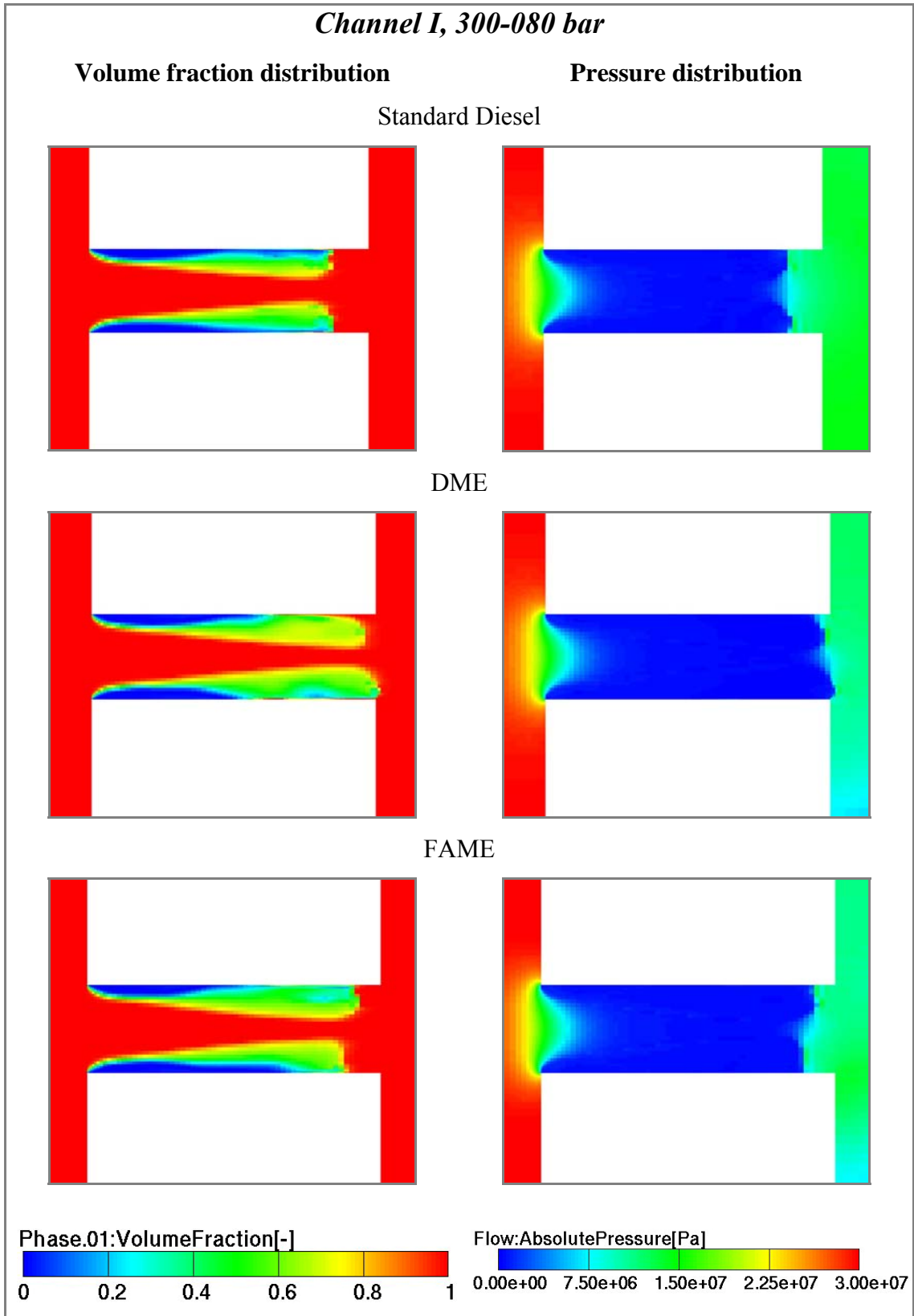


Figure 6.10 Channel I, 300-080bar comparison: volume fraction and absolute pressure distribution

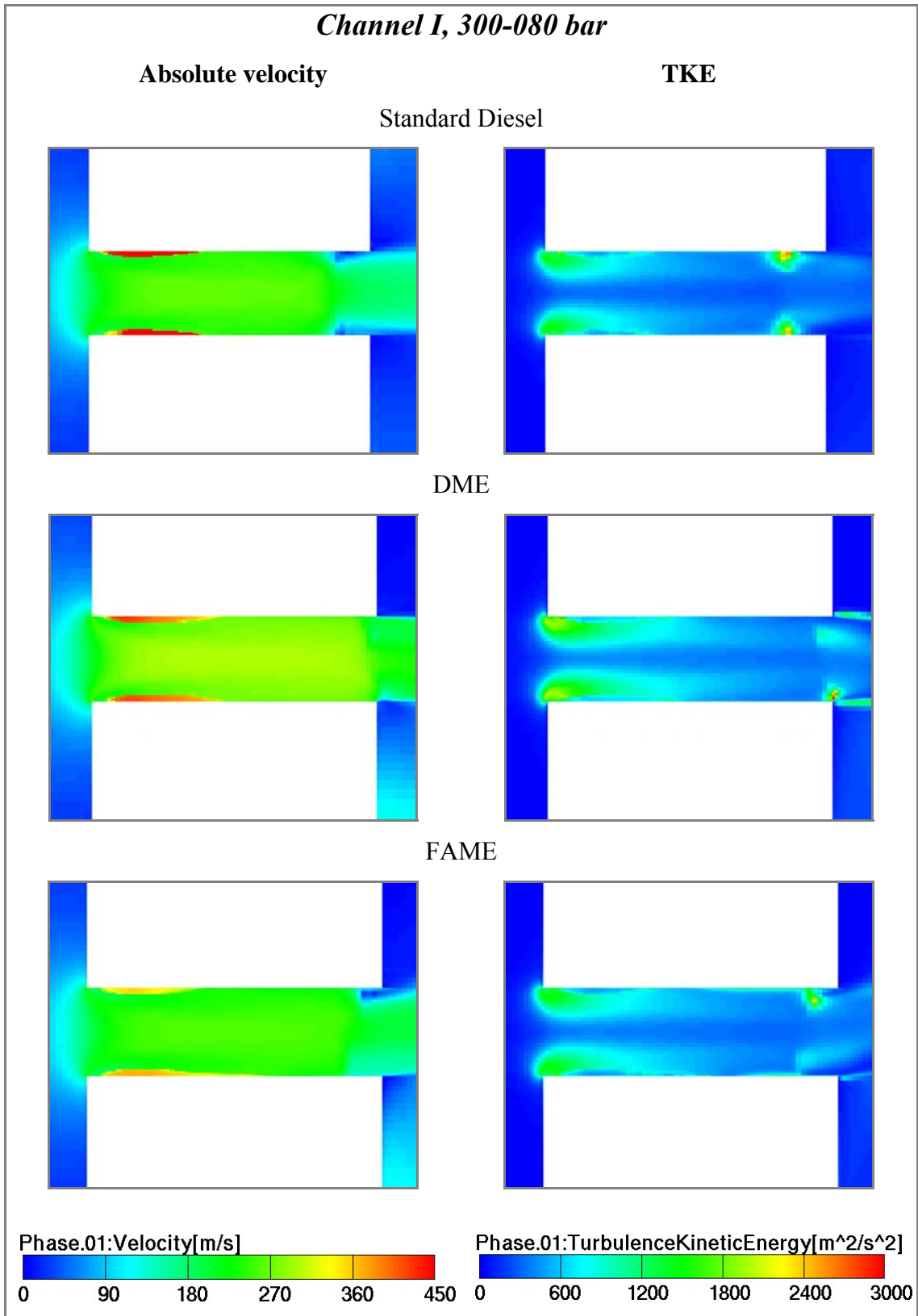


Figure 6.11 Channel I, 300-080bar comparison: velocity and TKE distribution

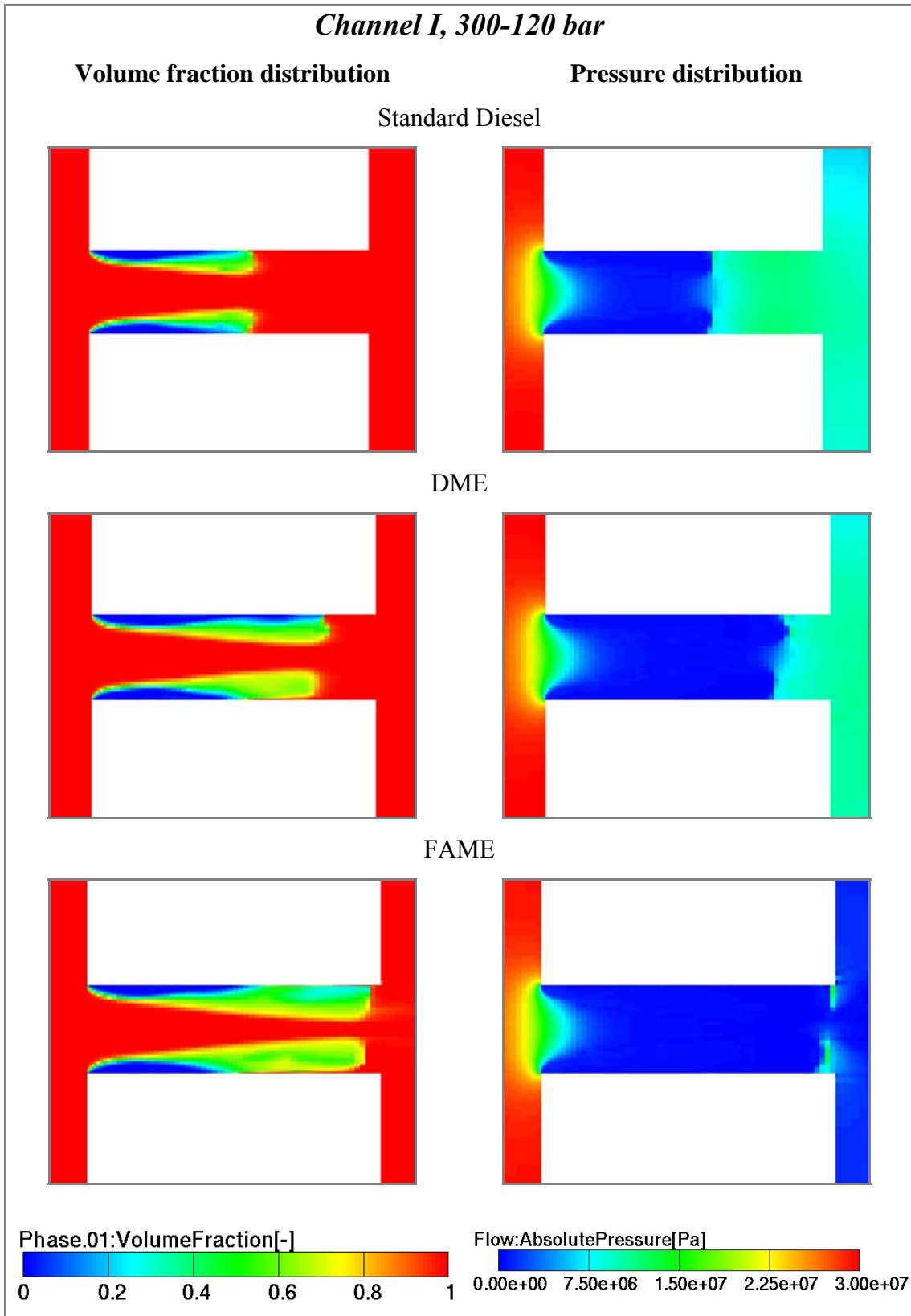


Figure 6.12 Channel I, 300-120bar comparison: volume fraction and absolute pressure distribution

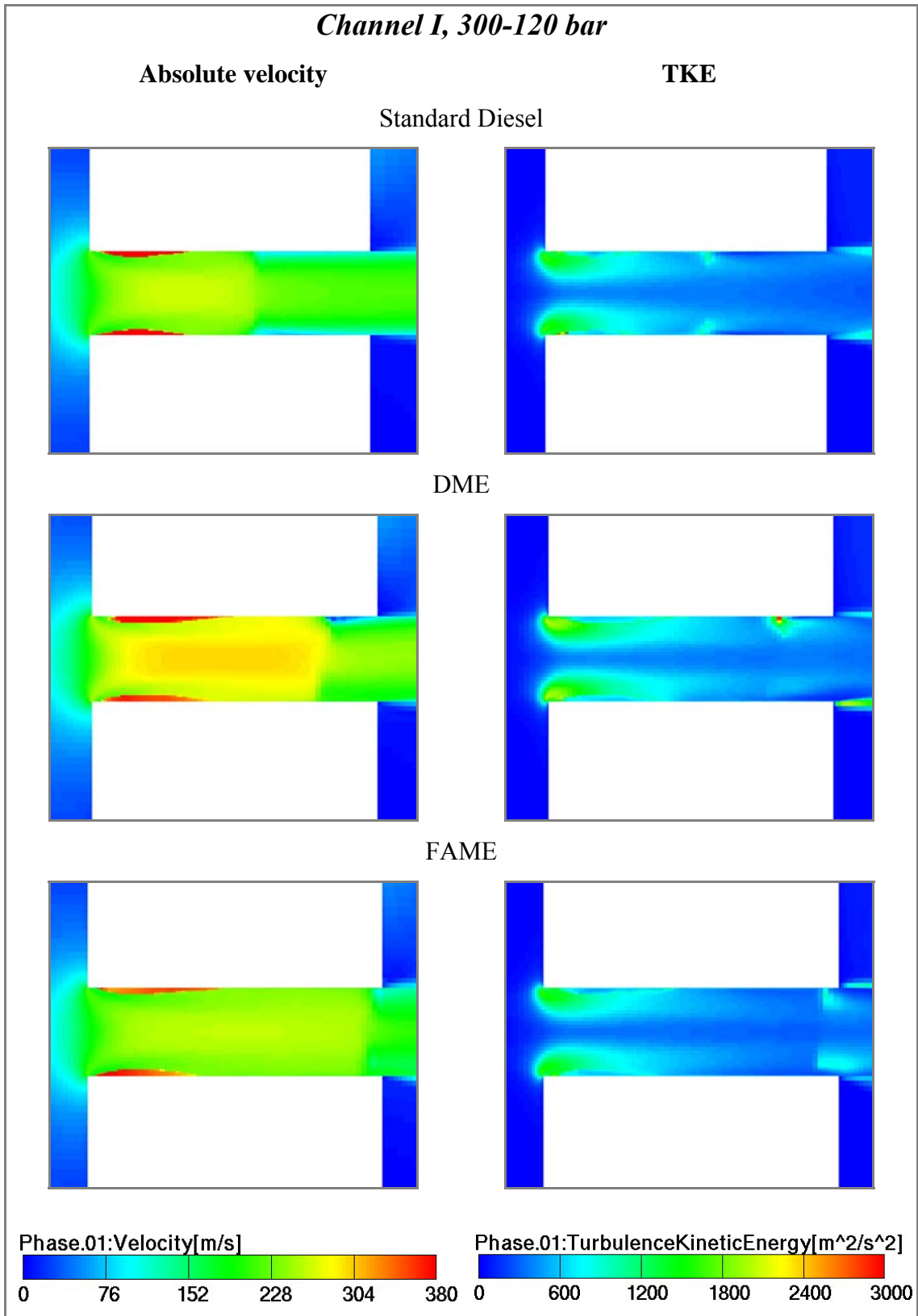


Figure 6.13 Channel I, 300-120bar comparison: velocity and TKE distribution

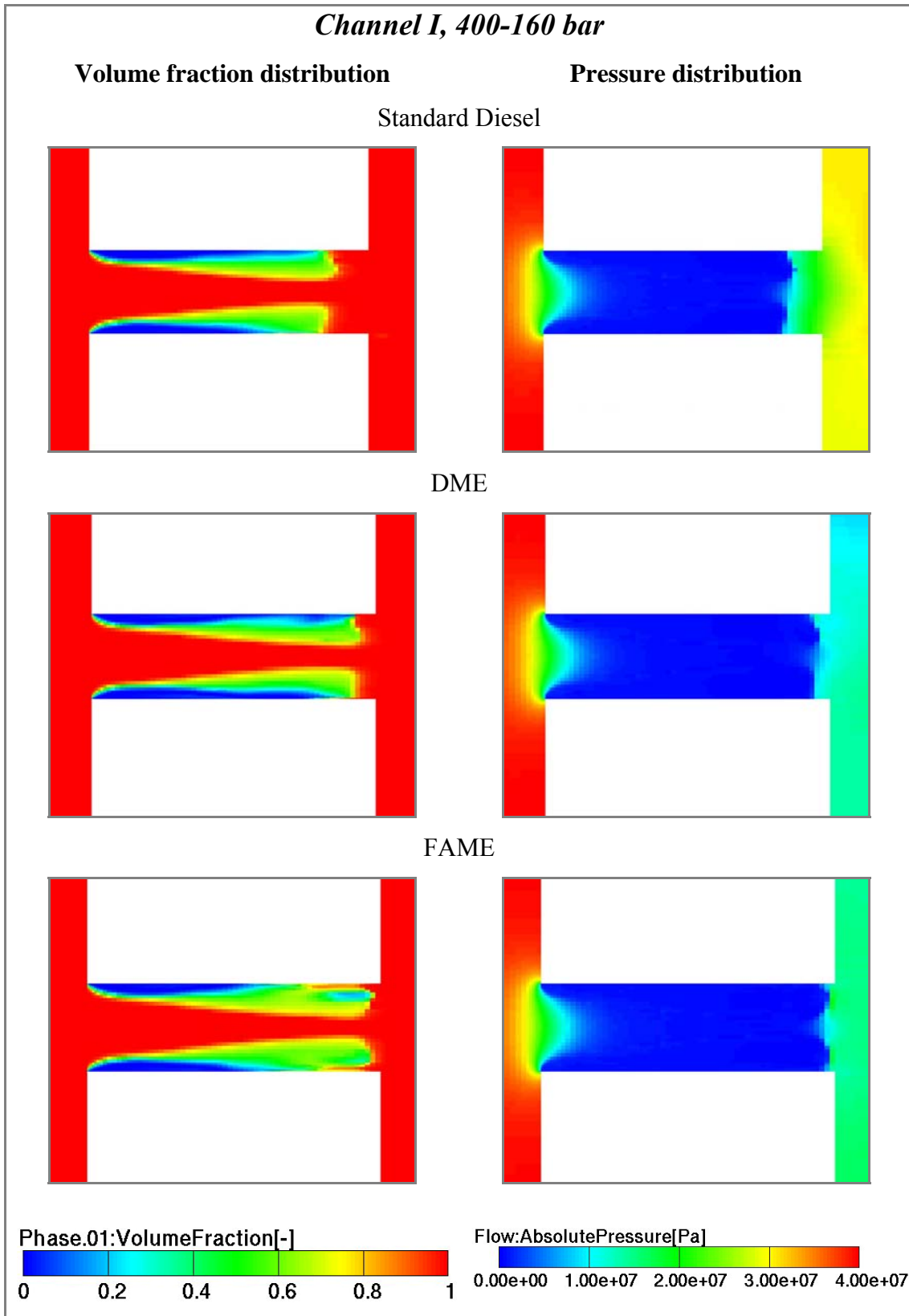


Figure 6.14 Channel I, 400-160bar comparison: volume fraction and absolute pressure distribution

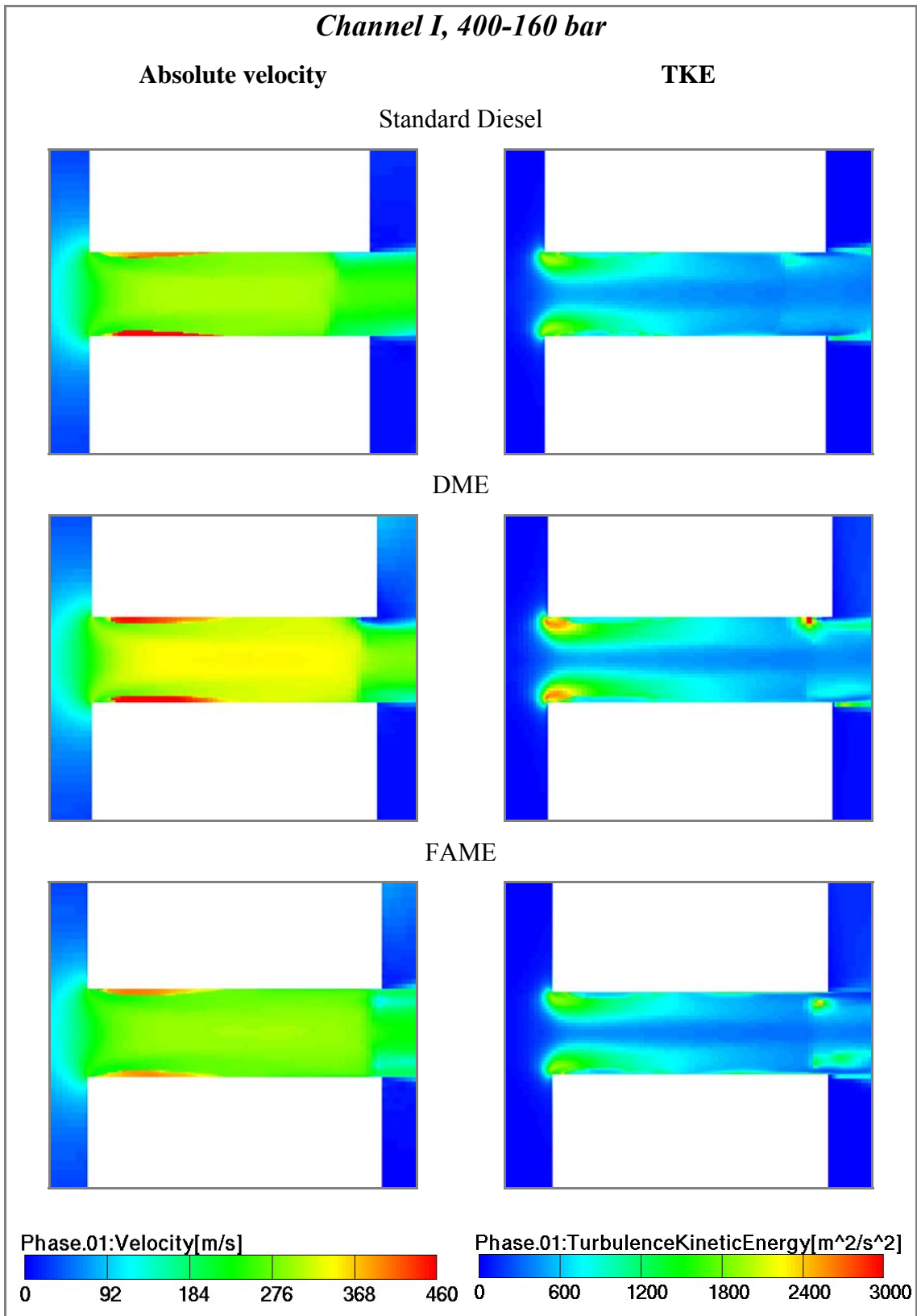


Figure 6.15 Channel I, 400-160bar comparison: velocity and TKE distribution

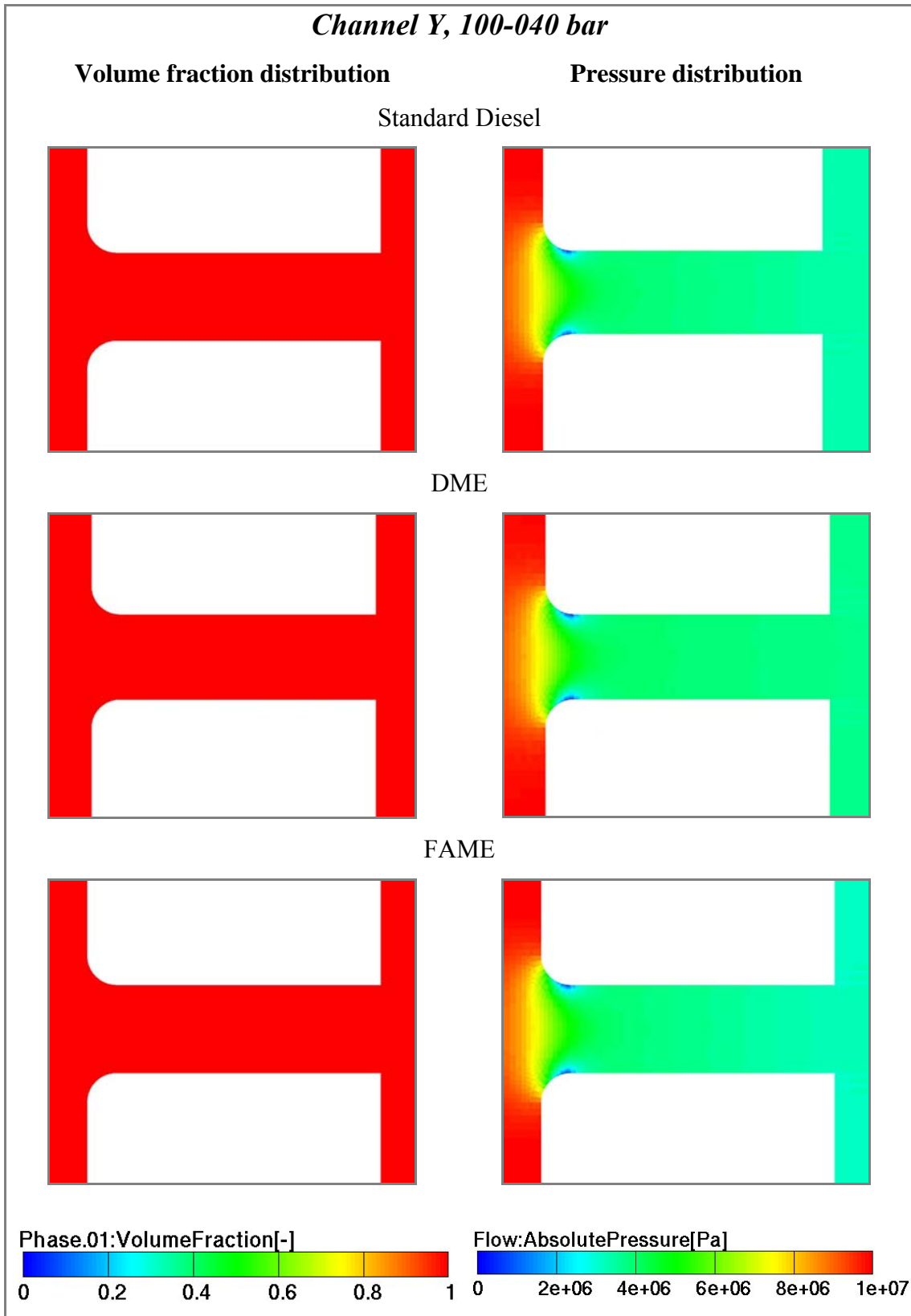


Figure 6.16 Channel Y, 100-040bar comparison: volume fraction and absolute pressure distribution

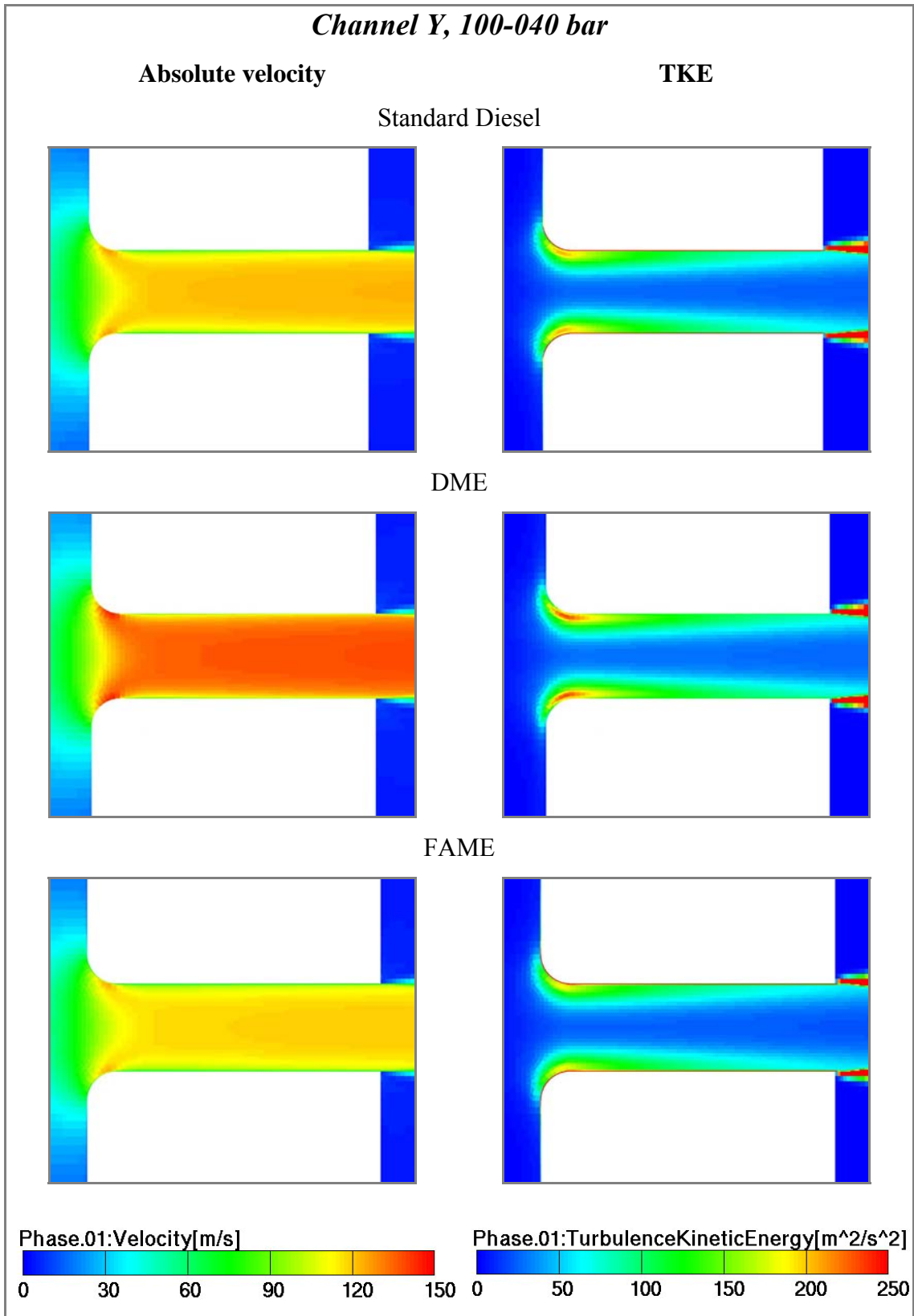


Figure 6.17 Channel Y, 100-040bar comparison: velocity and TKE distribution

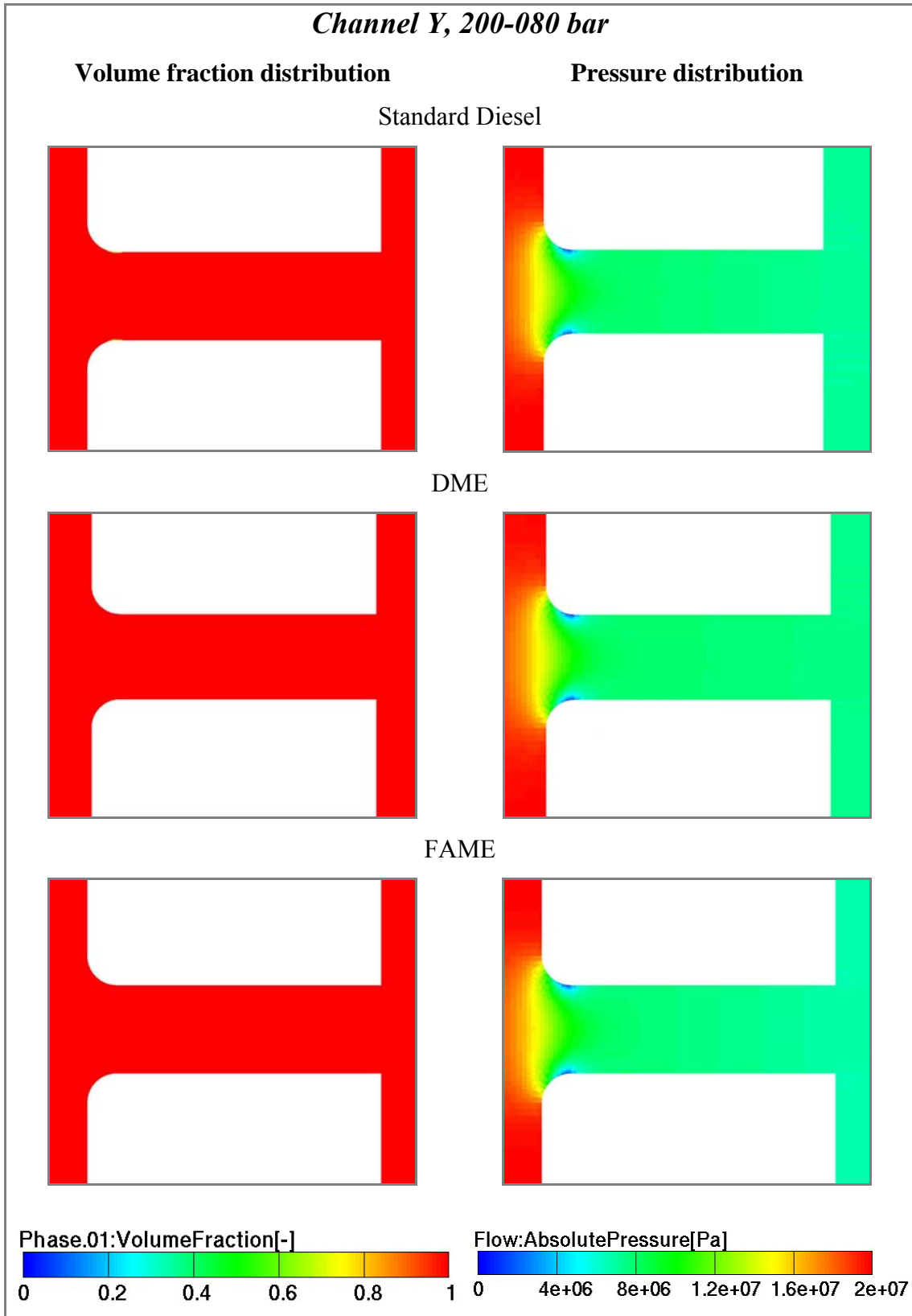


Figure 6.18 Channel Y, 200-080bar comparison: volume fraction and absolute pressure distribution

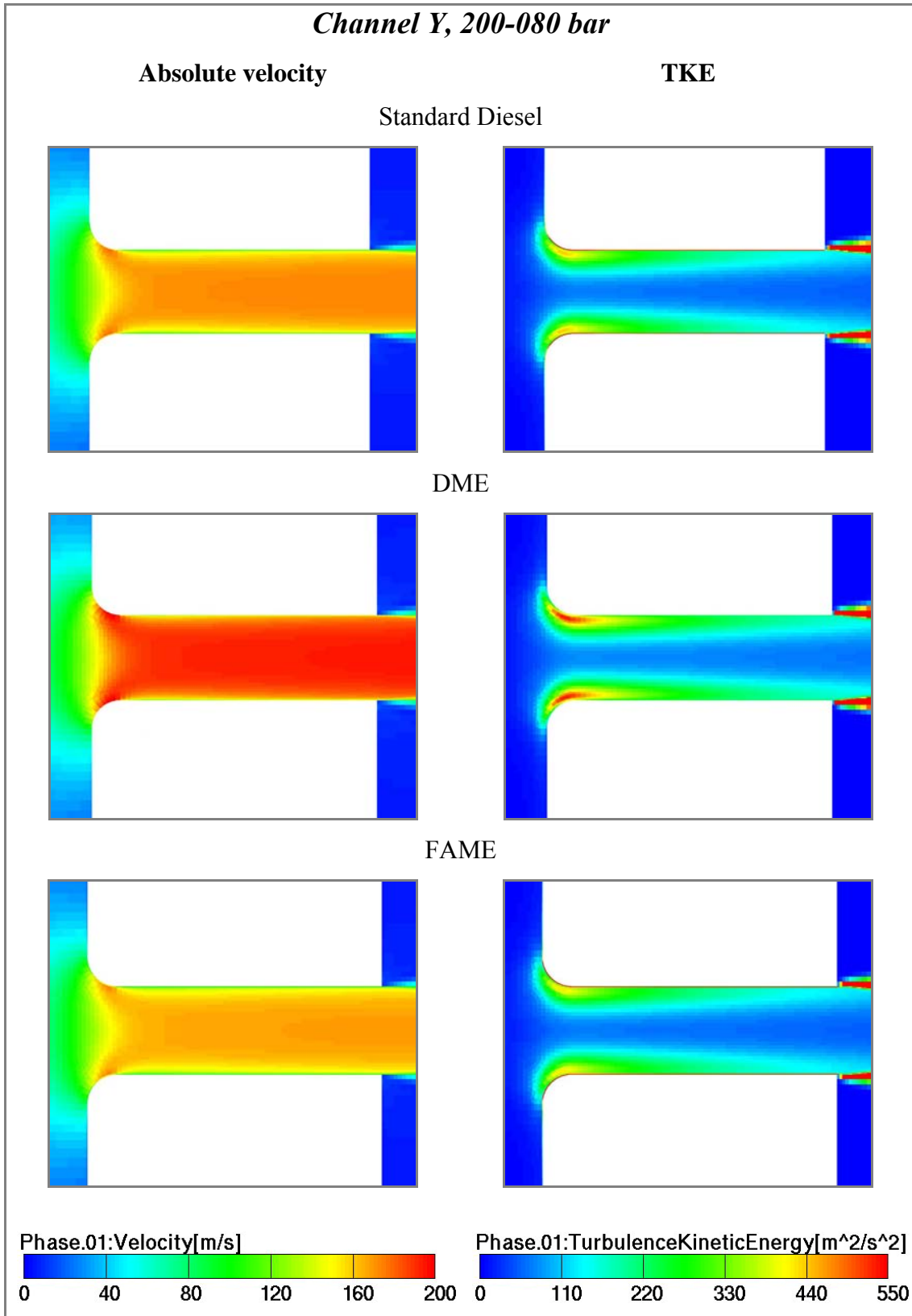


Figure 6.19 Channel Y, 200-080bar comparison: velocity and TKE distribution

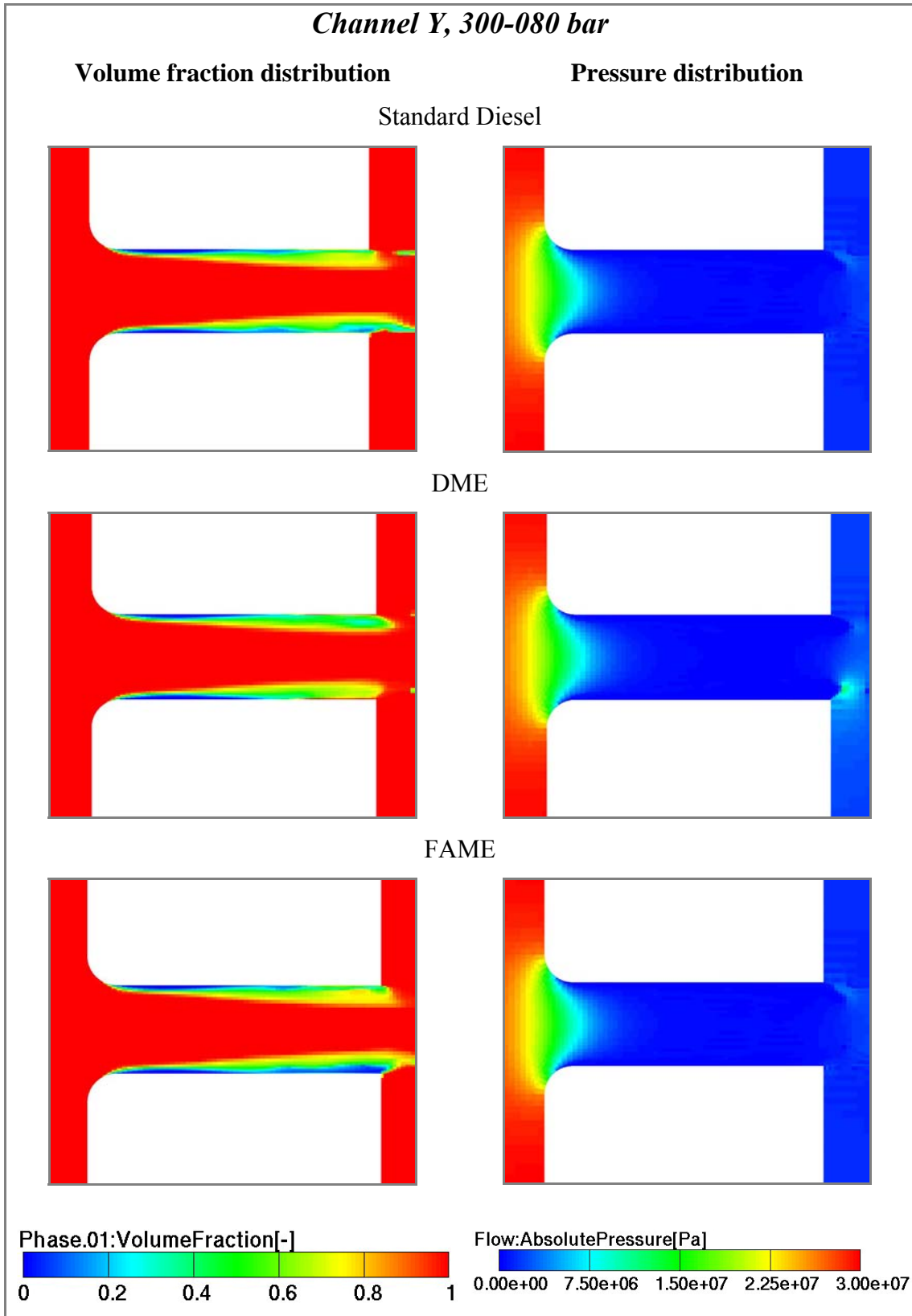


Figure 6.20 Channel Y, 300-080bar comparison: volume fraction and absolute pressure distribution

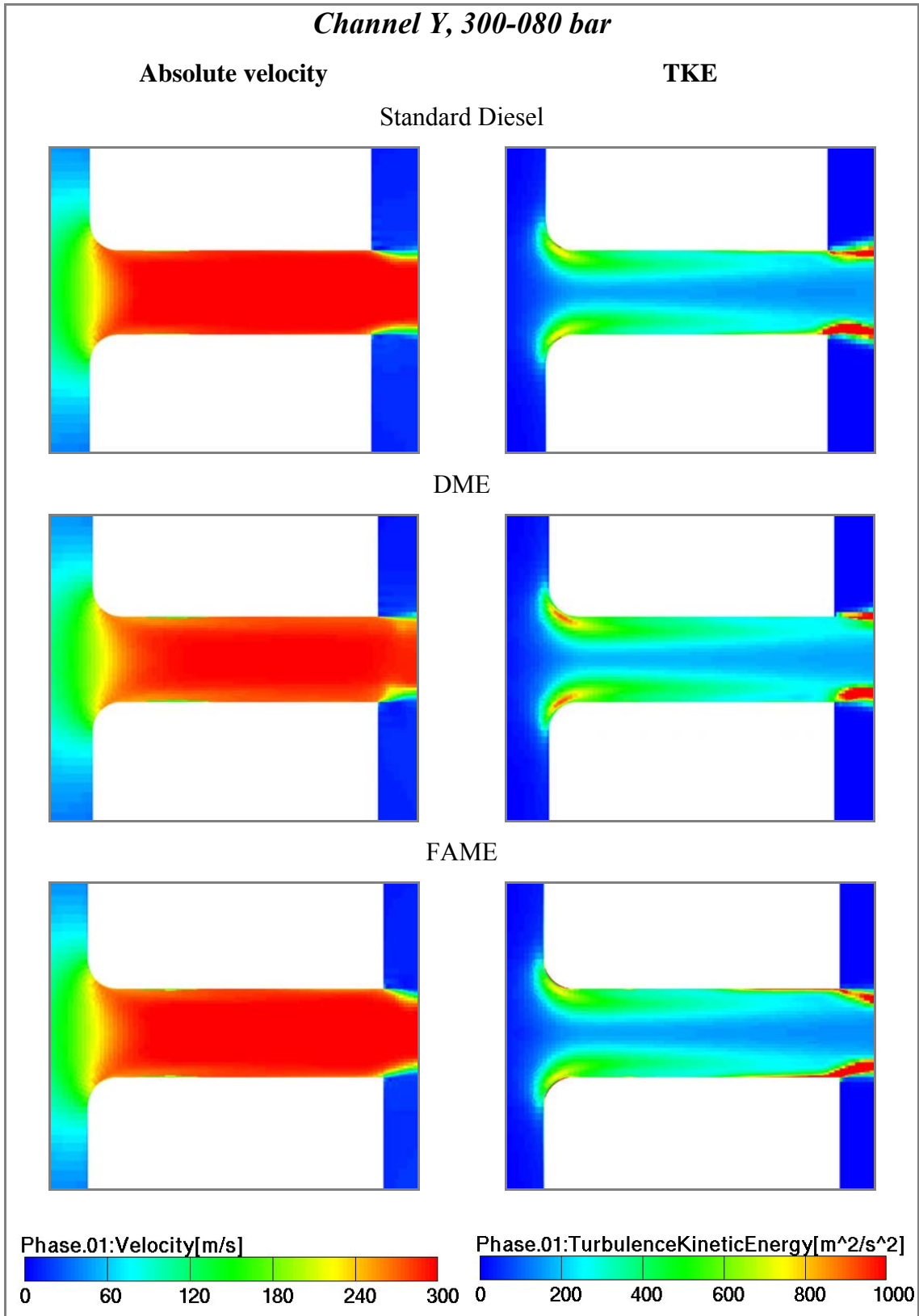


Figure 6.21 Channel Y, 300-080bar comparison: velocity and TKE distribution

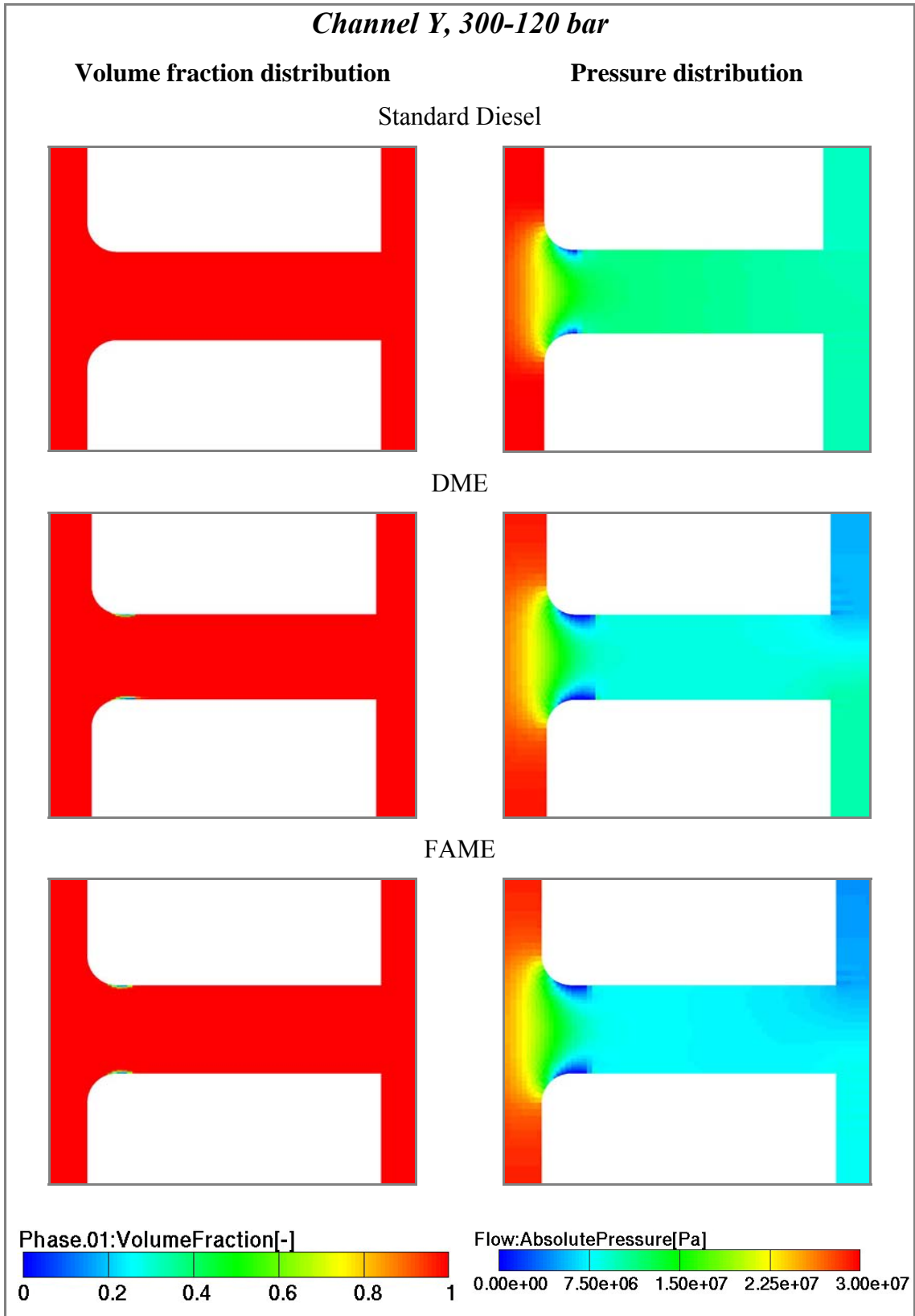


Figure 6.22 Channel Y, 300-120bar comparison: volume fraction and absolute pressure distribution

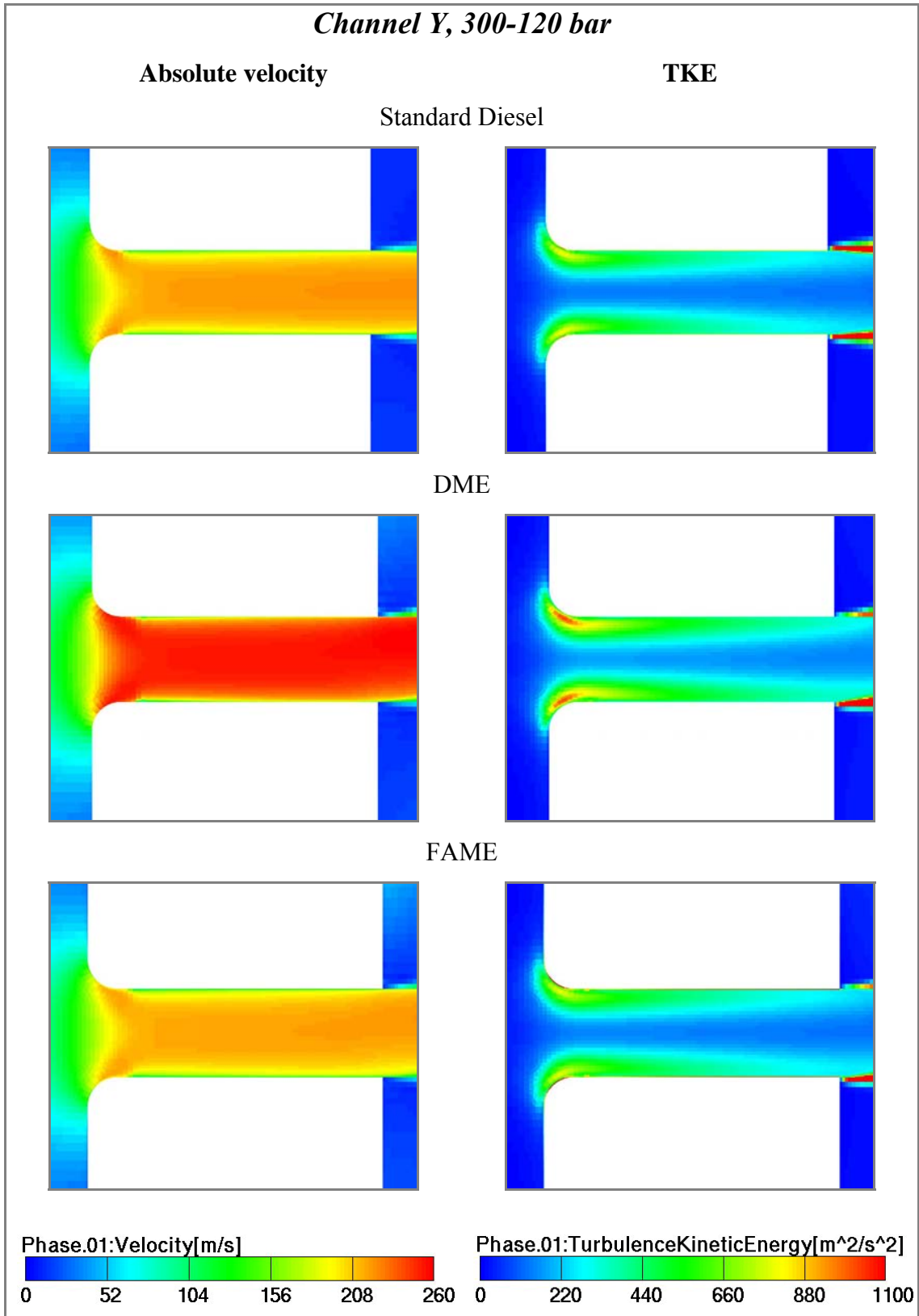


Figure 6.23 Channel Y, 300-120bar comparison: velocity and TKE distribution

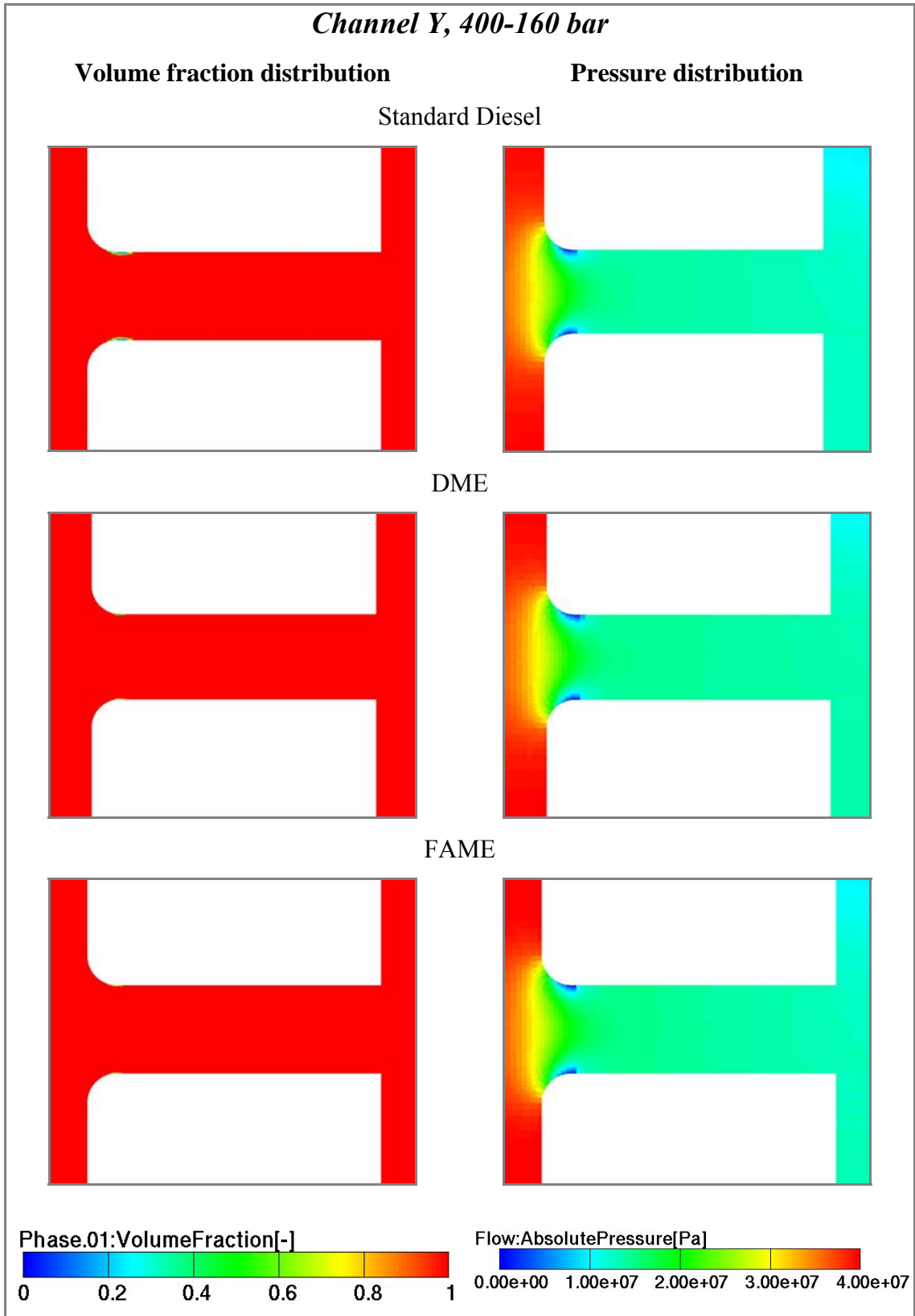


Figure 6.24 Channel Y, 400-160bar comparison: volume fraction and absolute pressure distribution

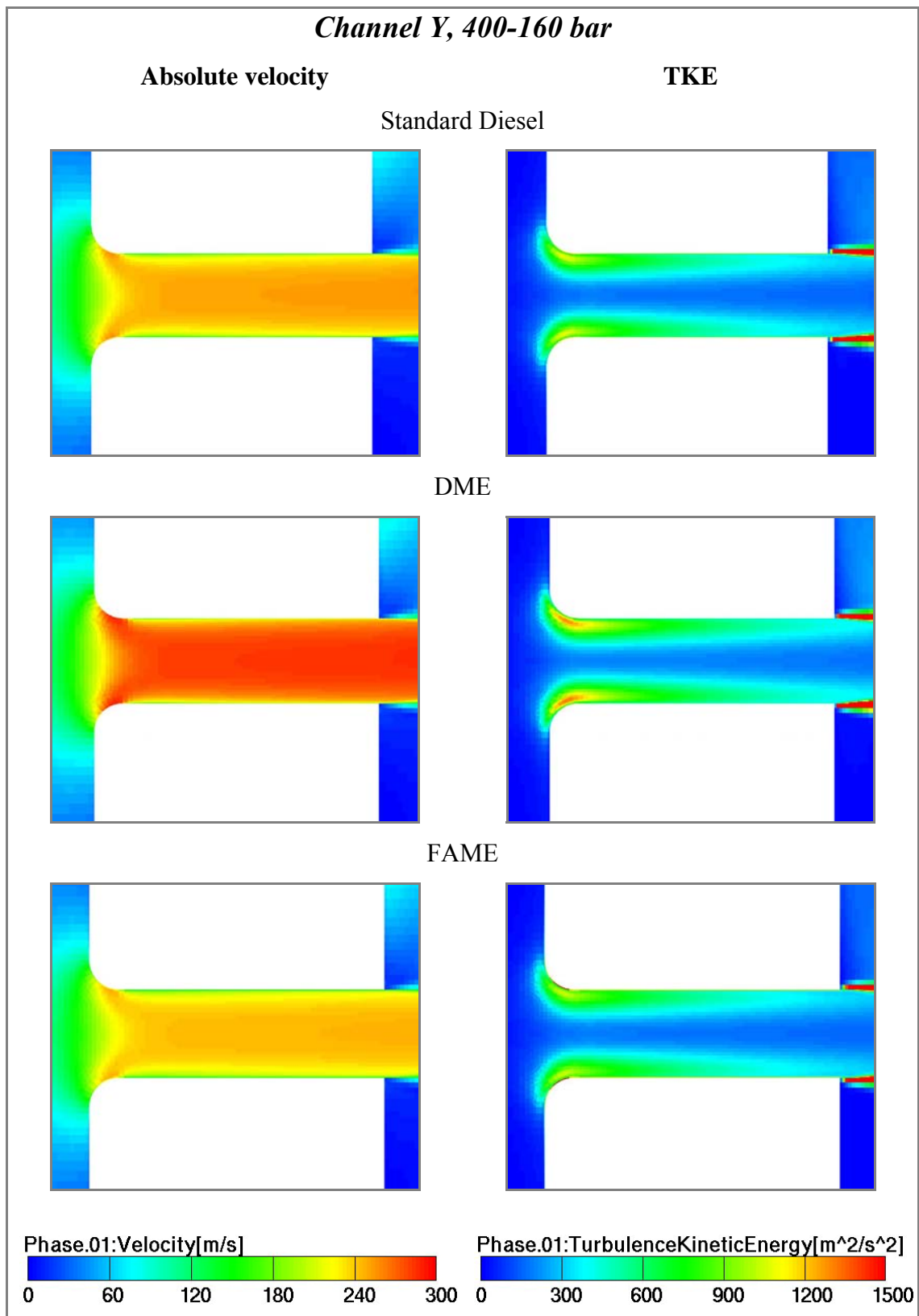


Figure 6.25 Channel Y, 400-160bar comparison: velocity and TKE distribution

6.2.3. Mass flow rate

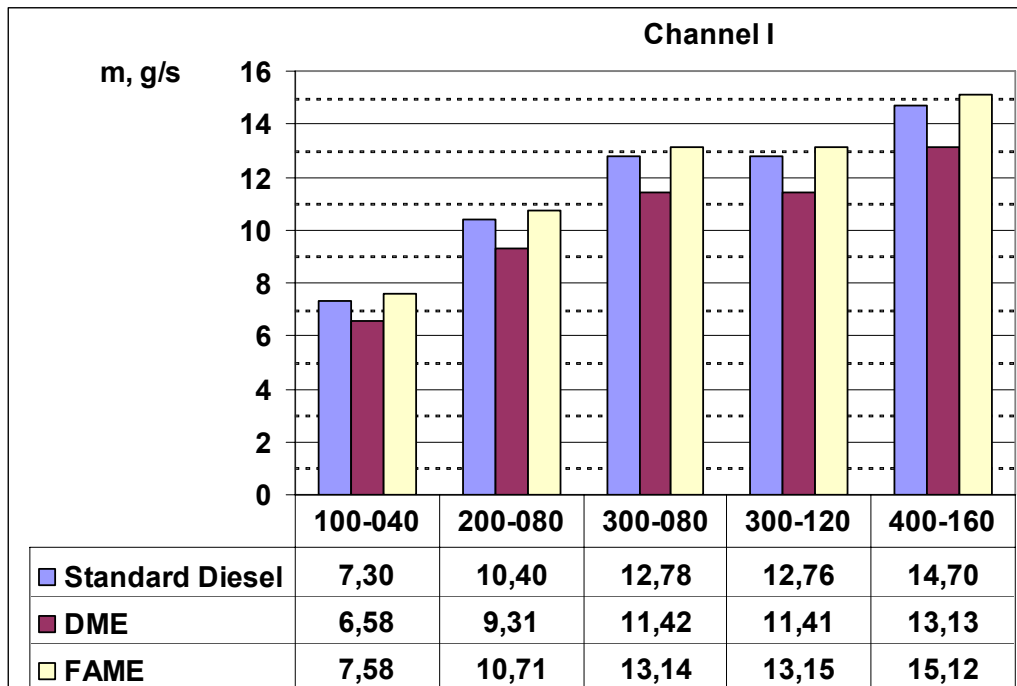


Figure 6.26 Channel I: mass flow rate

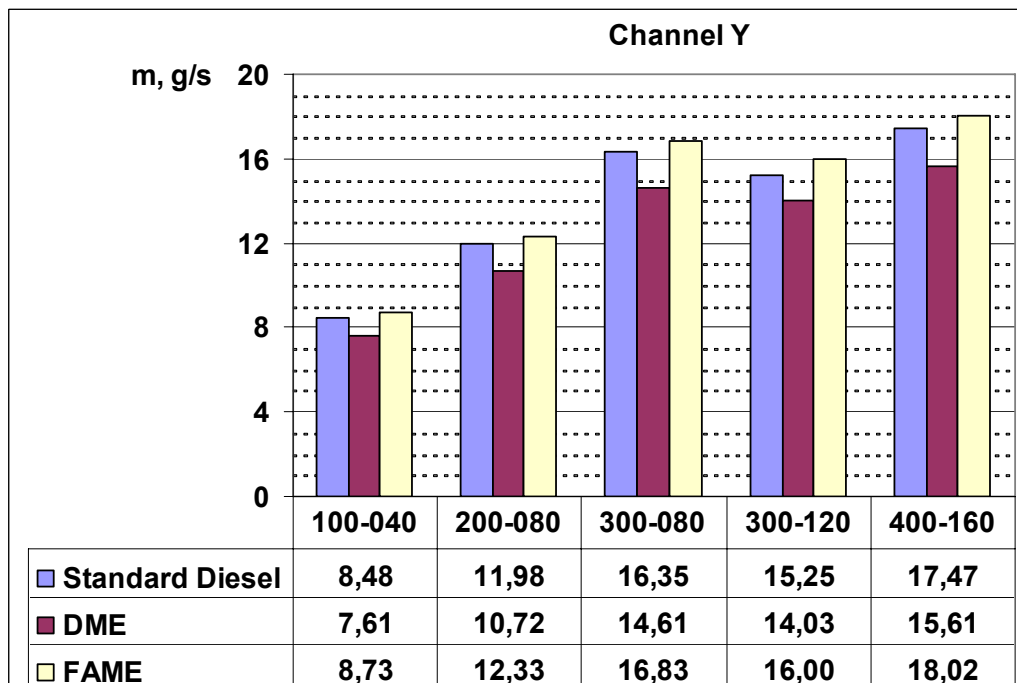


Figure 6.27 Channel Y: mass flow rate

6.2.4. Erosion incubation time and M DPR

Results were taken on Erosion selections, which were along narrow channel wall.

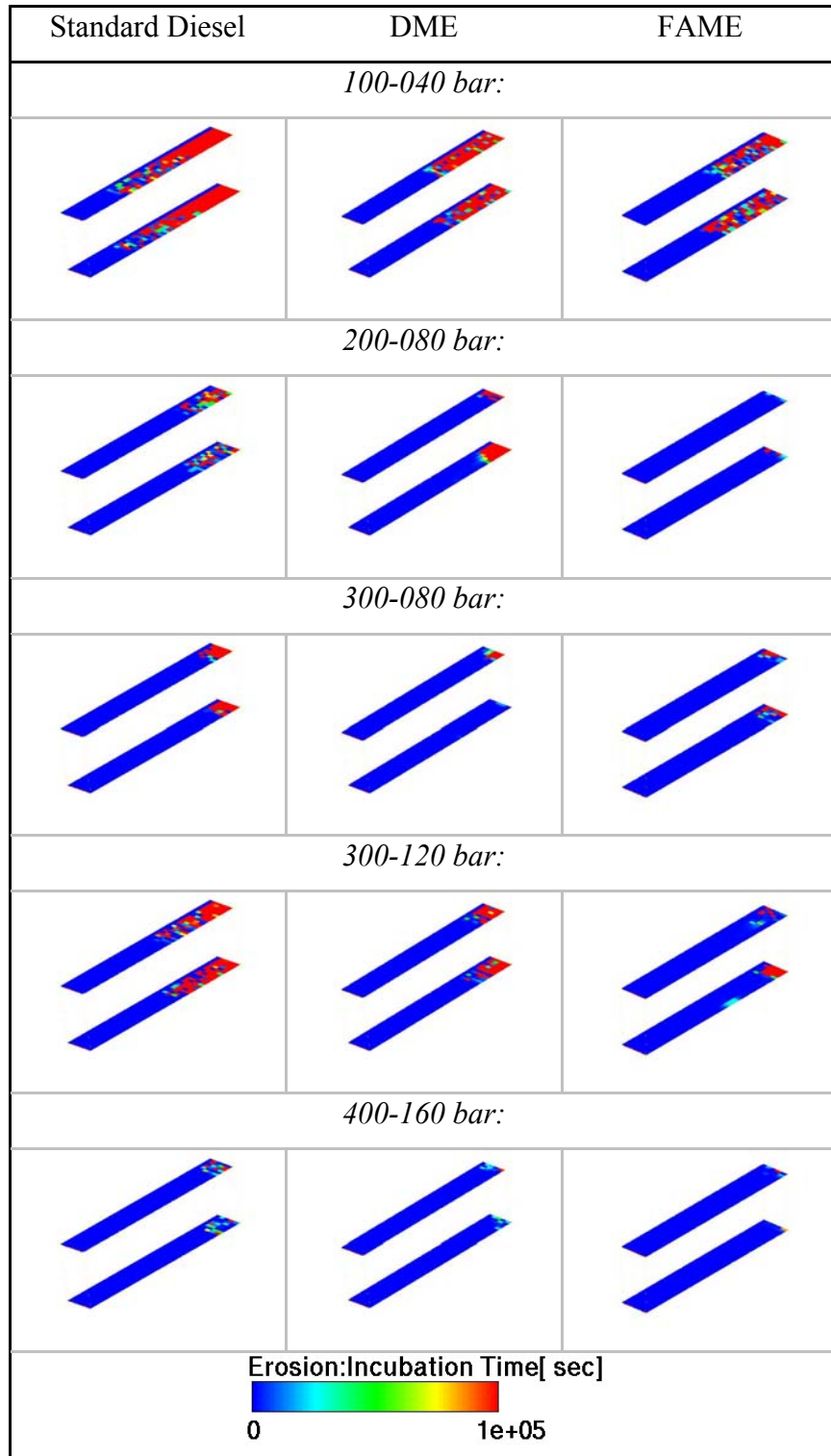


Figure 6.28 Channel I: erosion incubation time

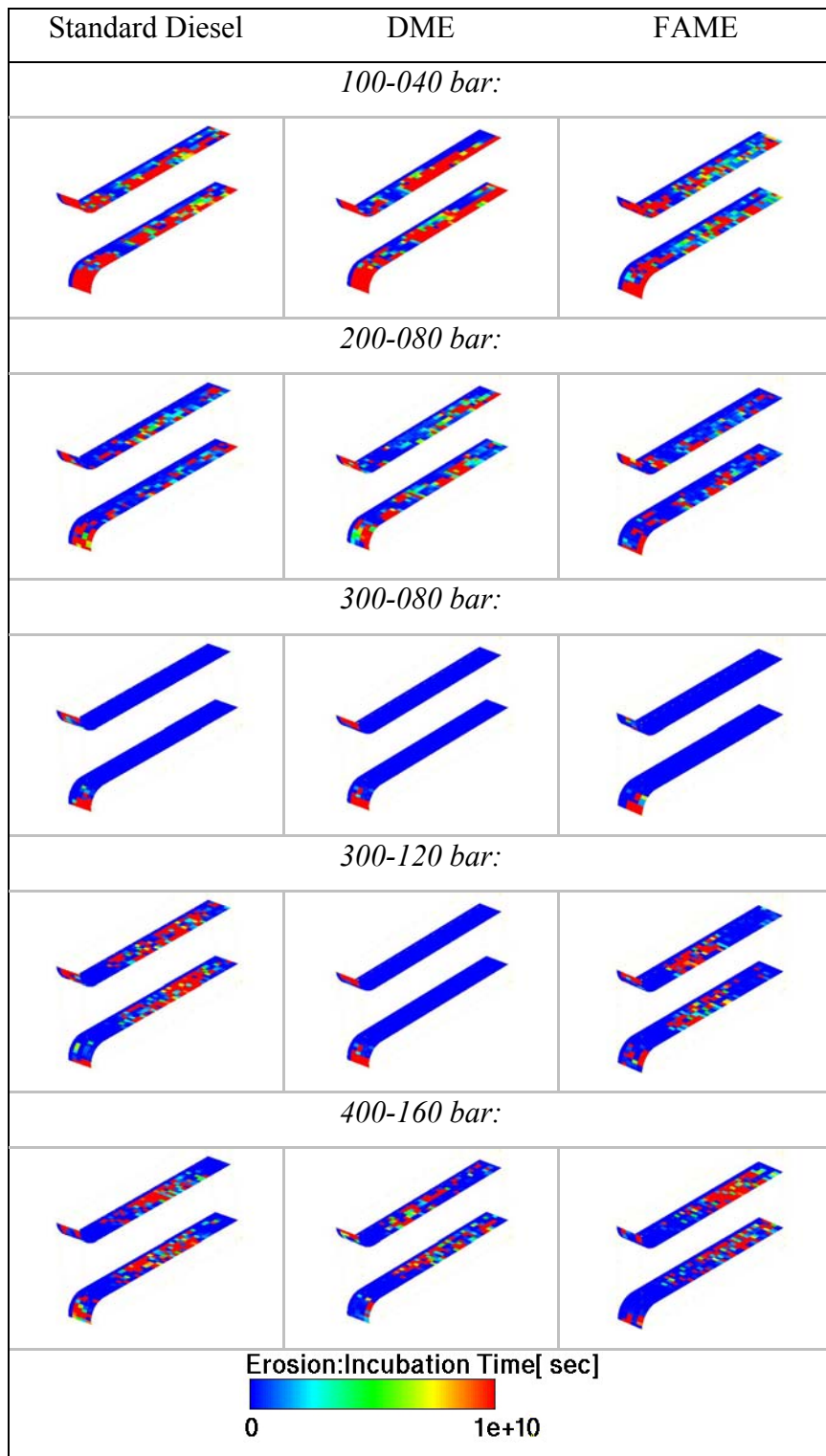


Figure 6.29 Channel Y: erosion incubation time

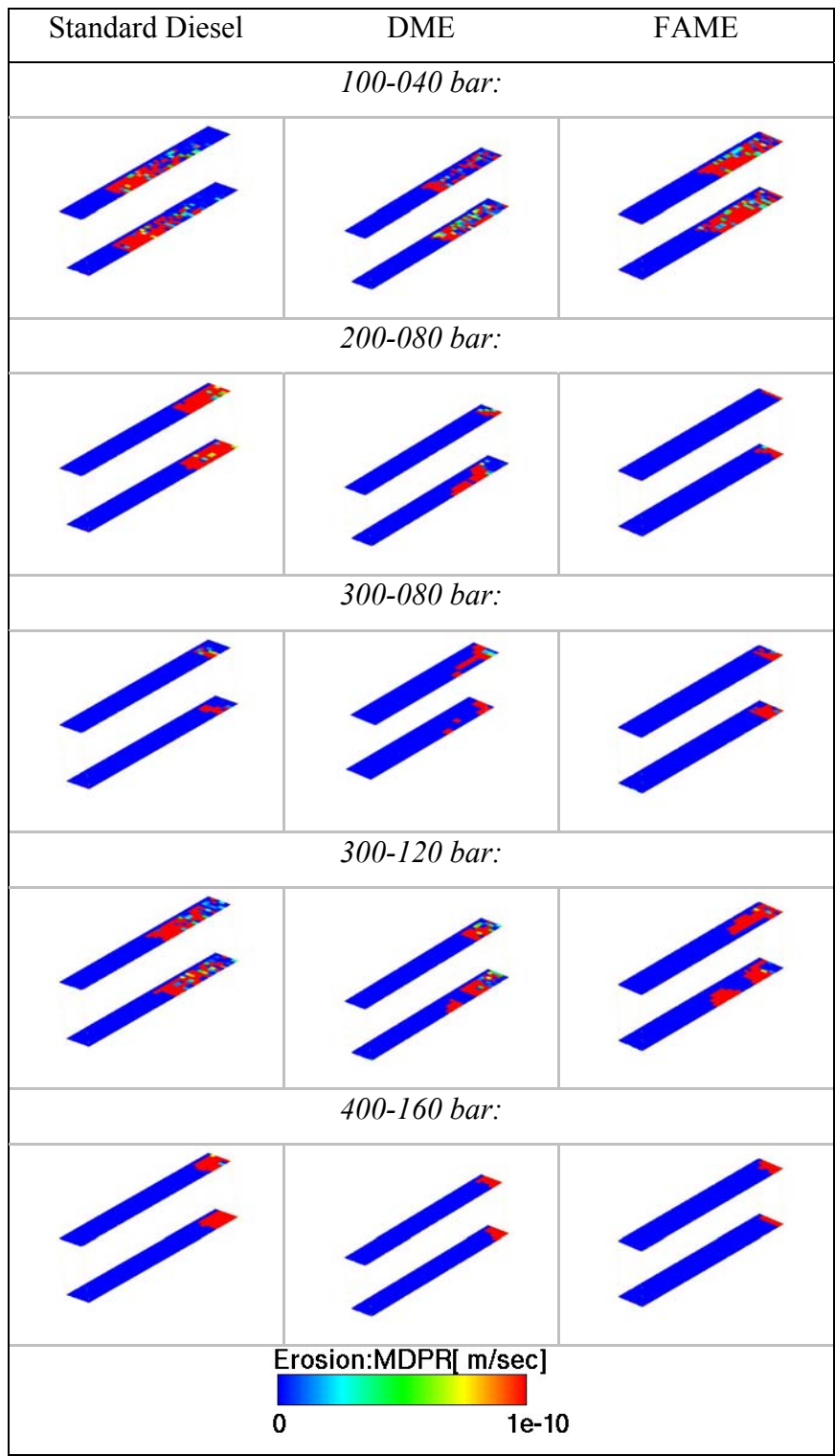


Figure 6.30 Channel I: MDPR

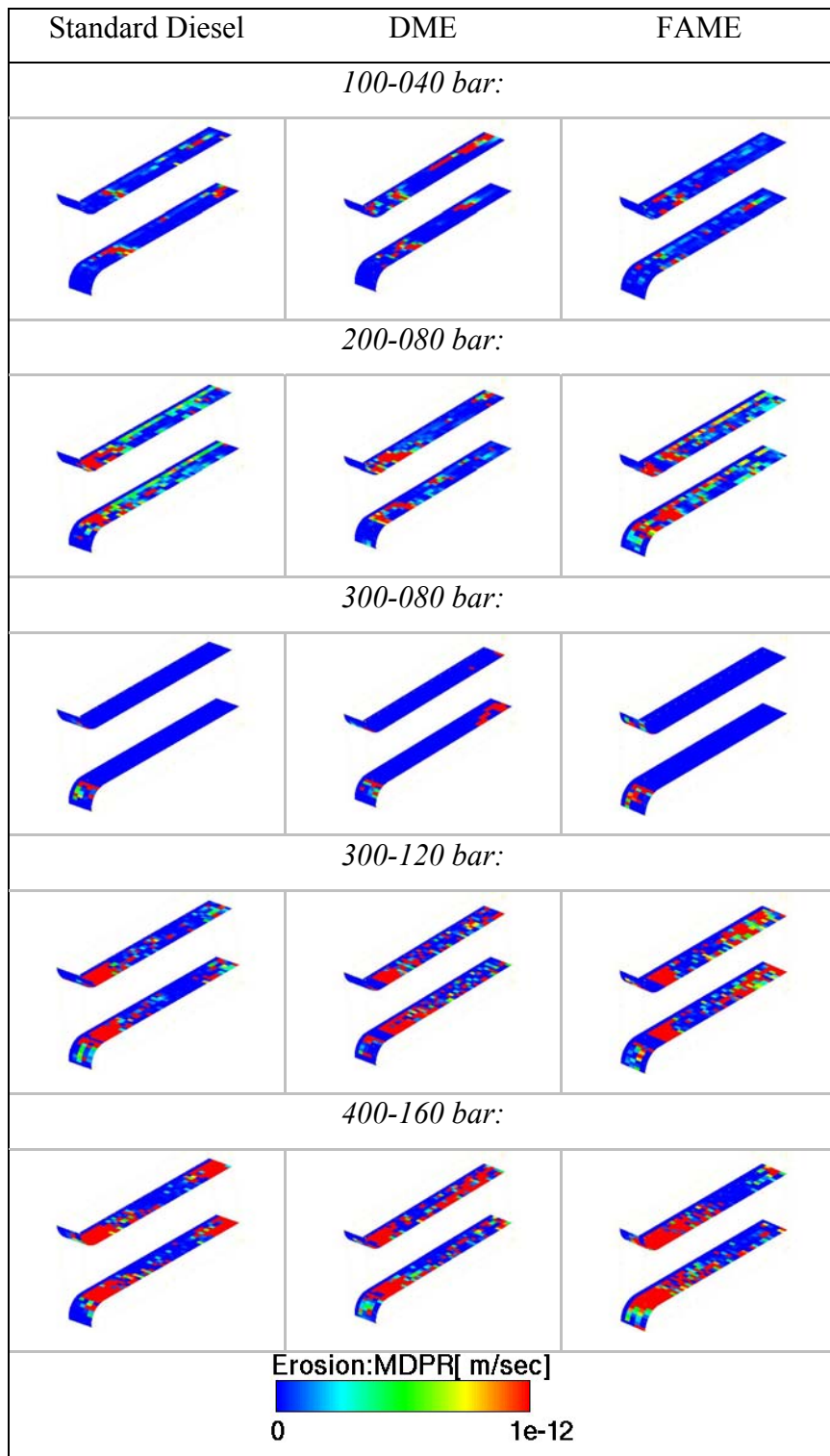


Figure 6.31 Channel Y: MDPR

6.2.5. Velocity profiles vs. narrow channel height

Velocity profiles were taken along polyline near narrow channel exit, as presented in following figure. Polyline is placed on symmetry plane.

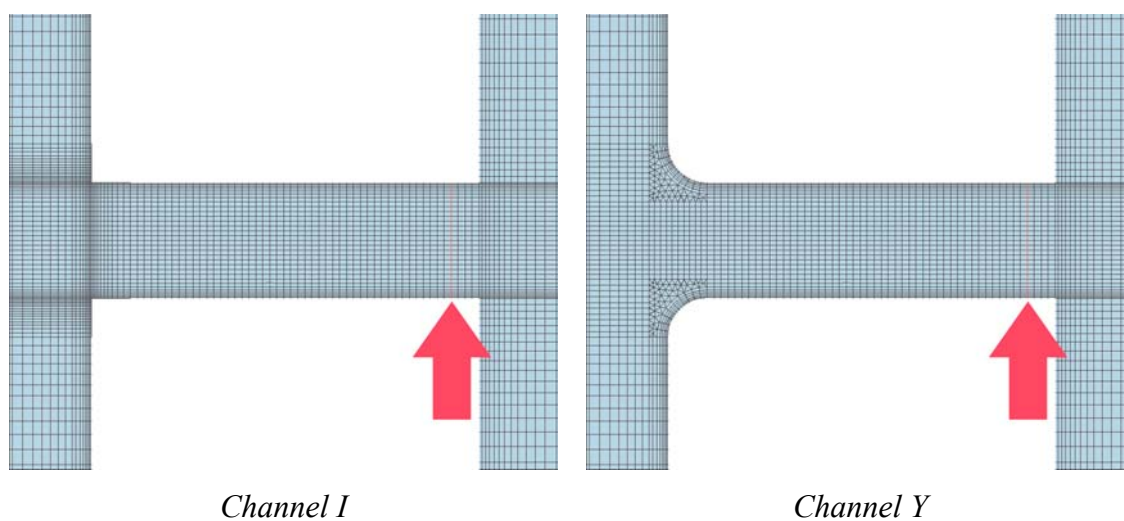


Figure 6.32 Channel flow: location of polyline on which velocity profiles were taken

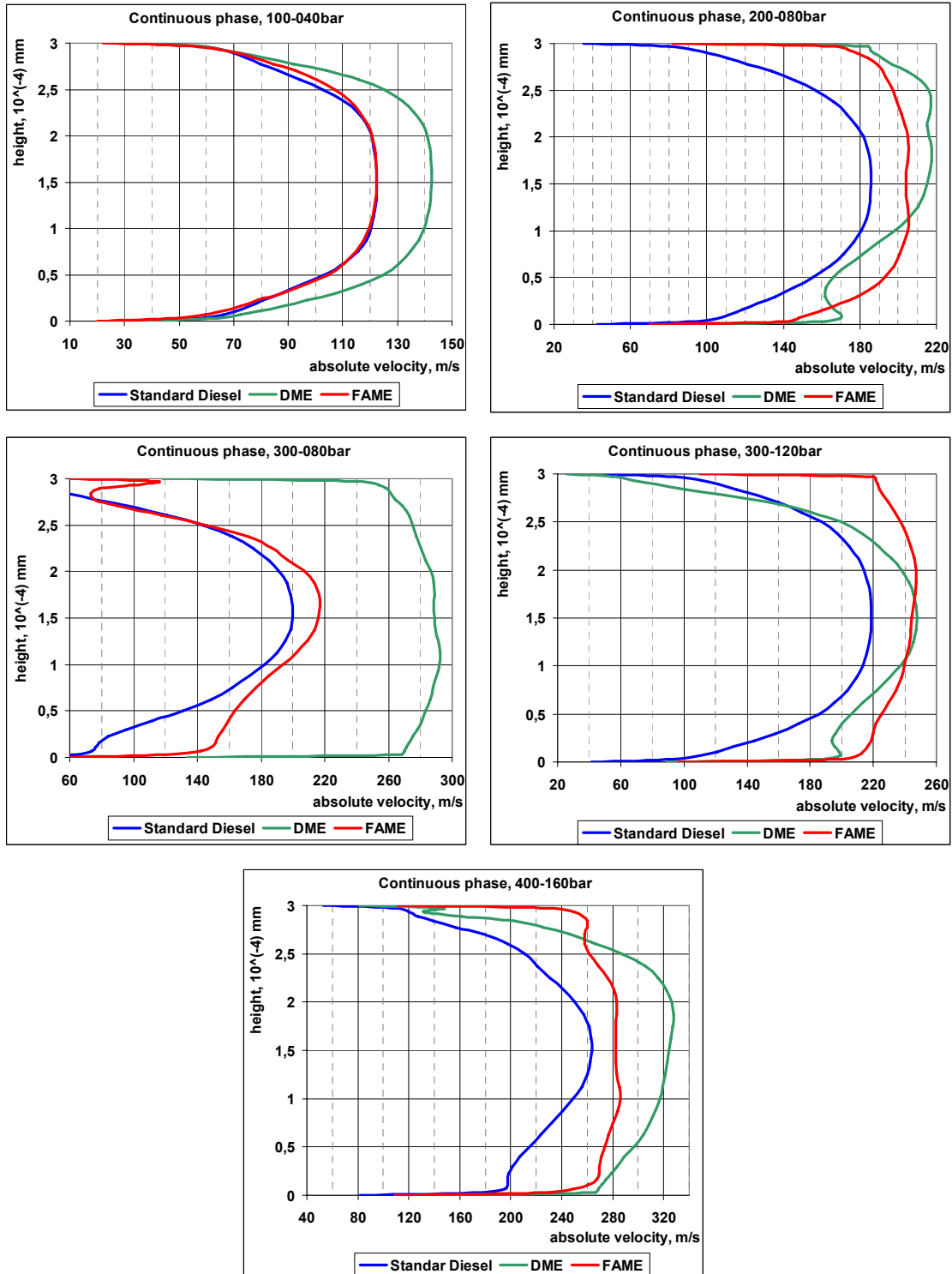


Figure 6.33 Channel I comparison: velocity profiles vs. narrow channel height

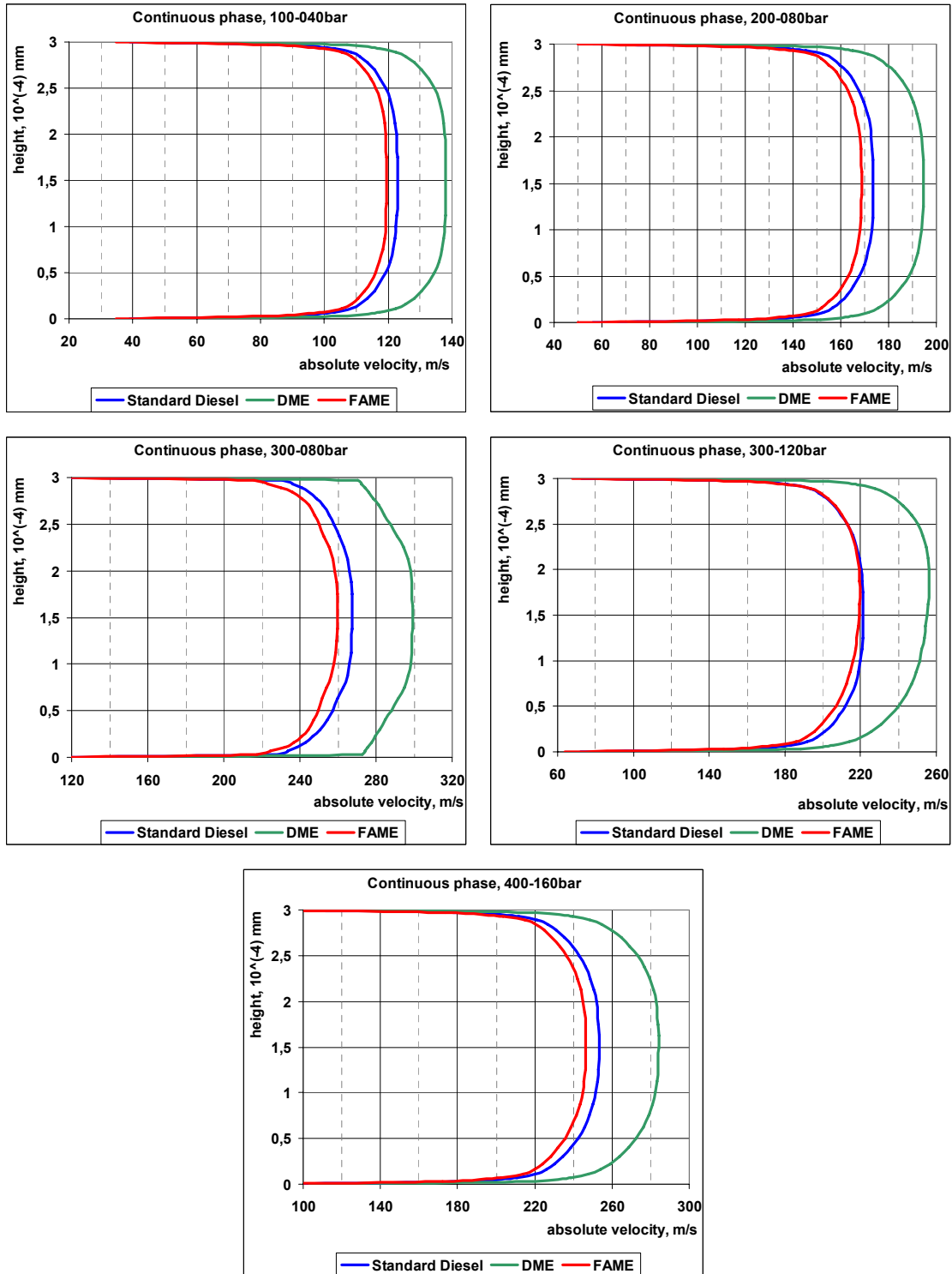


Figure 6.34 Channel I comparison: velocity profiles vs. narrow channel height

6.2.6. Channel I results analysis

Cavitation length, for all cases, is for Standard diesel shortest and for FAME longest. Cavitation thickness is approximately the same for all fuels. Absolute pressure distribution shows intense pressure drop in narrow channel inlet, where cavitation in all cases starts. In regions near narrow channel outlet, pressure rises and cavitation vanishes i.e. condensation occurs. Absolute velocity distribution shows that DME fuel achieves highest values in all cases. TKE distribution shows relatively similar result for all fuels, but it should be mentioned that in two cases DME fuel had slightly higher values near narrow channel inlet. Generally, TKE values are higher on narrow channel inlet, as well as on distance of cavitation length where condensation of bubbles is present.

Mass flow rate, *Figure 6.26*, shows that FAME fuel has highest, and DME fuel has lowest value. Values for standard fuel are slightly lower than the ones for FAME.

Erosion incubation time distribution, *Figure 6.28*, shows highest values in regions that are free from cavitation. This is logical, due to a fact that erosion is more intense in areas with more bubbles because of better chance for its implosion/condensation. MDP, *Figure 6.30*, shows that biggest values are around regions where cavitation vanishes. This could be due to positive pressure gradient at those regions that “forces” bubbles to implode.

Velocity profiles near narrow channel exit, *Figure 6.33*, point on fact that flow inside I channel is undeveloped, except for 100-001bar case. This is due to extensive vorticity of the flow caused by sharp narrow channel inlet. In most cases DME fuel achieves highest velocity.

6.2.7. Channel Y result analysis

By comparison with Channel I, in Channel Y we have very low cavitation, except for 300-080bar case. Absolute pressure drop is not so intensive as in Channel I cases, also with exception for 300-080bar case. Absolute velocity distribution shows same trend as Channel I cases, i.e. highest velocity for DME cases. Highest values of TKE

are close to rounded edge, also close to the inlet section. TKE is in all cases distributed near channel wall and is slightly decreasing along narrow channel length, with absolute value smaller than in Channel I.

It is interesting to observe 300-080bar case. Cavitation length and thickness is very similar for all fuels. Also, pressure distribution, absolute velocity and TKE are not different at all. This is contrary to all other case. All mentioned shows consistency between volume fraction and pressure distribution.

Mass flow rate, *Figure 6.27*, shows same trend, but higher values, when comparing with Channel I cases, regarding to fuels type.

Erosion incubation time distribution, *Figure 6.29*, is generally showing greater regions with higher erosion incubation time. MDPR, *Figure 6.31*, is greater on channel inlet and outlet zone.

Velocity profiles near narrow channel exit, *Figure 6.34*, suggest that flow is developed in all Channel Y cases. This could be explained with lower local pressure drop and vorticity of the flow which is direct contribution of rounded edge on narrow channel inlet. In all cases DME fuel achieves highest velocity. When comparing to Channel I, it can be observed that peak values are mostly similar.

6.3. Comparison of fuels: nozzle models with downstream placed target

6.3.1. Comparison criteria

Comparison criteria are same as in Chapter 6.3.2.

6.3.2. Volume fraction, pressure, velocity and TKE distribution

Since we are only interested in narrow channel zone, results are presented as following figure shows:

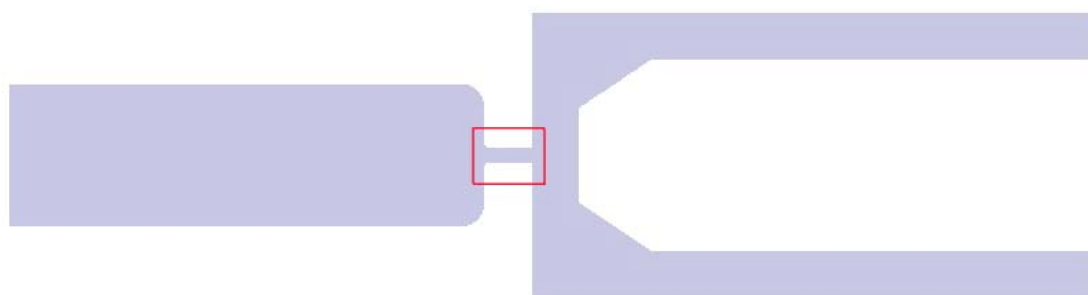


Figure 6.35 Target flow: area where distribution results are presented

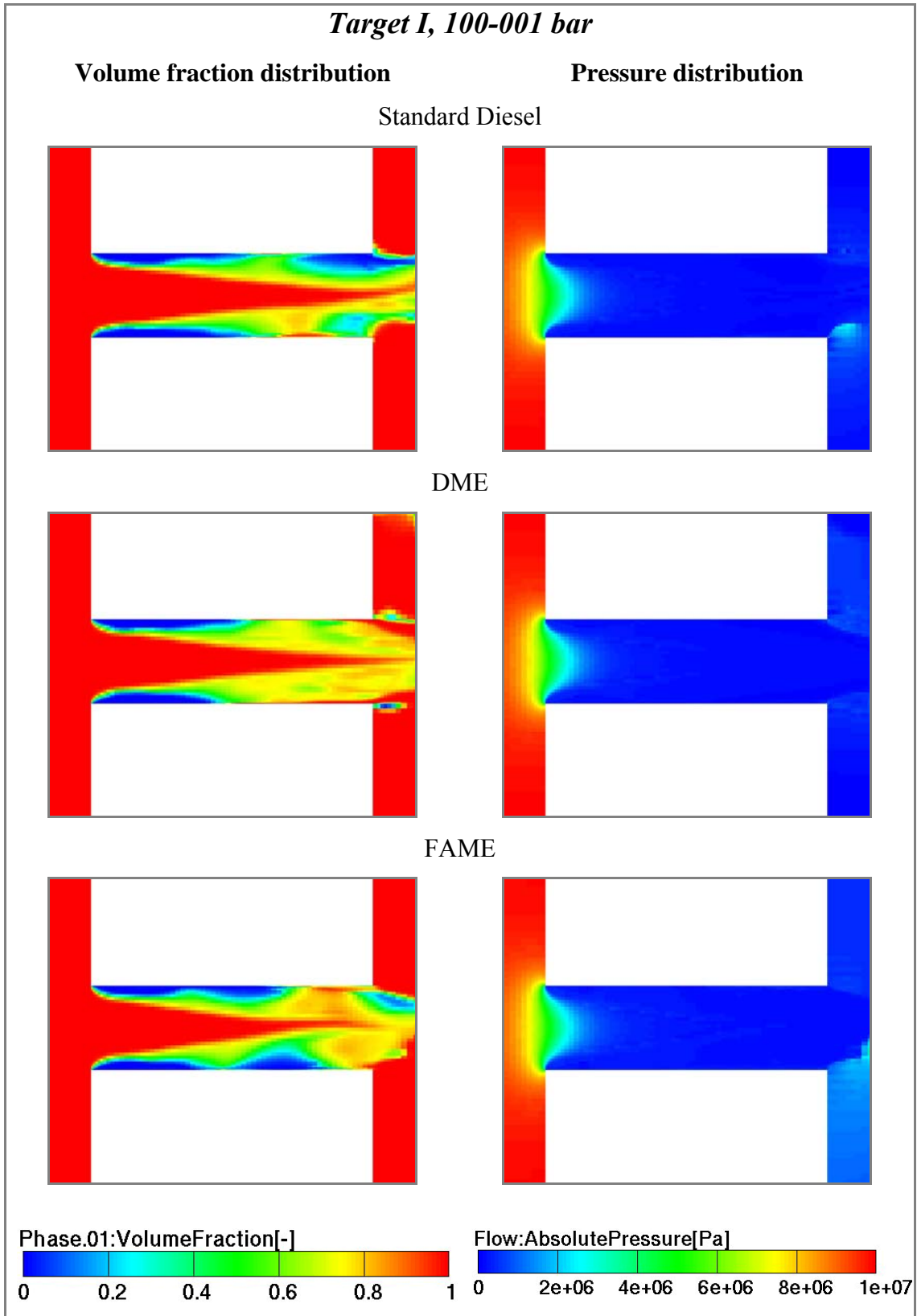


Figure 6.36 Target I, 100-001bar comparison: volume fraction and absolute pressure distribution

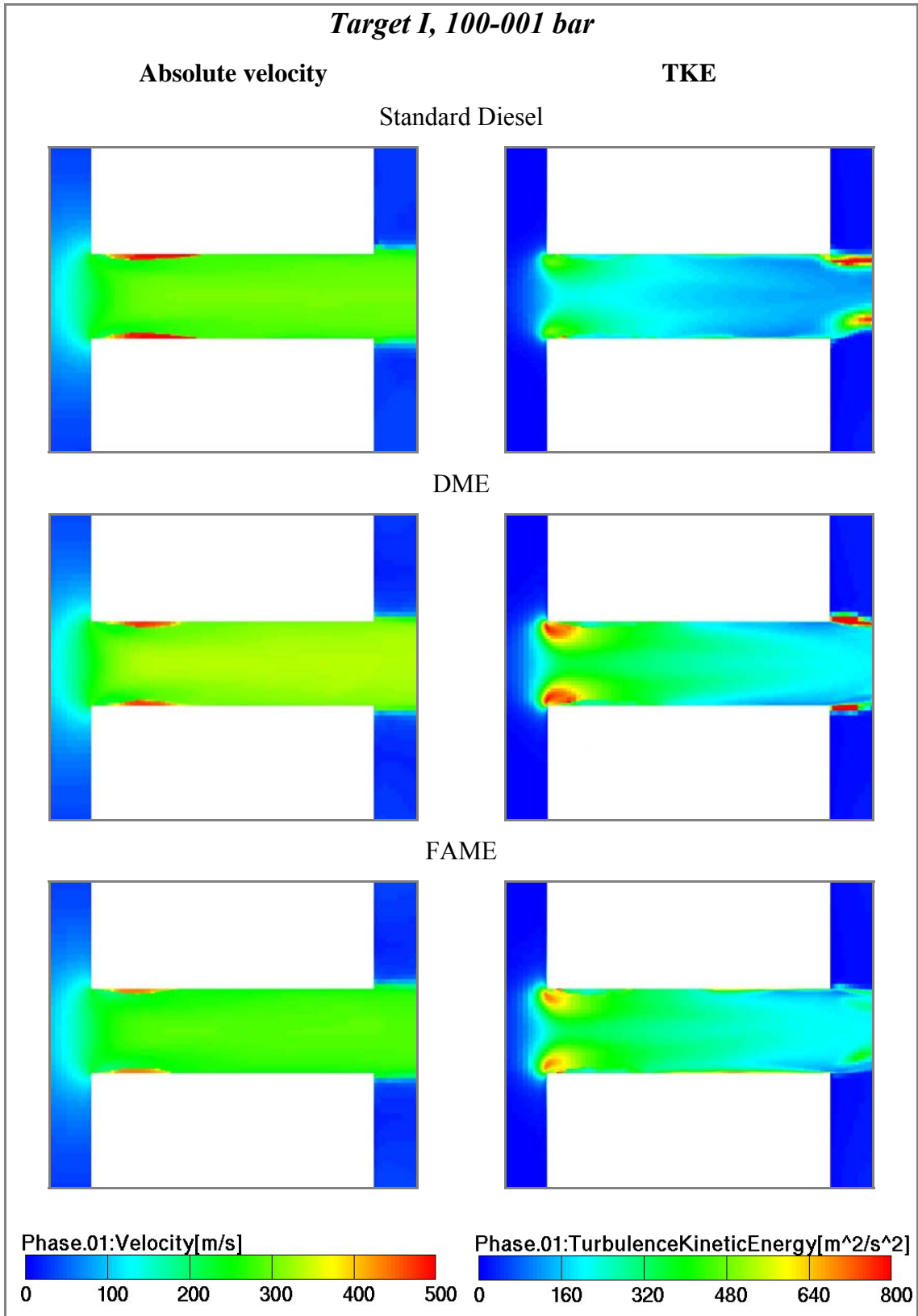


Figure 6.37 Target I, 100-001bar comparison: absolute velocity and TKE distribution

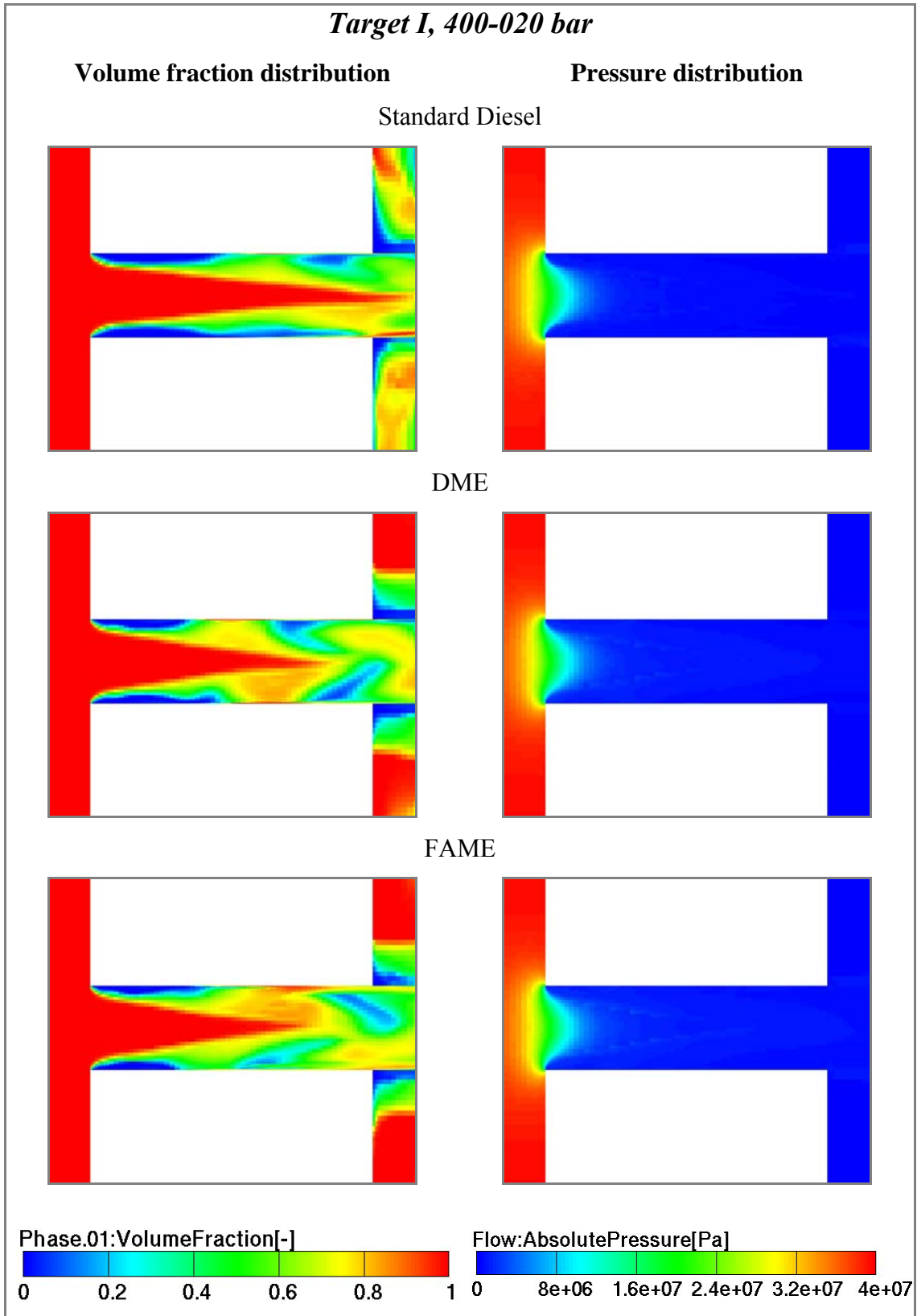


Figure 6.38 Target I, 400-020bar comparison: volume fraction and absolute pressure distribution

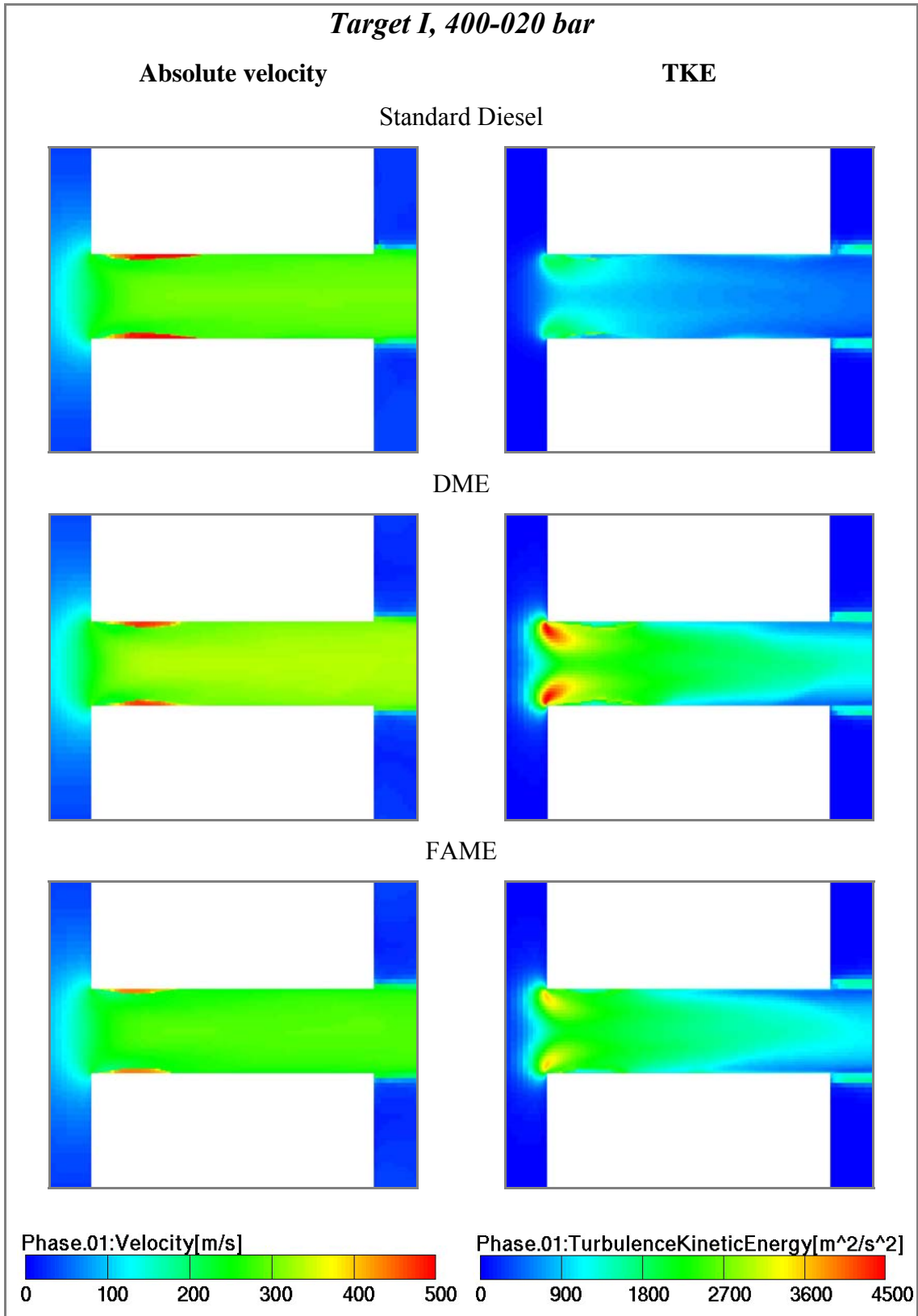


Figure 6.39 Target I, 400-020bar comparison: absolute velocity and TKE distribution

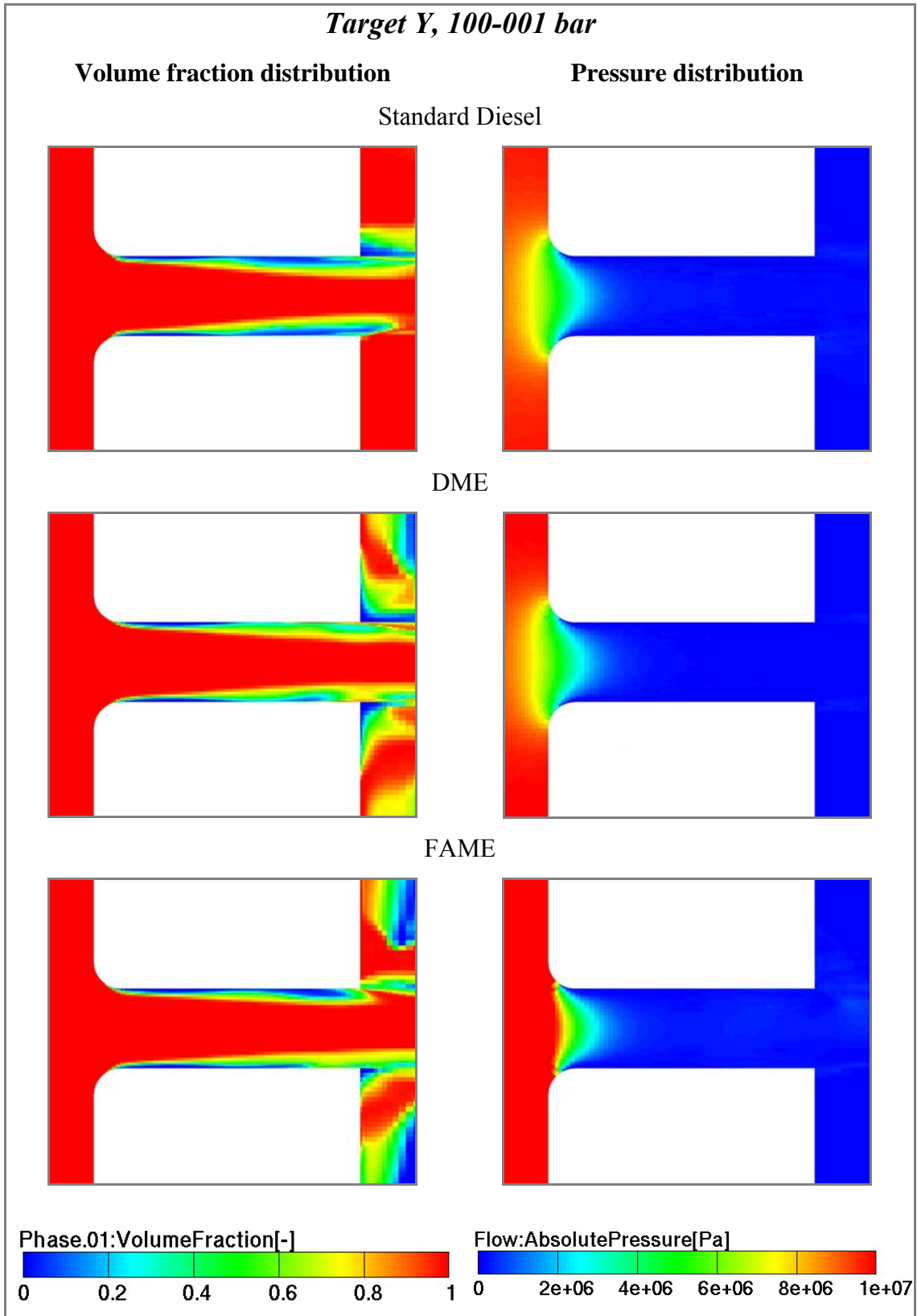


Figure 6.40 Target Y, 100-001bar comparison: volume fraction and absolute pressure distribution

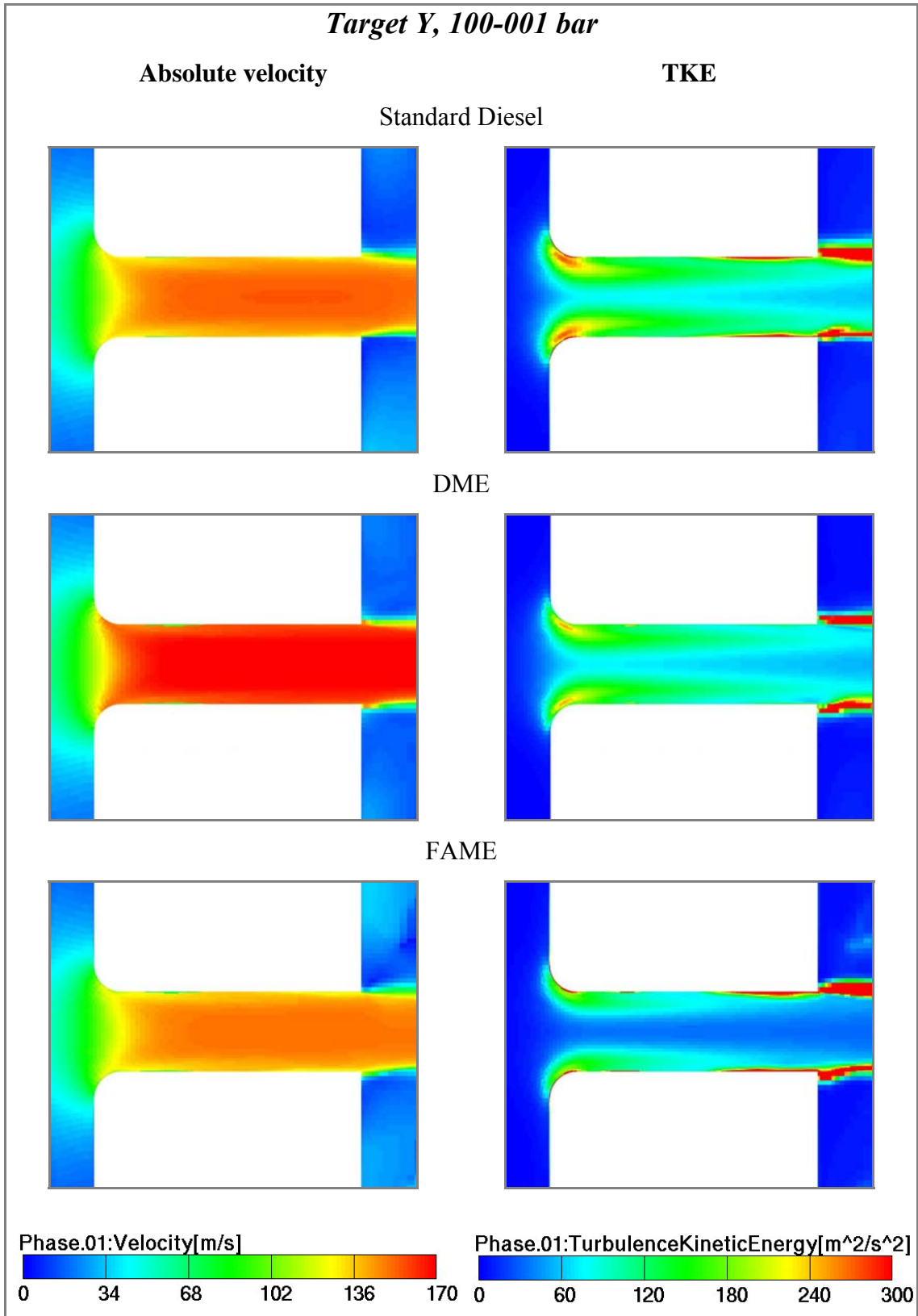


Figure 6.41 Target Y, 100-001bar comparison: absolute velocity and TKE distribution

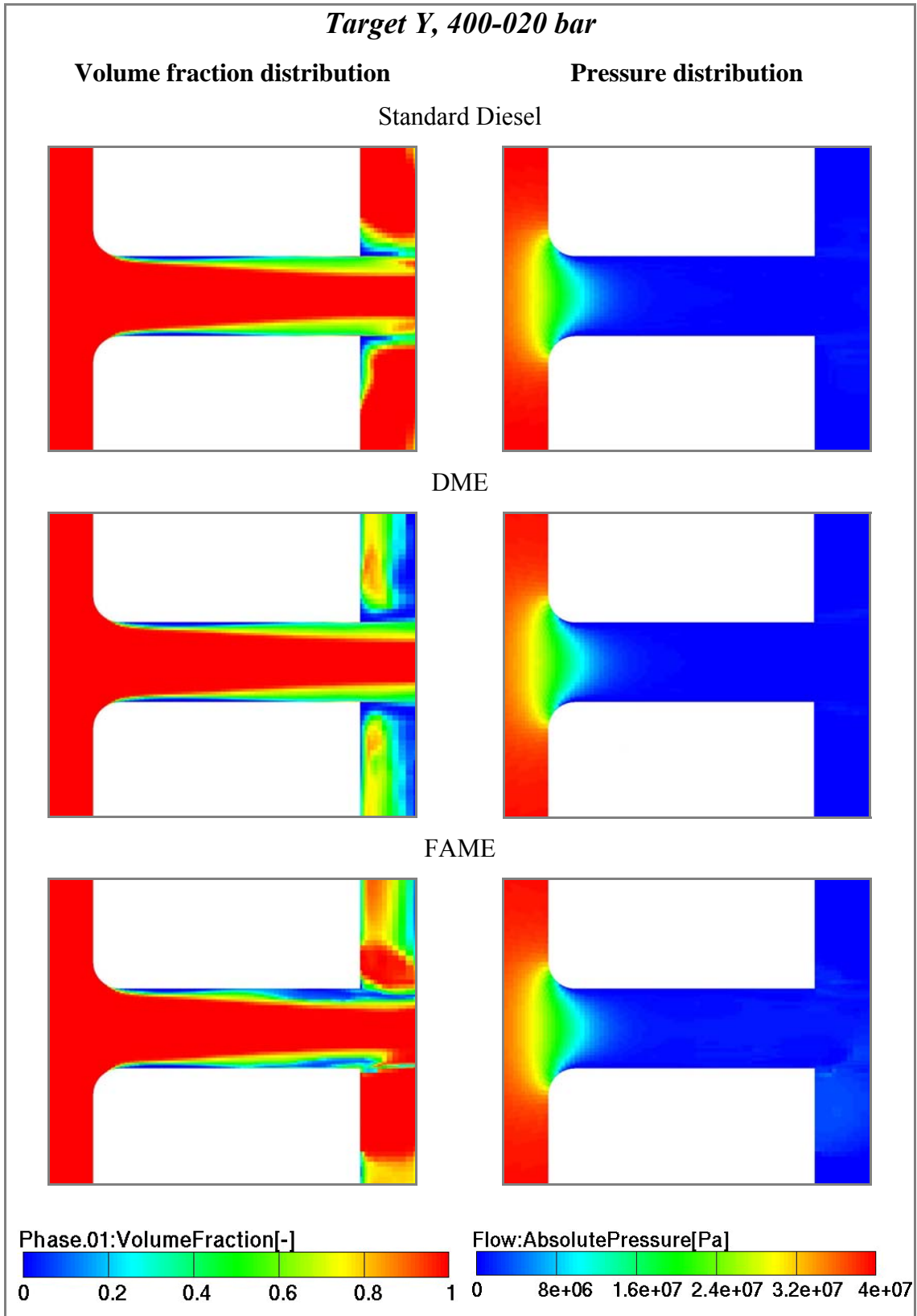


Figure 6.42 Target Y, 400-020bar comparison: volume fraction and absolute pressure distribution

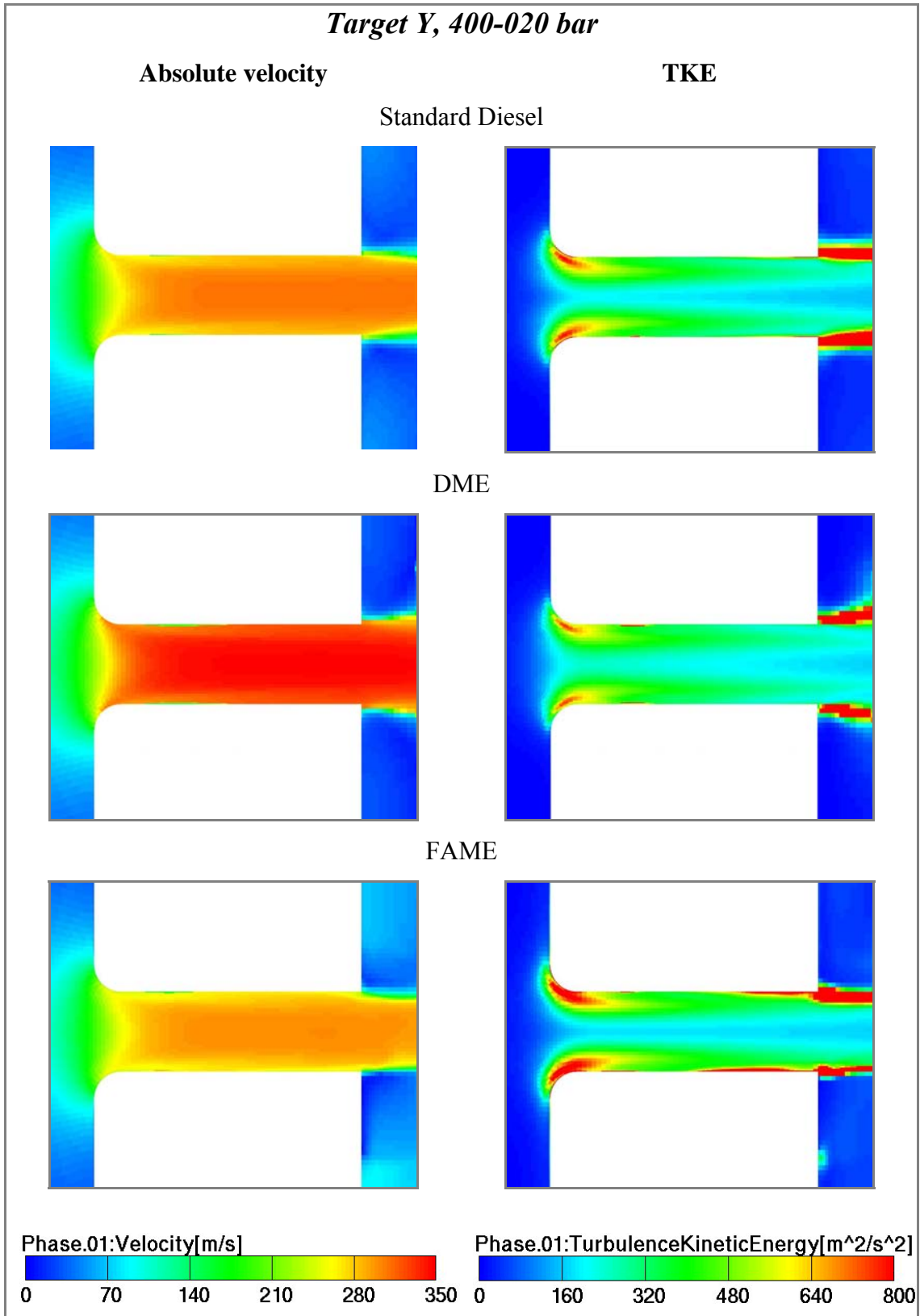


Figure 6.43 Target Y, 100-001bar comparison: absolute velocity and TKE distribution

6.3.3. Mass flow rate

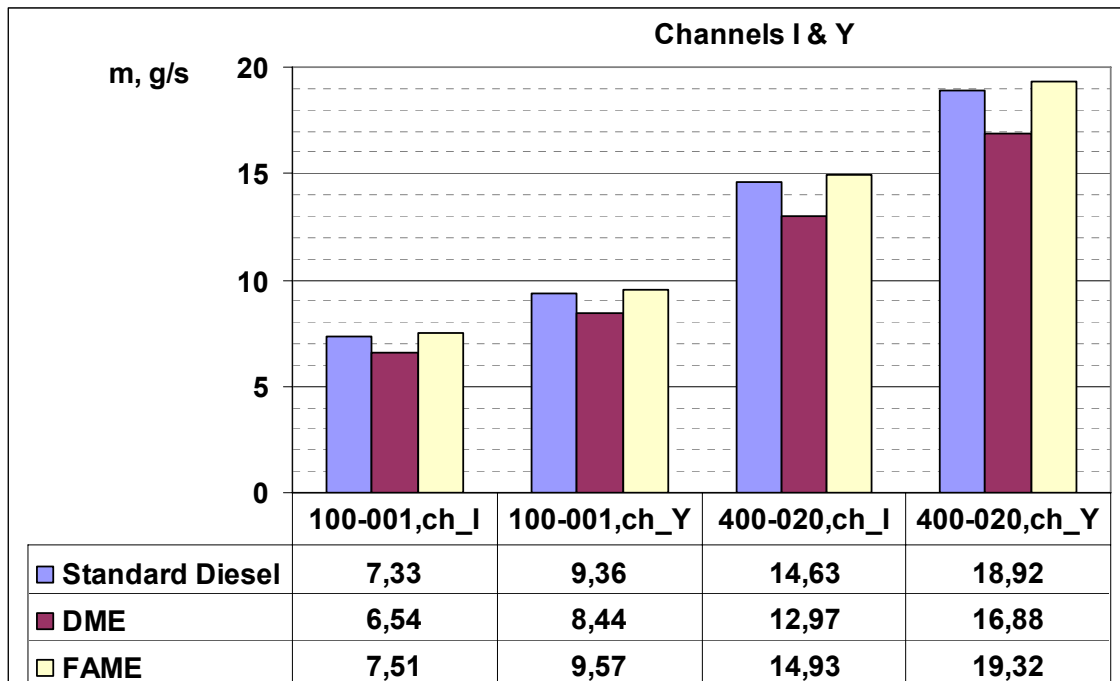


Figure 6.44 Target I&Y comparison: mass flow rate

6.3.4. Erosion incubation time and M DPR

Erosion selection for simulations on Target domains were on target itself, not along narrow channel wall.

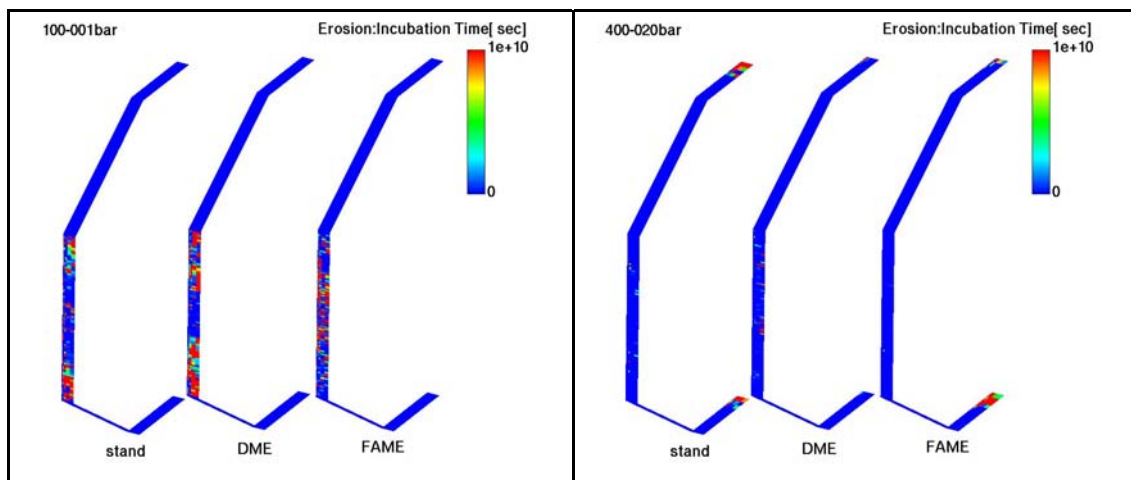


Figure 6.45 Target I comparison: erosion incubation time on target

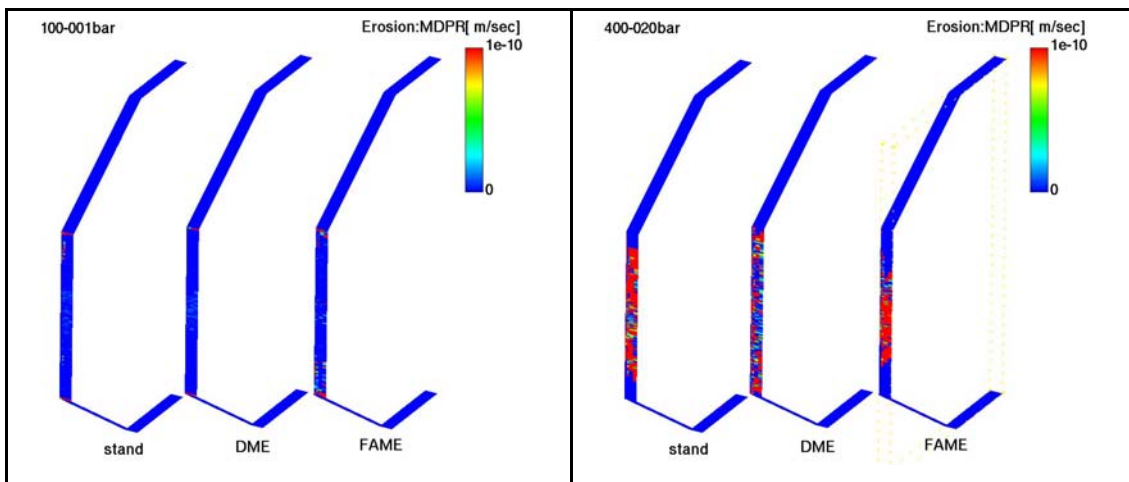


Figure 6.46 Target I comparison: MDPR on target

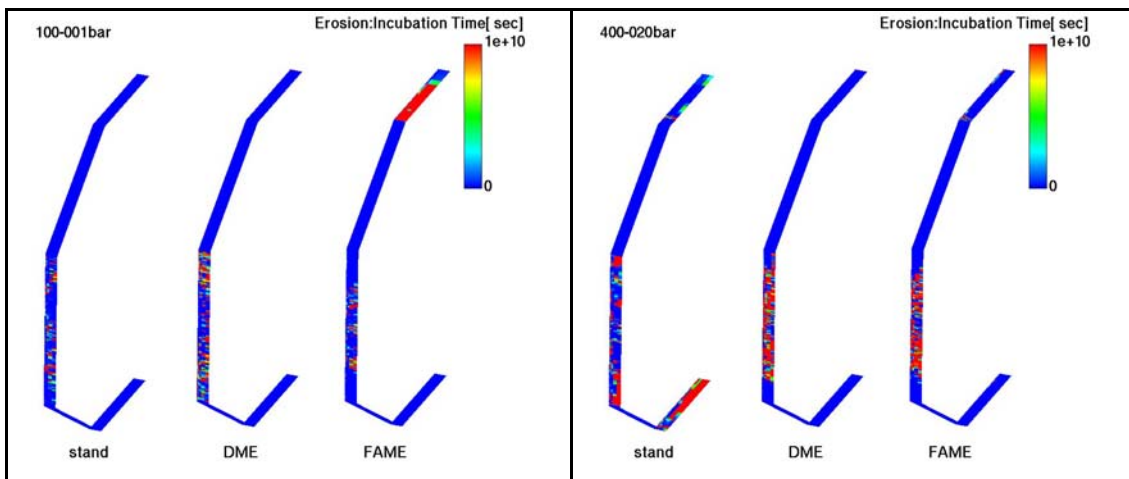


Figure 6.47 Target Y comparison: erosion incubation time on target

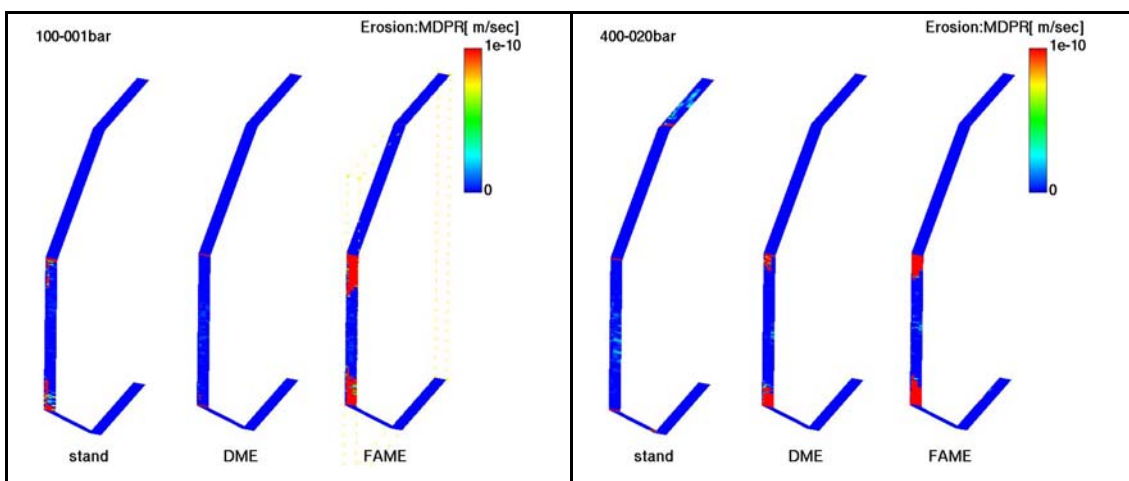


Figure 6.48 Target Y comparison: MDPR on target

6.3.5. Velocity profiles vs. narrow channel height

Velocity profiles were taken along polyline near narrow channel exit, as presented in following figure. Polyline is placed on symmetry plane.

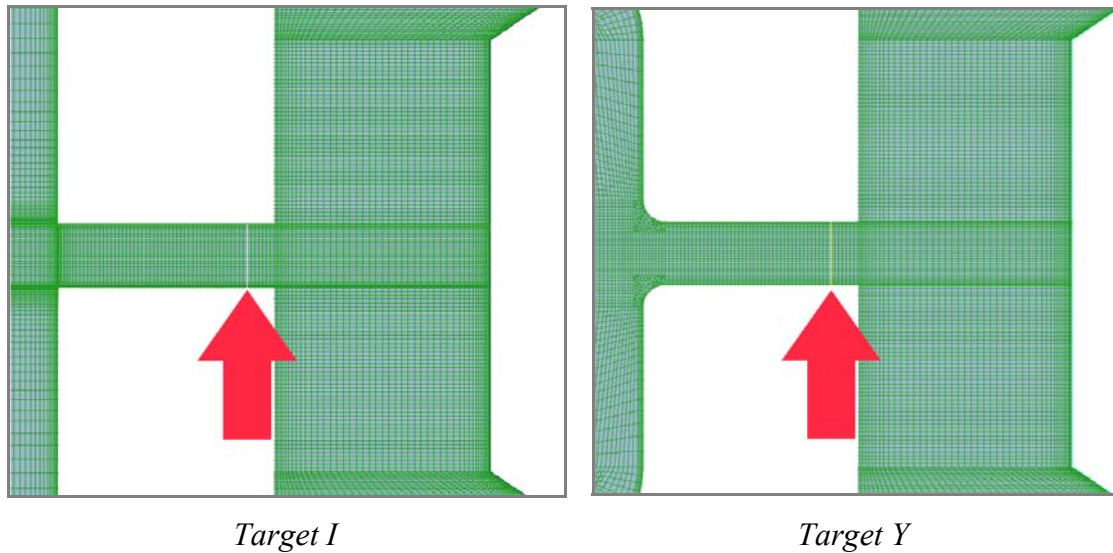


Figure 6.49 Target flow: location of polyline on which velocity profiles were taken

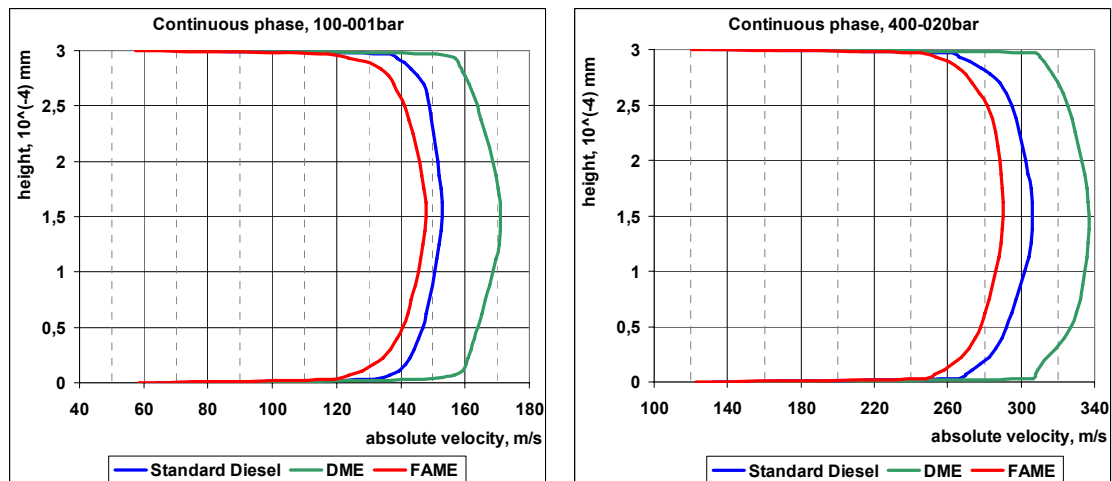


Figure 6.50 Target I comparison: velocity profiles vs. narrow channel height

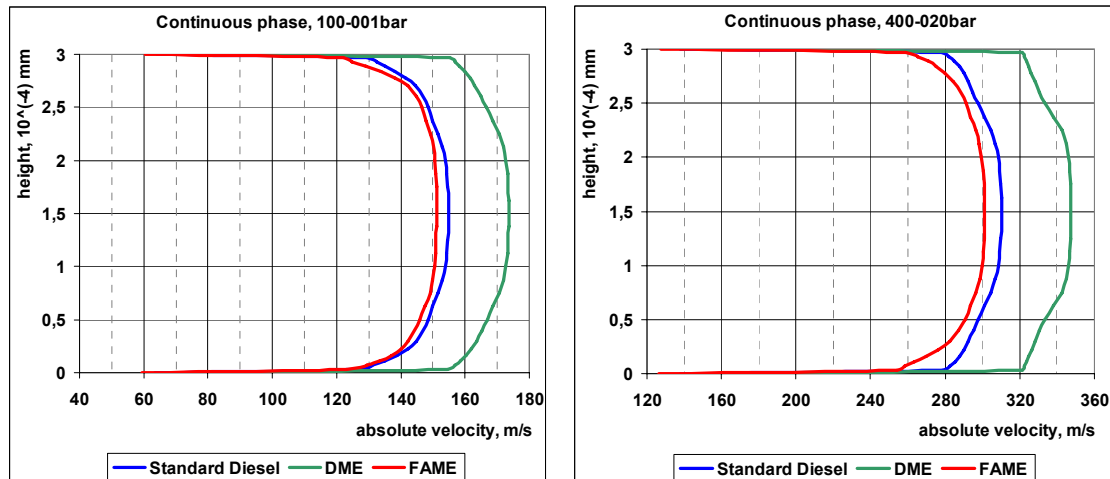


Figure 6.51 Target Y comparison: velocity profiles vs. narrow channel height

6.3.6. Target I results analysis

Cavitation is present in all cases and it is bigger in 400-020 cases for all fuels. It is distributed along whole narrow channel length. Increasing cavitation thickness causes “collision” of upper and lower cavitation trails near narrow channel exit. Pressure distribution indicates intense pressure drop near narrow channel inlet, which is observed earlier in Channel I cases. Absolute velocity and TKE distribution is very similar with Channel I cases, of course with different scale.

Mass flow rate, *Figure 6.44*, shows that FAME fuel has highest, and DME fuel has lowest value. Values for standard fuel are slightly lower than the ones for FAME. This is also mentioned in Channel I cases.

Erosion incubation time distribution, *Figure 6.45*, is smaller in 400-020 case, which is consequence of lower cavitation. MDP, *Figure 6.47*, shows that biggest values are around regions where cavitation vanishes.

Velocity profiles near narrow channel exit, *Figure 6.50*, indicate that flow is developed (despite sharp inlet). DME fuel has highest velocity profile.

6.3.7. Target Y results analysis

Cavitation is present in all cases. It is also distributed along whole narrow channel zone but thickness is significantly lower, and there is no collision of upper and lower cavitation trail on narrow channel exit. Pressure distribution indicates less intense pressure drop near narrow channel inlet. Absolute velocity and TKE distribution is very similar with Channel Y cases, of course with different scale.

Mass flow rate, *Figure 6.44*, shows that FAME fuel has highest, and DME fuel has lowest value. Values for standard fuel are slightly lower than the ones for FAME.

Erosion incubation time distribution, *Figure 6.46*, is bigger in 400-020 case (unlike Target I cases). MDPR, *Figure 6.48*, shows that biggest values are around regions where cavitation vanishes, which is observed earlier. Standard fuel has lowest MDPR.

Velocity profiles near narrow channel exit, *Figure 6.51*, indicate that flow is developed and DME fuel has highest velocity profile.

7. CONCLUSION

CFDWM/FIRE application can give us valuable data regarding multiphase cavitating flow inside nozzles. In *Chapter 6.1* it is shown that mathematical model is valid for its purpose and that nozzle flow for different fuels can be done.

When comparing different fuels simulation results, some obvious differences can be observed.

Most significant conclusion regarding to comparison between fuels is that in mass flow rate equation, fluid density is more significant term than molecular viscosity. This is concluded based on fact that in almost all cases DME fuel had highest velocity but lowest mass flow rate. If we combine that with fluid properties, *Table 5.1*, above conclusion can be derived.

Based on simulation results, when designing fuel nozzles, cavitation should always be considered, as well as resulting cavitation erosion. Nozzles in which less cavitation occurs will achieve larger mass flow rates for same boundary conditions. This conclusion is derived from differences between Channel/Target I and Channel/Target Y cases.

8. REFERENCES

- [1] Hammond G.P., Kallu S., McManus M.C., *Development of biofuels for the UK automotive market*, Applied Energy, 2006.
- [2] Mulqueen S., *The European Alternative Fuel Market And The Role Of Fuel Additives*, Biofuels Conference, Greece 2007
- [3] Diesel Fuel Injection Equipment Manufacturers Common Position Statement, *Fatty Acid Methyl Ester Fuels As a Replacement or Extender for Diesel Fuels*, 2004, published on:
http://www.ufop.de/downloads/FAME_Statement_June_2004.pdf
- [4] AVL FIRE v.8, *Multiphase Flow*, AVL, Graz, 2004
- [5] AVL FIRE, *New Cavitation Model: a parametric variation of coefficients*, AVL, Graz, 2006
- [6] Greif D., Wang D.M., *Aspects Of Modelling Cavitation Effects Within Injecton Equipment Using Advanced Two-Fluid Techniques*, Turbulence, Heat and mass transfer 5
- [7] Hanjalić K., *Dinamika stišljivog fluida*, 1970
- [8] Franjić, K., *Hidraulički strojevi i postrojenja*, FSB scrypt
- [9] Asi O., *Failure of a Diesel Engine Injector Nozzle by cavitation damage*, Engineering Failure Analysis, 2006.
- [10] ASM handbook, vol. 13, Corrosion. Metals Park (OH): American Society for Metals; 1987.
- [11] ASM handbook, vol. 18, Friction, lubrication, and wear technology. Metals Park (OH): American Society for Metals; 1992.
- [12] ASM handbook vol.11., Failure Analysisi and prevention, 1986
- [13] Dular M., Bachert B., Stoffel B., Sirok B.. *Relationship between cavitation structures and cavitation damage*, Wear, 2004
- [14] Szkodo M., *Mathematical description and evaluation of cavitation erosion*

- resistance of materials*, Journal of Materials Processing Technology, 2005.
- [15] Berchiche N., Franc J.P., Michel J.M., *A Cavitation Erosion Model for Ductile Materials*, Journal of Fluids Engineering, 2002
- [16] Franc J.P., Riondet M., *Incubation Time and Cavitation Erosion Rate of Work-Hardening Materials*, CAV2006 simposium, 2006
- [17] Greif D., Morozov A., Winklhofer E., Tatschl R., *Experimental and Numerical Investigation of Erosive Effects Due to Cavitation Within Injection Equipment*, ICCHMT, 2005
- [18] Payri F., Bermudez V., Payri R., Salvador F.J., *The influence of cavitation on the internal flow and the spray characteristics in diesel injection nozzles*, Fuel, 2004
- [19] Chaves H., Knapp M., Kubitzek A., *Experimental study of cavitation in the nozzle hole of diesel injectors using transparent nozzles*, SAE Paper, 1995
- [20] ASM handbook vol.11., Failure Analysis and prevention, 1986
- [21] Semelsberger, T.A, Borup R.L. Greene, H.L., *Dimethyl Ether (DME) as an Alternative Fuel*, Journal of Power Sources, 2005.
- [22] Hansen J.B., Mikkelsen S., *DME as a Transportation Fuel*, 2001.
- [23] Badock C., Wirth R., Fath A., Leipertz A., *Investigation of cavitation in real size diesel injection nozzles*, International Journal of Heat and Fluid Flow, 1999
- [24] Takenakaa N., Kadowakia T., Kawabatab Y., Limc I.C., Simc C.M., *Visualization of cavitation phenomena in a Diesel engine fuel injection nozzle by neutron radiography*, Nuclear Instruments and Methods in Physics Research, 2005.
- [25] AVL FIRE v.8, *CFD Solver v.8.3*, AVL, Graz, 2004

APPENDIX: FORTRAN CODE OF USER FUNCTIONS

```
-----
module allocating
DOUBLE PRECISION, ALLOCATABLE, DIMENSION(:) :: vfmax_cell
INTEGER, ALLOCATABLE, DIMENSION(:) :: vfmax_bnd
INTEGER, ALLOCATABLE, DIMENSION (:,:) :: cell_id

end module allocating

-----
SUBROUTINE useini(mat,mph)

c *****
c 1. dynamic allocation of vfmax_cell i vfmax_bnd- 1D allocation
c 2. dynamic allocation of cell_id - 2D allocation
c 3. creation of cell_id matrix
c
c INPUT VARIABLES:
c ip3          number of mesh cells in z direction, unit (-)
c z_value      cell centre z coordinate on highest z value, unit m
c
c *****

USE comm1
USE allocating
INCLUDE 'com0.inc'

print*,'Number of cells is ',ncell
if(.not.ALLOCATED(vfmax_cell)) ALLOCATE(vfmax_cell(ncell))
vfmax_cell(:)=0.

if(.not.ALLOCATED(vfmax_bnd)) ALLOCATE(vfmax_bnd(nbfac))
vfmax_bnd(:)=0.

ip3=5
z_value=(-0.00003)
ncell_2=ncell/ip3

if(.not.ALLOCATED(cell_id)) ALLOCATE(cell_id(ncell_2,ip3))
cell_id(:,:)=0

print*,''
print*,'cell_id matrix'
print*,''
ixx=0
do ip=nsp(mat),nep(mat)
  if (xp(3,ip).gt.(z_value))then
    ixx=ixx+1
    iyy=2
    cell_id(ixx,1)=ip
    do ip2=nsp(mat),nep(mat)
      if (abs(xp(2,ip2)-xp(2,ip)).lt.(0.0000001).and.
x  abs(xp(1,ip2)-xp(1,ip)).lt.(0.0000001).and.ip2.ne.ip) then
        cell_id(ixx,iyy)=ip2
        iyy=iiy+1
      end if
    end do
  end do
end do
```

```
print*,    ix,    cell_id(ix,:)
    end if
end do

c    print*,    cell_id(1,:)

print*, 'Initialization finished!'
print*, ''
print*, ''
RETURN
END

-----
SUBROUTINE useout(mat,mph,ifile)

USE comm1
USE allocating
INCLUDE 'com0.inc'

c    *****
c    1. Comparison of volume fraction in z direction, where max value
of
c    volume fraction is placed in cell with highest z value.
c    This is used when simulating transparent optical measurement, in
c    this case volume fraction.
c
c    2. Limitation ok TKE (listing or listing+limitation)
c
c    INPUT VARIABLES:
c    ip3          number of mesh cells in z direction, unit (-)
c    limit_TKE    TKE value limitation, unit (m/s)2
c    *****

print*, 'Useout routine started!'
c    ip4=0
ip3=5
ncell_2=ncell/ip3

do ip=1,ncell_2
    vfm=vf(cell_id(ip,1))
    ip4=ip4+1
c    print*,    ip4,    vfm
    do ip2=2,ip3
        if (vf(cell_id(ip,ip2)).gt.vfm) then
            vfm=vf(cell_id(ip,ip2))
        end if
c    print*,    ip4,    vfm
    end do
    vfm_max_cell(cell_id(ip,1))=vfm
end do

c    *****

c    limit_TKE=100
c    print *, limit_TKE, '00000000000000000000'
c    icount_1=0
c    icount_2=0

c    do ip6=nsp(mat),nep(mat)
```

```
c      if (te(ip6).ge.limit_TKE) then
c      icount_2=icount_2+1
c      te(ip6)=limit_TKE
c      print*,  te(ip6),  'in cell no.',  ip6
c      end if
c      end do
c      print*,''
c      print*,  'There was', icount_2,'cells with TKE over',
ilimit_TKE
c      print*,  'There was', icount_2,'cells with TKE limited to',
limit_TKE
c      print*,''

      print*,'Useout routine finished!'

      RETURN
      END
```

```
-----
      SUBROUTINE useplo(mat,mph,ifile)

      USE comm1
      USE allocating
      INCLUDE 'com0.inc'

      call Write_User_Fl3(mat,mph,ifile,'max_VF','- ',
x          ncell,nbfac,vfmax_cell,vfmax_bnd)

      print*, 'Successfully written to *.Fl3 file.'

      RETURN
      END
```